



저작자표시-비영리-변경금지 2.0 대한민국

이용자는 아래의 조건을 따르는 경우에 한하여 자유롭게

- 이 저작물을 복제, 배포, 전송, 전시, 공연 및 방송할 수 있습니다.

다음과 같은 조건을 따라야 합니다:



저작자표시. 귀하는 원저작자를 표시하여야 합니다.



비영리. 귀하는 이 저작물을 영리 목적으로 이용할 수 없습니다.



변경금지. 귀하는 이 저작물을 개작, 변형 또는 가공할 수 없습니다.

- 귀하는, 이 저작물의 재이용이나 배포의 경우, 이 저작물에 적용된 이용허락조건을 명확하게 나타내어야 합니다.
- 저작권자로부터 별도의 허가를 받으면 이러한 조건들은 적용되지 않습니다.

저작권법에 따른 이용자의 권리는 위의 내용에 의하여 영향을 받지 않습니다.

이것은 [이용허락규약\(Legal Code\)](#)을 이해하기 쉽게 요약한 것입니다.

[Disclaimer](#)

공학박사 학위논문

**Complex amplitude
imaging and display systems
for high space-bandwidth product**

높은 공간 대역폭을 위한
복소 진폭 이미징 및 디스플레이 시스템

2021년 2월

서울대학교 대학원

전기·정보공학부

이 병 효

공학박사 학위논문

**Complex amplitude
imaging and display systems
for high space-bandwidth product**

높은 공간 대역폭을 위한
복소 진폭 이미징 및 디스플레이 시스템

2021년 2월

서울대학교 대학원

전기·정보공학부

이 병 효

Complex amplitude imaging and display systems for high space-bandwidth product

지도 교수 이병호

이 논문을 공학박사 학위논문으로 제출함

2021년 2월

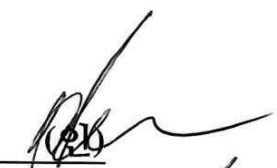
서울대학교 대학원


전기·정보공학부

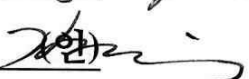
이 병 호


이병호의 공학박사 학위 논문을 인준함

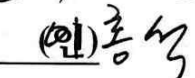
2021년 2월

위 원 장: 鄭潤燾 

부위원장: 李竝浩 

위 원: 姜勳宗 

위 원: 이재상 

위 원: 이홍석 

Abstract

**Complex amplitude
imaging and display systems
for high space-bandwidth product**

Byounghyo Lee
Department of Electrical and Computer Engineering
College of Engineering
Seoul National University

Understanding light as a wave makes it possible to interpret a variety of phenomena, including interference and diffraction. By modulating the complex amplitude of the wave, hologram, three-dimensional imaging, and three-dimensional display system, called future technologies, can be implemented that surpass the currently commercialized optical engineering devices. Although a lot of research has been conducted to develop and commercialize the wave optical system, state-of-the-art devices are still far from the performance expected by the public due to the limited space-bandwidth product (SBP).

This dissertation presents the studies on high SBP for complex amplitude imaging and display systems. The performance of a complex amplitude modulating system is limited by the SBP, which represents the amount of information in the optical system. To improve the SBP of the complex amplitude in a limited amount of information, the author applies various multiplexing techniques suitable for the implemented system. In practice, the spatial frequency multiplexed digital holography is devised by efficiently allocating frequency bandwidth with dual-wavelength light sources. The author also applies illumination

multiplexing to the single-shot Fourier ptychography to expand the amount of information recorded in the image sensor. Computational reconstruction algorithm combined with novel optical design allows the acquired multiplexed information to be decomposed in the imaging system, leading to improvement of size of the image or resolution. Furthermore, the author applied illumination multiplexing and temporal multiplexing techniques to holographic displays. The multiplexed information is decomposed by a combination of human perceptual temporal bandwidth and spatial filtering. The SBP enhanced holographic display is implemented, providing a more wide viewing angle.

It is expected that this thesis will contribute to the development of the imaging and display fields, which share a common problem of small SBP. The author hopes that the proposed methods will inspire various researchers to approach the implementation of complex amplitude modulating systems, and various future industries, including 3-D inspection, holography, virtual reality, and augmented reality will be realized with high-performance.

keywords: Space-bandwidth product, complex amplitude, digital holography, Fourier ptychography, holographic displays

student number: 2015-22798

Contents

Abstract	i
Contents	iii
List of Tables	vi
List of Figures	vii
1 Introduction	1
1.1 Complex Amplitude of Wave	1
1.2 Complex Amplitude Optical System	3
1.3 Motivation and Purpose of the Dissertation	5
1.4 Scope and Organization	8
2 Space-Bandwidth Product	10
2.1 Overview of Space-Bandwidth Product	10
2.2 Space-Bandwidth Product of Complex Amplitude Imaging Sys- tems	11
2.3 Space-Bandwidth Product of Complex Amplitude Display Sys- tems	13
3 Double Size Complex Amplitude Imaging via Digital Holography	15
3.1 Introduction	15
3.1.1 Digital Holography	16
3.1.2 Frequency Multiplexed Digital Holography	22

3.1.3	Adaptation of Diffractive Grating for Simple Interferometer	24
3.2	Principle	26
3.2.1	Single Diffraction Grating Off-Axis Digital Holography	26
3.2.2	Double Size Implementation with Multiplexed Illumination	29
3.3	Implementation	32
3.4	Experimental Results	34
3.4.1	Resolution Assessment	34
3.4.2	Imaging Result	36
3.4.3	Quantitative 3-D Measurement	38
3.5	Conclusion	42
4	High-Resolution Complex Amplitude Imaging via Fourier Ptychographic Microscopy	43
4.1	Introduction	43
4.1.1	Phase Retrieval	45
4.1.2	Fourier Ptychographic Microscopy	47
4.2	Principle	52
4.2.1	Imaging System for Single-Shot Fourier Ptychographic Microscopy	52
4.2.2	Multiplexed Illumination	55
4.2.3	Reconstruction Algorithm	58
4.3	Implementation	60
4.3.1	Numerical Simulation	60
4.3.2	System Design	64
4.4	Results and Assessment	65

4.4.1	Resolution	65
4.4.2	Phase Retrieval of Biological Specimen	68
4.5	Discussion	71
4.6	Conclusion	73
5	Viewing Angle Enhancement for Holographic Display	74
5.1	Introduction	74
5.1.1	Complex Amplitude Representation	76
5.1.2	DMD Holographic Displays	79
5.2	Principle	81
5.2.1	Structured Illumination	81
5.2.2	TM with Array System	83
5.2.3	Time Domain Design	84
5.3	Implementation	85
5.3.1	Hardware Design	85
5.3.2	Frequency Domain Design	85
5.3.3	Aberration Correction	87
5.4	Results	88
5.5	Discussion	92
5.5.1	Speckle	92
5.5.2	Applications for Near-eye Displays	94
5.6	Conclusion	99
6	Conclusion	100
	Appendix	116
	Abstract (In Korean)	117

List of Tables

3.1	Summary of utilized characteristics of diffractive grating.	25
-----	---	----

List of Figures

1.1	3-D wave representation by 2-D complex amplitude with wave-length.	2
1.2	Complex amplitude optical system.	3
1.3	Block diagram for illustration of dissertation organization.	8
2.1	Illustration of SBP for the optical imaging systems.	11
2.2	Illustration of SBP for the complex amplitude display systems.	13
3.1	Illustration of the conventional DH system.	16
3.2	(a) On-axis and (b) off-axis configurations of the conventional DH systems.	18
3.3	Fourier spectrum of the off-axis DH where object bandwidth is in (a) general case or (b) maximum case.	20
3.4	(a) Frequency domain and (b) optical system of dual-wavelength off-axis DH system.	23
3.5	Single grating off-axis reflective DH system. (a) After collimated by a lens, normally incident beam is diffracted by the diffraction grating and split into reference and signal beams. (b) The -1st order of beam is reflected on the specimen and interferes with the reference beam on the image sensor.	26
3.6	SGDH with multiplexed illumination system. (a) Two wavelengths of beams are diffracted in different directions. (b) The two signal beams of adjacent regions of 1 and 2 are reflected on the diffraction grating.	29

3.7	Experimental setup of proposed method with multiplexed illumination. The size of the system is measured in the area indicated by the yellow dashed line. The mobile phone is placed next to the system for size comparison.	32
3.8	Experimental results of 1951 USAF resolution target imaging. (a) The captured hologram and (b) its Fourier spectrum. (c, d) The intensity images of the filtered regions in the spatial domain (e) The stitched double size of the image of the hologram. The size of image sensor is presented using the red arrows. (f) Zoom-in image that presents high-resolution part. (g) The cross-section of the intensity through the vertical line of group 5. . . .	35
3.9	Holographic imaging experimental results using the latent fingerprint. (a) Synthesized focus image. (b1, c1) The zoom-in intensity images corresponding to the noted boxes in part (a) before the numerical propagation. Focused zoom-in (b2, c2) amplitude and (b3, c3) phase images reconstructed by numerical propagation.	36
3.10	Quantitative phase imaging using a concave mirror. (a) The stitched wrapped phase image. (b) Unwrapped phase profile. (c) The cross-section of the wrapped phase along x -axis, which corresponds to the black dash line of (a). (d) Unwrapped phase profile of (c) with theoretical value. (e) Three-dimensional distribution of the reconstructed result.	39
3.11	Zernike polynomials coefficients of the experimental result and theoretical model.	41
3.12	Two-dimensional phase error between the reconstructed result and the theoretical value.	41

4.1	Schematic diagram of the phase lost by measuring intensity image.	45
4.2	Optical acquisitions and computational reconstruction of FPM. High-resolution complex amplitude is reconstructed by multiple low-resolution intensities.	47
4.3	Iterative projections on the constraints to find solution.	49
4.4	SSFPM set-up. The specimen is illuminated by multiple LEDs. (a) Three dimensional schematic diagram of SSFPM. (b) Its cor- responding two dimensional diagram.	52
4.5	The schematic diagram of (a1) single illumination and (b1) mul- tiplexed illumination. (a2, b2) The Fourier spectrum of speci- men. Measured intensity pattern in CCD with (a3) single illu- mination and (b3) multiplexed illumination. (b2) The Fourier spectrum with LED multiplexing. (b4) Fourier spectrum recon- structed by SSFPM.	57
4.6	Numerical simulation results of SSFPM. The input (a) intensity and (b) phase of complex specimen. (c) A measured intensity pattern. (d) A magnified central sub-image which has low reso- lution. Applying the measured pattern to the SSFPM, (e) inten- sity and (f) phase profiles are reconstructed.	61
4.7	Numerical simulation results to select Δk_i . (a) Plot of the phase error while changing $\Delta k_i/\Delta k_m$ from 1 to 2. Several recon- structed results are displayed in (b).	63

4.8	(a) The original experimental data from 7 x 7 lens array with turning 3 x 3 LEDs simultaneously on. (b) The image from conventional x10 microscope with coherent illumination. (c, d) The high resolution of reconstruction intensity and phase profiles, respectively. (e-g) The zoom in images of raw data, reconstruction image, and conventional microscope image.	67
4.9	Biological specimen imaging using SSFPM. High resolution (a) intensity and (b) phase results. The magnified (c1-e1) intensity images and (c2-e2) phase images corresponding to the regions of red, green, and blue boxes in (a) and (b). (c3-e3) The coherent microscopic images, for comparison. (c4-e4) The raw-data images taken by proposed SSFPM extracted from central bright sub-image.	69
4.10	3-D Phase distribution recovered by SSFPM, phase-shifting DH, and TIE	70
5.1	Simulations of complex amplitude representations by amplitude discard, double-phase, and single-sideband amplitude encoding methods.	78
5.2	Schematic diagram of (a) the conventional and (b) the proposed TM DMD holographic display.	81
5.3	Frequency domain design to utilize the filter array. The sideband encoding and the anamorphic transformation are implemented to match the structure of the filter array. The DC components are blocked using the bezel of the array.	86

5.4	(a) An example of captured image from raw binary hologram. (b) The aberration corrected result using a correction map. (c) The pre-measured global correction maps.	88
5.5	Temporal multiplexing to reduce speckle noise.	89
5.6	Captured results in changing the image sensor's observation an- gles. Each viewing zone covers $\pm 3.2^\circ \times \pm 3.2^\circ$ from the center axis, indicated by the inset in the right bottom.	90
5.7	Experimental result when the 2-D (1st) and 3-D hologram (2nd - 4th) are displayed.	91
5.8	Four sample frames of the holographic video as focusing on the middle depth. Top columns are experimental photographs and bottoms are input images.	91
5.9	(a) The speckle contrast ratio versus the number of TM. (b),(c) Experimental results of the 2-D uniform hologram without TM and with TM of 30 frames, respectively. (d),(e) Enlarged distri- butions of the b and c	92
5.10	Applications of SBP expanding in four types of holographic dis- plays.	94
5.11	Eye-box expanded system of AR near-eye holographic display. .	95
5.12	Full-color binary holographic near-eye display.	97
5.13	Experimental results of full-color binary near-eye holographic display.	98

Chapter 1. Introduction

1.1 Complex Amplitude of Wave

Light can be described by diverse theories such as ray, wave, electromagnetic, and quantum optics. Although the quantum or electromagnetic optics provides the most complete interpretation of the light, many optical phenomenon including diffraction and interference can be described by the wave optics. In this dissertation, the wave optics is adopted and the light is interpreted as the scalar wavefunction.

Mathematically, real wavefunction $u(r, t)$ is described by the position of r and time of t , and it can be represented by complex wavefunction of $U(r, t)$ where $u(r, t) = \text{Re}(U(r, t))$. The complex wavefunction is written in the form of $U(r, t) = U(r) \exp(j2\pi\nu t)$, where ν is temporal frequency. The time-independent term $U(r) = a(r) \exp(j\phi(r))$ is called complex amplitude, where a is the amplitude and ϕ is the phase. Since ν is extremely high-value of 10^{13} in visible light, the natural observed light is time-averaged wavefunction, and it depends on only the complex amplitude rather than wavefunction. Therefore, it is sufficient to interpret the wave by complex amplitude in display and imaging systems, where the detecting frequency is low compared with the ν .

Since complex amplitude expresses waves, in order to understand all waves in three-dimensional (3-D) space, it is necessary to know all of the complex amplitudes in 3-D space. Fortunately, if the wavelength of the wave is known, the complex amplitudes of 3-D space can be acquired with only the complex amplitude of one specific plane. More specifically, when complex amplitude at z_0 plane is $f(x, y) = U(x, y, z_0)$, any arbitrary complex amplitude is calculated

by

$$U(x, y, z) = \iint_{-\infty}^{\infty} F(\nu_x, \nu_y) \cdot \exp(jk_z(z - z_0)) \cdot \exp[j(\nu_x x + \nu_y y)] d\nu_x d\nu_y, \quad (1.1)$$

where $F(\nu_x, \nu_y)$ is Fourier transform of $f(x, y)$, and ν_x, ν_y are spatial frequencies at z_0 plane. Note that $k_z = 2\pi\sqrt{\lambda^{-2} - \nu_x^2 - \nu_y^2}$. Figure 1.1 shows that complex amplitude on the other z -axis can be calculated and reconstructed from the complex amplitude in one plane. Therefore, this dissertation focuses on acquiring or displaying 2-D complex amplitude in a specific plane.

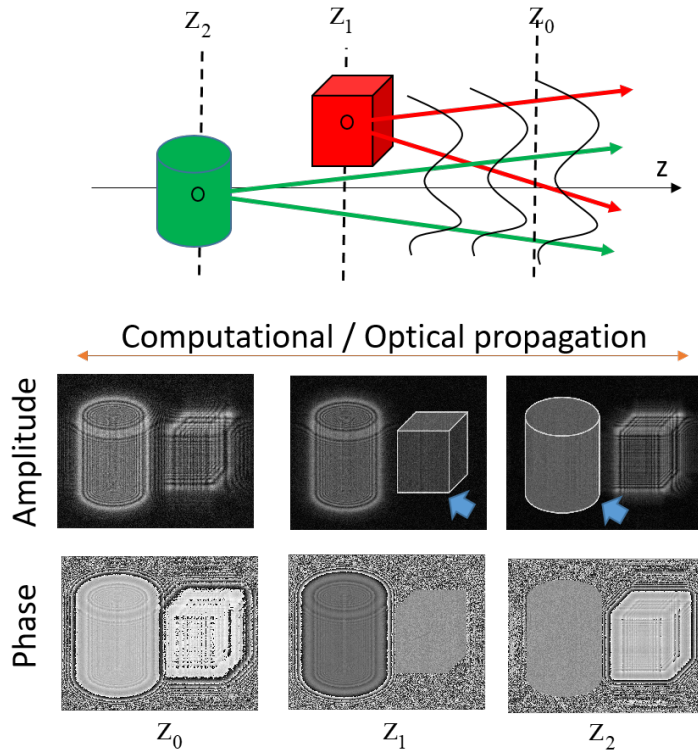


Figure 1.1 3-D wave representation by 2-D complex amplitude with wavelength.

1.2 Complex Amplitude Optical System

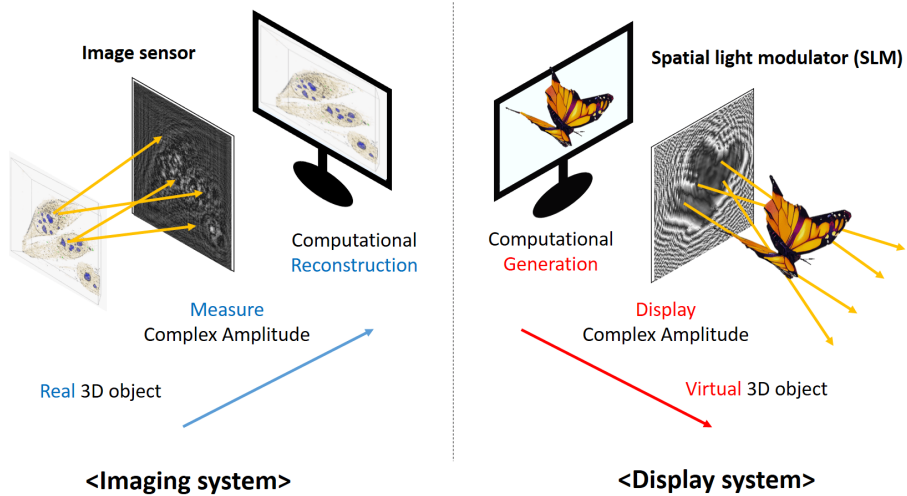


Figure 1.2 Complex amplitude optical system.

Since wave is fully described by the complex amplitude, many optical applications can be realized by understanding and controlling it. In this dissertation, the author focuses on two optical systems: imaging system and display system. Figure 1.2 shows the schematic diagrams of the complex amplitude optical systems. As described in the Section 1.1, the wave can be represented as the complex amplitude of the specific 2-D plane with knowledge of the wavelength. In the imaging system, the wave from a real 3-D object is obtained by measuring the complex amplitude with an image sensor. Then the wave from the real object is computationally reconstructed with many useful applications beyond the conventional 2-D imaging system. Similarly, in the display system, a spatial light modulator (SLM) is used to display a computationally formed complex amplitude, thereby implementing a 3-D display that goes beyond the conventional two-dimensional display.

Most commercialized optical imaging and display devices interpret light as rays and deal with only light intensity information. For example, optical microscopes and cameras can only obtain images on a focused 2-D plane, and TVs and monitors can display only two-dimensional (2-D) images on a panel. On the other hand, the complex-amplitude optical system handles the amplitude and phase of light together, enabling more diverse optical engineering applications. For instance, in the field of imaging systems, the phase provides 3-D (three dimensional) depth information because optical path length difference through thickness of the object leads to the phase delay. Moreover, the phase makes it possible to observe high-transmittance cells or high-reflectance objects which have little change in intensity. Also computational post-processing is possible which gives changing the focal plane, correcting the optical aberrations, and application of the tomography. It enables measurement and detection of 3-D profiles with sub-wavelength accuracy. Coherent diffraction imaging and computational imaging are other applications with enhancement for resolution, size of the image, and so on. Complex amplitude is also crucial in the field of display systems. Hologram which is familiar word to the public, can be realized by controlling the complex amplitude with the characteristics of the interference and diffraction. The hologram reproduces the identical wave as the light in nature of a 3-D object, and reproduces vivid experience without the need for glasses. Holographic displays are implemented with lots of applications in the fields of augmented reality (AR) and virtual reality (VR) as type of panel or near-eye.

1.3 Motivation and Purpose of the Dissertation

In the previous section, the author mentioned that complex amplitude control has many advantages with lots of applications in the fields of imaging and display. For obtaining (or imaging) the complex amplitude, a charge-coupled device (CCD) or a complementary metal-oxide-semiconductor (CMOS) is used as an image sensor. The image sensor detects the number of photons during the exposure time and converts it into a 2-D image. The number of photons corresponds to the intensity of the wave, so the output 2-D image is $I(r) = |U(r)|^2 = |a(r)|^2$. From the intensity, only the amplitude $a(r)$ is obtainable, and the phase information $\phi(r)$ is lost. Therefore, a specific optical technique is required to obtain both amplitude and phase, such as digital holography using interferometer or phase retrieval by computational imaging. However, since the image sensor has limited number of pixels, the amount of information that can be obtained is limited. Furthermore, the amount of information is further limited in order to obtain complex information rather than amplitude only. The limited information deteriorates the performance of the imaging result, such as resolution and size of the image. In fact, these two parameters undergo a trade-off relationship, and the product of them is defined as space-bandwidth product (SBP) because the resolution corresponds to the bandwidth and the size of the image corresponds to the space. A detailed explanation of SBP will be given in Section 2.2. Therefore, the limited performance of the complex amplitude imaging system corresponds to the low SBP.

Meanwhile, the performance degradation of the complex amplitude system due to the low SBP is similarly applied to the display system. To reconstruct (or display) complex amplitude, a spatial light modulator (SLM) is used. The SLM, which is composed of pixelated structure, can modulate wave amplitude

or phase only. Therefore, a specific technique that encodes the complex amplitude to the amplitude or the phase SLM is adopted. For instance, when the amplitude SLM is adopted, it is possible to encode the complex amplitude with 50% loss of bandwidth through the single-sideband (SSB) method [1]. Another technique to use phase only SLM is to apply the double-phase encoding [2]. However, the double-phase method also sacrifices bandwidth more than 50% to avoid noise. The detailed explanation of encoding the complex amplitude will be covered in Section 5.1.1. Since SBP is an index that is the product of space and bandwidth, complex amplitude display systems have low SBP due to the reduced bandwidth to represent complex values. It degrades the performance of the display such as the viewing angle or the size of display, which will be explained in detail in Section 2.3.

In this dissertation, the author proposes complex amplitude optical systems to achieve high SBP. The authors noted that imaging and display optical systems have a common limitation of low SBP in order to control complex amplitudes using an amplitude or phase only expression device. Therefore, the author tries to solve the common problem in both complex amplitude systems by proposing novel optical systems providing high SBP. Specifically, in the imaging system, size of the image and resolution of the complex amplitude are increased while keeping the single-shot acquisition. To implement high SBP optical imaging system, the author applies multiplexed illumination technique. The novel optical system design with computational decomposition algorithm makes it possible to achieve high SBP complex amplitude. Also, the multiplexed illumination technique is applied to the display system to obtain high SBP, especially a wide viewing angle. Here, novel optical design and temporal multiplexing are key ideas. The high SBP allows for the modulation of light based on wave optics more freely, which makes many useful applications in the fields of biomedical,

forensic, VR, and AR more versatile with higher performance.

In Chapter 3, the author proposes the first approach to enhance SBP in the imaging system. As a complex amplitude imaging system, digital holography is adopted with an off-axis configuration. First, conventional digital holography is reviewed with the discussion of SBP. Then, the double-expanded size of the image system without loss of resolution is proposed via the wavelength and spatial frequency multiplexing. The compact optical design is also presented using a single diffraction grating by utilizing the grating's multiple functions such as diffraction, wavelength and polarization dependence.

In Chapter 4, the author adopts a computational imaging technique to obtain high-resolution of complex amplitude imaging. First, the phase lost problem and Fourier ptychographic microscopy are introduced. Then novel optical design using multiplexed illumination and lens array imaging is proposed. The author calls it a single-shot Fourier ptychographic microscopy. The computational phase retrieval algorithm is devised and applied to decompose the multiplexed information. Then, a high-resolution of complex amplitude without loss of size of the image is obtained.

In Chapter 5, the viewing angle expanded holographic display is introduced to enhance SBP in the field of display. In order to overcome the narrow viewing angle of the holographic display, the author adopts structured illumination with a temporal multiplexing technique. With the high-speed synchronization ($>10\text{k}$ Hz) among SLM, light sources, and filter array, the viewing angle expanded holographic video display is implemented without loss of hologram size. The proposed method also reduces speckle noise, and applications of AR and full-color implementation are discussed.

In Chapter 6, the author concludes this dissertation by summarizing the proposed methods with their contributions. Several future researches to improve the proposed methods are also suggested.

Chapter 2. Space-Bandwidth Product

2.1 Overview of Space-Bandwidth Product

In this section, the author briefly explains the space-bandwidth product (SBP). As shown in the word, SBP is the multiplication of the spatial domain's size with the bandwidth of the spatial frequency domain. Let's assume the 2-D optical digital signal is bandlimited and has significant value in the region $-L_x \leq x \leq L_x, -L_y \leq y \leq L_y$. Then the size of the spatial domain corresponds to $4L_xL_y$. The signal's frequency domain is bandlimited by $-B_x \leq f_x \leq B_x, -B_y \leq f_y \leq B_y$, and the bandwidth corresponds to the $4B_xB_y$. Therefore SBP is determined by the multiplication of the two values $16L_xL_yB_xB_y$.

In digital signal processing systems, the signal is sampled by $\delta x, \delta y$. The sampling period should be precisely selected to avoid aliasing and oversampling. If the number of sampling points are N_x and N_y , the size of spatial domain can be written by $2L_x = N_x \times \delta x$ and $2L_y = N_y \times \delta y$ in x and y-axis, respectively. From the Nyquist sampling theorem, the sampling periods are given by $\delta x \leq \frac{1}{2B_x}, \delta y \leq \frac{1}{2B_y}$. This is a condition to avoid aliasing of signals only, and all signals having meaningful values (conditions not to be oversampling) are when the equal sign is established.

Finally, SBP of well sampled digital signal is given by $16L_xL_yB_xB_y = 16 \left(\frac{N_x\delta x}{2}\right) \left(\frac{N_y\delta y}{2}\right) \left(\frac{1}{2\delta x}\right) \left(\frac{1}{2\delta y}\right) = N_xN_y$. The results imply that SBP is a metric that represents the amount of information transmitted through the optical system. The size of spatial domain and bandwidth of frequency have a trade-off relationship, so that both parameters should be increased simultaneously rather than sacrificing another one to enhance the SBP of the optical system.

2.2 Space-Bandwidth Product of Complex Amplitude Imaging Systems

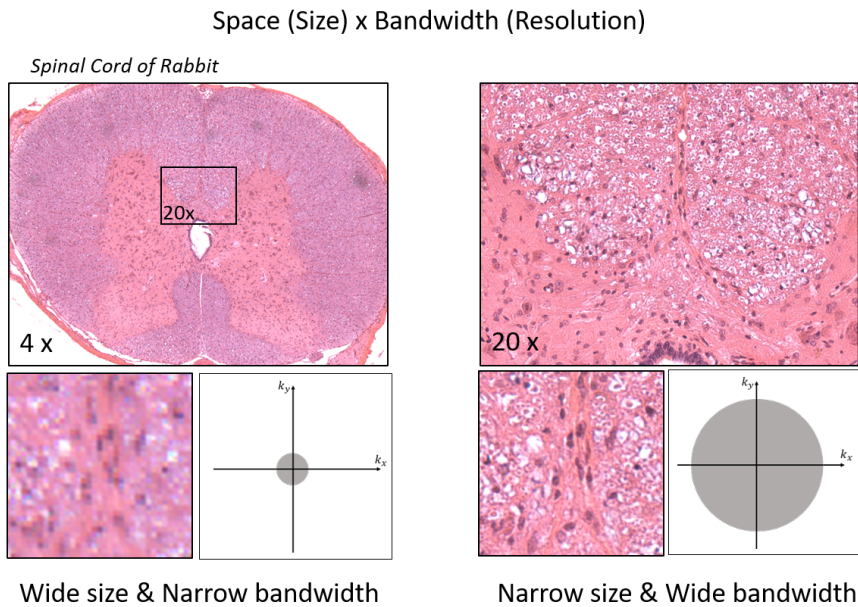


Figure 2.1 Illustration of SBP for the optical imaging systems.

In section 2.1, background knowledge of SBP for the general optical systems is introduced. In this section, SBP for the more specific case of the optical imaging system will be discussed. First, the author introduces SBP of the conventional imaging system (obtain intensity-only) rather than a complex amplitude imaging system. Figure 2.1 shows two cases of the imaging system where the spinal cord of the rabbit is used as a specimen. In the imaging systems, space corresponds to the size of the image. And the bandwidth means the maximum spatial frequency of the image, which corresponds to the resolution of the image. The specimen is experimentally captured by the low-magnification system (4x) and the high-magnification system (20x). Wide size of the image can be

obtained by the 4x system, but it cannot provide high-resolution due to the narrow bandwidth. Using the 20x system, high-resolution but the narrow space image is acquired. Thus, they have followed the concept of SBP, where the two parameters have a trade-off relationship, and the maximum SBP is limited by the number of pixels of the image sensor.

For the complex amplitude imaging system where not only amplitude but also phase should be measured, the SBP suffers more reduction to obtain complex amplitude. The image sensor detects the number of a photon during the exposure time and converts the energy to the image. The energy corresponds to the intensity of the light. The amplitude of the complex amplitude can be obtained by the square root of the intensity profile. But the phase information cannot be obtained from the intensity. Thus, phase retrieval is a crucial topic and there has been lots of studies including digital holography, coherent diffraction imaging, transport intensity equation, and so on [3–12]. However, SBP is generally more reduced to retrieve the lost phase profile comparing the conventional intensity-only imaging technique. Detailed explanation for the phase retrieval techniques is described in Section 4.1.1. Since low SBP corresponds to narrow image size with low-resolution results, it is crucial to study complex amplitude imaging systems with high SBP.

2.3 Space-Bandwidth Product of Complex Amplitude Display Systems

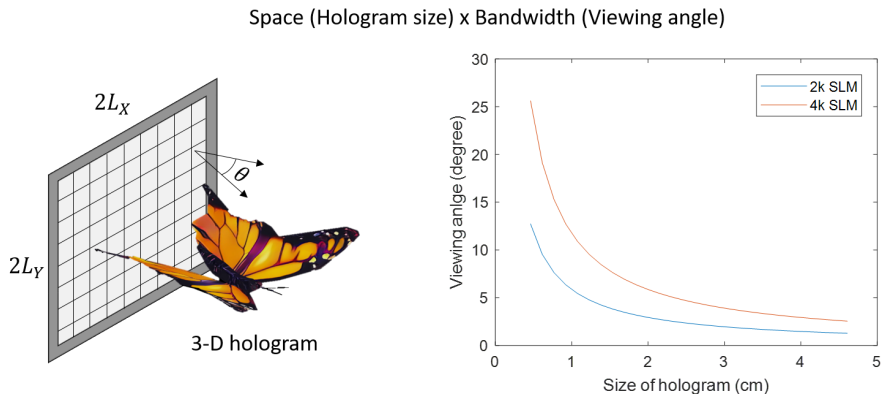


Figure 2.2 Illustration of SBP for the complex amplitude display systems.

Although conventional display provides a 2-D image onto the panel, the complex amplitude display shows a realistic 3-D virtual scene, which is generally called a hologram. An SLM forms the holographic 3-D view via interference and diffraction of the coherent light. Like the image sensor of the complex amplitude imaging system, the SLM comprises a finite number of pixels, where each pixel only presents the amplitude or phase profile. So the amount of information that can be expressed by the SLM is limited. By applying the concept of SBP to the display system, it is possible to derive the relationship between the performance of the complex amplitude expressed by SLM. As mentioned earlier, SBP is defined as the product of a spatial physical quantity and a bandwidth. Here, the space of the display system corresponds to the spatial size of the SLM (2-D size of the hologram) and the bandwidth corresponds to the diffraction

angle from the SLM. The diffraction angle is numerically defined by

$$\theta_x = 2\sin^{-1}\left(\frac{\lambda}{2M\delta_x}\right), \theta_y = 2\sin^{-1}\left(\frac{\lambda}{2M\delta_y}\right), \quad (2.1)$$

where M is the magnification ratio and λ is the wavelength of the light. Here, the size of the SLM is $2L_x = M\delta_x N_x, 2L_y = M\delta_y N_y$. Figure 2.2 shows the complex amplitude display with the trade-off relationship between the hologram size and the viewing angle. The right chart plots the viewing angles for 2k and 4k SLMs when the hologram size changes (M of Eq. (2.1)) at a wavelength of 532 nm. As mentioned earlier, these two parameters are inversely proportional to each other, and only when SBP of the system is improved, the overall display performance can be improved. Therefore, it is crucial to implement high SBP optical system to obtain a large size of the hologram with a wide viewing angle.

Chapter 3. Double Size Complex Amplitude Imaging via Digital Holography

3.1 Introduction

In this chapter, the SBP enhanced complex amplitude imaging system is introduced based on digital holography (DH). Key features of the proposed methods are as follows: The sample's complex amplitude is captured by the off-axis interferometer. The off-axis configuration makes it possible to record and reconstruct the complex value by only a single interference pattern. To enhance the SBP, especially doubling size of the image without the loss of resolution, two multiplexed wavelengths of light sources illuminate the sample. Each wavelength beam is designed to illuminate adjacent region of the sample and occupy different bandwidth to avoid aliasing. And two region of complex amplitudes are reconstructed by the captured multiplexed interference pattern (digital hologram). The author also proposes a novel compact multi-wavelength interferometer composed of only one diffraction grating by using wavelength dependency. Since the interferometer composed of only a single optical element, it has the advantages of low aberration, high stability, and high reproducibility. Compared with the conventional DH system, the proposed system reconstructs twice the SBP of the digital hologram with a hand-carriable compact design.

3.1.1 Digital Holography

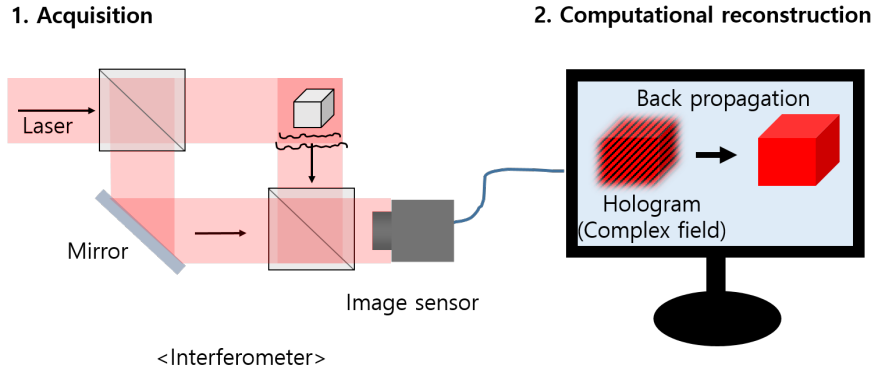


Figure 3.1 Illustration of the conventional DH system.

In this section, the author briefly introduces DH, which is a basic system of Chapter 3. The DH is a label-free imaging technique that can completely measure the complex amplitude of light using interference property [13–17]. The acquisition of complex amplitude provides various applications beyond the conventional imaging systems. For example, it allows to numerically propagate the wave-front over the measurement system’s depth of field that enables quantitative investigation of three-dimensional biological cells [3] and optical elements [18]. DH is composed of mainly two processes: optical acquisition and computational reconstruction, as shown in Fig. 3.1. The holographic acquisition is based on the interferometer, where the Mach-Zehnder and Michelson types are typical examples. Figure 3.1 shows the schematic diagram of the Mach-Zehnder type. This system consists of a collimated laser source, two beam splitters, a mirror, a sample, and an image sensor. The incident laser beam is split for reference and object beams, and these beams are merged by the second beam splitter. The image sensor captures interference patterns. After the acqui-

sition process, the digital hologram is computationally reconstructed to obtain the complex amplitude of the object beam. Once complex amplitude is obtained, the various applications such as back-propagation, the 3-D measurement can be digitally implemented.

DH can be categorized in on-axis [19] and off-axis [4, 20] configuration according to the angle of interference between signal and reference beams. The schematic diagrams of the Mach-Zehnder DH system with the on-axis and off-axis configuration are shown in Figure 3.2(a) and Figure 3.2(b). Let U_o and U_r are the complex amplitude of the object beam and reference beam at the image sensor plane, respectively. The captured intensity profile (hologram) is given by

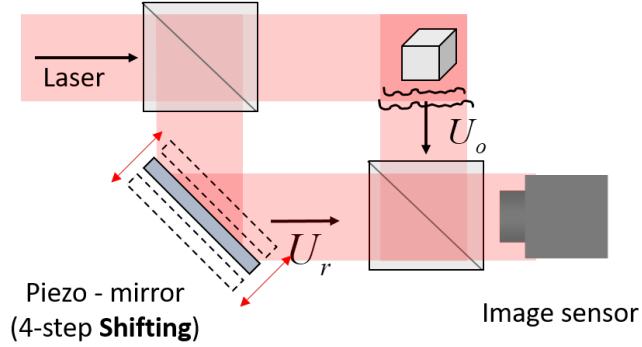
$$I = |U_o + U_r|^2 = |U_o|^2 + |U_r|^2 + U_o U_r^* + U_o^* U_r, \quad (3.1)$$

where $*$ is conjugate operator. From Eq. (3.1), it is conformed that the captured intensity profile is consisted of four terms. The first term corresponds to auto-correlation function of object beam, and the second term is DC of reference beams. The third term is object beam which is multiplexed by conjugate of reference beam and the fourth term is conjugate of the third term. To reconstruct the complex amplitude of object beam, the hologram is computationally divided by the conjugate of reference beam :

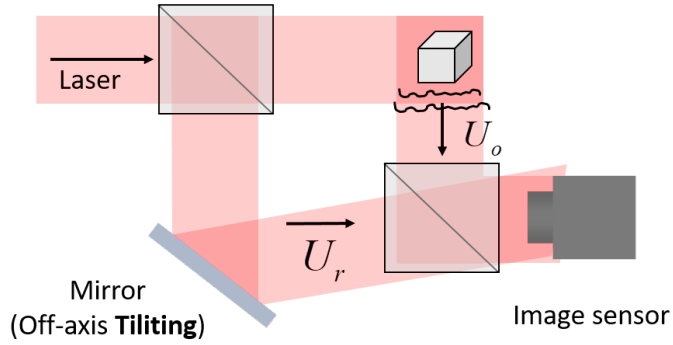
$$\frac{I}{U_r^*} = \frac{|U_o|^2 + |U_r|^2}{U_r^*} + U_o + U_o^* \frac{U_r}{U_r^*}. \quad (3.2)$$

Although the third term of Eq. 3.2 is the object beam's complex amplitude, their exist the unwanted terms that should be removed to obtain object beam only. In the case of on-axis DH, four-step phase-shifting is a representative method to solve the problem. Different holograms are captured as changing the phase of the reference beam. It can be achieved by shifting a piezo-mirror that allows precise control at the sub-wavelength level. The piezo-mirror changes the

(a) On-axis configuration



(b) Off-axis configuration



U_o : Object beam U_r : Reference beam

Figure 3.2 (a) On-axis and (b) off-axis configurations of the conventional DH systems.

optical path of the reference beam by $0, 1/4\lambda, 2/4\lambda,$ and $3/4\lambda$. Then, the phase of the object beam is obtained by $\phi = \tan^{-1} \left(\frac{I_{3\lambda/4} - I_{\lambda/2}}{I_0 - I_\lambda} \right)$. The amplitude can

be obtained as a root value by additionally capturing intensity information after removing the reference beam. $U_o = \sqrt{I_{U_r=0}} \exp(j\phi)$. The on-axis configuration provides a high-resolution hologram without loss of bandwidth. However, it requires five acquisitions for a single complex amplitude (four for phase and one for amplitude). Since SBP is proportional to the number of information, it is trivial that the multi-shot (on-axis) configuration provides high-resolution. However, since the dissertation aims to increase SBP with a novel optical system and algorithm, the approach of simply increasing the number of captures is excluded. Therefore, the author focuses on a single-shot (off-axis) system and takes the number of shots as a controlling variable. Furthermore, the off-axis system has many advantages: First, it collects data without any moving component. Second, single-shot imaging can be adopted in the field of dynamic imaging. Third, it is known to be robust to experimental noises [21, 22].

The off-axis configuration captures a single interference pattern as sacrificing the bandwidth. A mirror is tilted to change the direction of the reference beam as shown in Fig. 3.2(b). Typically the reference beam is directional plane-wave $U_r = A_r \exp(j\mathbf{k} \cdot \mathbf{r})$, where $j = \sqrt{-1}$, $\mathbf{k} = (k_x, k_y, k_z)$, and $\mathbf{r} = (x, y, z)$. The off-axis wave-vector \mathbf{k} makes third and fourth terms of Eq. (3.1) to be shifted in the frequency domain. Figure 3.3 (a) shows an example of the frequency domain when off-axis configuration is adopted. The object beam is band-limited to have bandwidth of BW . In this case, the second autocorrelated term has bandwidth of $2BW$ and the third and fourth terms have bandwidth of BW . The off-axis wave-vector makes the carrier wave-vector of \mathbf{k} and \mathbf{k}^* , which corresponds to the off-axis angle between object and reference beam. From the Fig. 3.3 (a), it can be confirmed that the norm of the off-axis wave-vector $\|\mathbf{k}\|$ should be larger than $\frac{3}{2}BW$ to avoid signal aliasing. If the non-aliasing condition is satisfied, the object term can be retrieved by low-pass

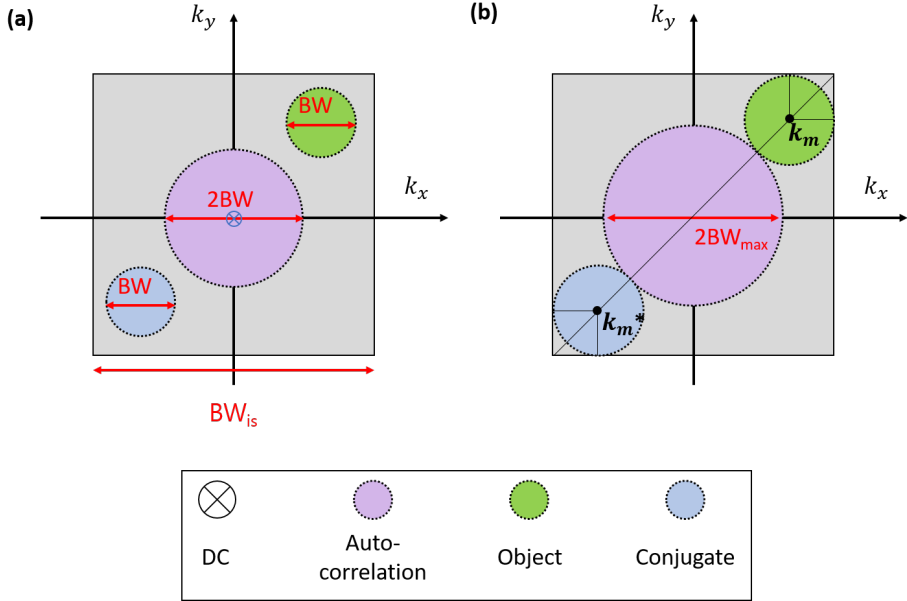


Figure 3.3 Fourier spectrum of the off-axis DH where object bandwidth is in (a) general case or (b) maximum case.

filtering after relocating the carrier frequency of object to the origin. Mathematically, the relocation corresponds to the dividing captured hologram by the conjugate of the reference beam in Eq. (3.2).

$$U_o = LPF \left\{ \frac{I}{U_r^*} \right\}, \quad (3.3)$$

where LPF is the low pass filtering operator whose cut-off bandwidth is identical with BW .

Since off-axis configuration obtains the complex amplitude by frequency filtering, the bandwidth of object beam should be limited. The maximum value is defined when the bandwidth of object beam is in contact with the bandwidth of image sensor and the autocorrelated term at the same time as shown in Fig.

3.3 (b). In this case, the maximum bandwidth is given by

$$BW_{\max} \leq \frac{\sqrt{2}}{3 + \sqrt{2}} BW_{IS} \approx 0.32 BW_{IS}, \quad (3.4)$$

where BW_{IS} is bandwidth of the image sensor. Since SBP is proportional to the 2-D bandwidth with fixed size of the image, the SBP of off-axis DH system is

$$SBP_{DH} \leq \frac{\pi \left(\frac{BW_{\max}}{2} \right)^2}{BW_{IS}^2} SBP_{IS} = 0.08 N_x N_y, \quad (3.5)$$

where SBP_{IS} is $N_x N_y$ (see section 2.2.1).

3.1.2 Frequency Multiplexed Digital Holography

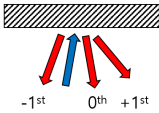
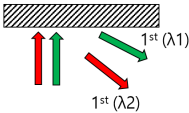
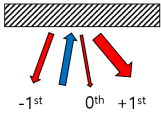
In the post-processing of the off-axis DH, most of the bandwidth is filtered in the frequency domain to remove conjugate and noises. Therefore, the filtered complex amplitude of the object contains a relatively small amount of SBP than that can be acquired by the image sensor. Although the off-axis configuration has useful advantages for practical applications, the limited SBP should be addressed. Since there exists some remaining frequency region that is not used in off-axis DH, more information can be recorded simultaneously by utilizing the area. The multiplexing method is used in a variety of ways, such as reconstructing a phase profile with synthetic wavelength [23–26], acquiring a super-resolution image [27, 28], and capturing an image corresponding to multiple regions [29–31]. Figure 3.4 shows the multiple size of the image expansion cases implemented with two wavelengths of coherent light sources. To avoid signal aliasing between not only object and DC noises but also multiplexed signals, the carrier frequencies of each off-axis DH should be precisely designed. Figure 3.4 (a) shows the frequency domain of the well-designed non-aliasing system. Note that \tilde{U} denotes the Fourier spectrum of U . Two complex amplitudes captured from λ_1 and λ_2 are obtained by the sequential off-axis DH reconstruction process. Although the frequency multiplexing directly improves SBP of the off-axis DH, it requires many optical elements and complicated optical paths because multiple interferometers need to be implemented and, at the same time, satisfy different carrier frequency angles for each wavelength. Figure 3.4 (a) shows the limitation that lots of optical elements such as beamsplitters, mirror, color filters, and neutral density filters construct the complicated dual-wavelength DH system.

3.1.3 Adaptation of Diffractive Grating for Simple Interferometer

For the conventional off-axis DH system, an optical component that splits the beam and at least one additional optical component for tilting a beam is required to implement an interferometer. Despite the significant merits of DH, the performance and the complicated structure of interferometer are considered as main factors that hinder the system from wide use in industry. With the recent development in technology, such as the small pixel size of the image sensor and the high coherency of the light source, it is possible to implement the DH system using a few essential components [32–34]. Although these works alleviate the limitation by reducing the number of optical elements required, a more simple and high-performance system is desired. Furthermore, as discussed in Section 3.1.2, the wavelength multiplexing research requires more optical elements and makes the optical system more complicated.

In Chapter 3, the author proposes an adaptation of a diffraction grating for a simple off-axis interferometer. Since the grating can modulate incident beam of high quality, it has been widely used in DH field for extending the size of the image [35–37], common-path configuration [38, 39], and diffraction phase microscopy [40, 41]. Although the previous studies have used the grating as an additional optical element, the author adopts it to replace essential components of conventional off-axis DH. The author exploits multi-functions of the diffraction grating: First, the grating diffracts incident beam with multi-order, which can be used to split and reflect beams. Second, the grating diffracts the incident light depending on the wavelength, which can be made to have different carrier frequencies for each wavelength. Third, when a blazed diffraction grating is used, each order's diffraction efficiency varies according to the polarization state of the incident light. This characteristic can be applied to match

Table 3.1 Summary of utilized characteristics of diffractive grating.

	Diffracting with multi-order	Wavelength dependency	Polarization dependency
Illustration			<i>*Blazed grating</i> 
Characteristic	Beam splitting and reflecting	Diffraction angle according to wavelength	Efficiency by order according to polarization
Utilization	Interferometer	Carrier frequency multiplexing	Energy matching for interference
Replaced optical elements	Beam splitters, Mirrors	Off-axis mirrors	ND filters

the energy of captured intensity patterns of each wavelength. These features are summarized in Table. 3.1. This substitution simplifies the interferometer with more robust experimental noise because the degree of freedom in alignment is reduced. Moreover, the proposed method does not need a constraint on the specimen, such as sparsity, to use the signal beam as the reference beam because it takes the clear reference beam. Furthermore, the author adopts the wavelength multiplexing method to mitigate the limited SBP problem using two laser diodes without any additional optical components.

3.2 Principle

3.2.1 Single Diffraction Grating Off-Axis Digital Holography

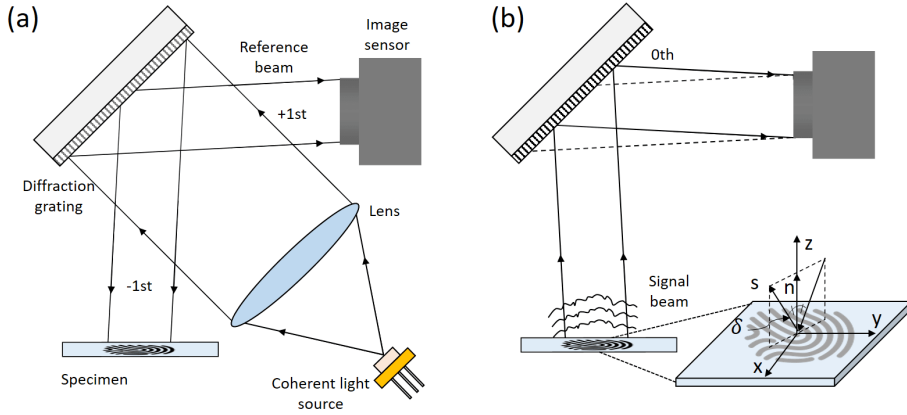


Figure 3.5 Single grating off-axis reflective DH system. (a) After collimated by a lens, normally incident beam is diffracted by the diffraction grating and split into reference and signal beams. (b) The -1st order of beam is reflected on the specimen and interferes with the reference beam on the image sensor.

In this section, a novel approach in constructing a reflective off-axis DH system with a single diffraction grating as a multi-functional component is presented. When the normally incident beam is reflected on the diffraction grating, it is split into several waves. The corresponding diffraction angles are

$$\theta_m = \sin^{-1} \left(m \frac{\lambda}{\Lambda} \right), \quad (3.6)$$

where $m = 0, \pm 1, \pm 2, \dots$, is the index of order, λ is wavelength, and Λ is grating period. A single grating DH (SGDH) method in off-axis configuration is devised with zeroth and first orders of the diffracted beams. Figure 3.5 shows the schematic diagram of the proposed system. The optical system consists of

a coherent light source (LD; laser diode), a lens, one-dimensional diffraction grating, and an image sensor. A diverging beam from LD is collimated by the lens and perpendicularly illuminated on the grating, as shown in Fig. 3.5(a). The incident beam on the grating is divided into ± 1 orders, each of which diffracts from opposite angles. The blazed grating designed to have high grating efficiency in the -1st order is utilized to enhance interference efficiency. In this case, the +1st order of the beam directly enters the image sensor and is used as a reference beam. On the other hand, the -1st order of the beam is incident on the specimen and then reflected back to the grating with signal information. The author sets the specimen plane to have an angle with the reflected signal beam, as shown in Fig. 3.5(b). The normal vector of specimen is \mathbf{n} and the angle difference between the specimen plane and the signal beam is $\boldsymbol{\delta} = (\delta_x, \delta_y)$. The reflected signal beam (s) has a difference of $2\boldsymbol{\delta}$ with an incident beam of the specimen, which results in an off-axis configuration. Then, the signal beam is reflected by the grating through the 0th order and propagated to the image sensor. In the image sensor, the signal beam and the reference beam make an off-axis interference pattern with a carrier frequency as

$$\nu = \frac{1}{\lambda} \sin(2\boldsymbol{\delta}) = \left(\frac{\sin(2\delta_x)}{\lambda}, \frac{\sin(2\delta_y)}{\lambda} \right). \quad (3.7)$$

The number of interference fringe pixel created by the carrier frequency should be more than 2 pixels to satisfy the Nyquist sampling condition. Meanwhile, the number of pixels is also upper limited to mitigate signal aliasing, and 3 to 4 pixels are a reasonable compromise in practical implementation [42]. The angle difference $\boldsymbol{\delta}$ should be bounded by

$$\begin{aligned} \frac{1}{2} \sin^{-1} \left(\frac{\lambda}{4p} \right) &< \|\boldsymbol{\delta}\|, \\ \max(|\delta_x|, |\delta_y|) &< \frac{1}{2} \sin^{-1} \left(\frac{\lambda}{2p} \right), \end{aligned} \quad (3.8)$$

where p is the pixel size of the image sensor. The optical path difference (OPD)

should be smaller than the coherence length of light for interference. The reference beam reaches the image sensor directly after diffracted by the grating, but the signal beam experiences a longer optical path because of the additional round trip to the specimen. The OPD is about twice the distance between the grating and the specimen. In lens-less digital holography, the specimen information of a wider area than the image sensor is measured due to the diffraction of the signal beam. Since most of the signal beam's energy is concentrated on the DC component, the author defines the size of the image as a bright field, and the outer part is filtered during the reconstruction process. Therefore, the size of the image is determined to be identical to the image sensor size.

3.2.2 Double Size Implementation with Multiplexed Illumination

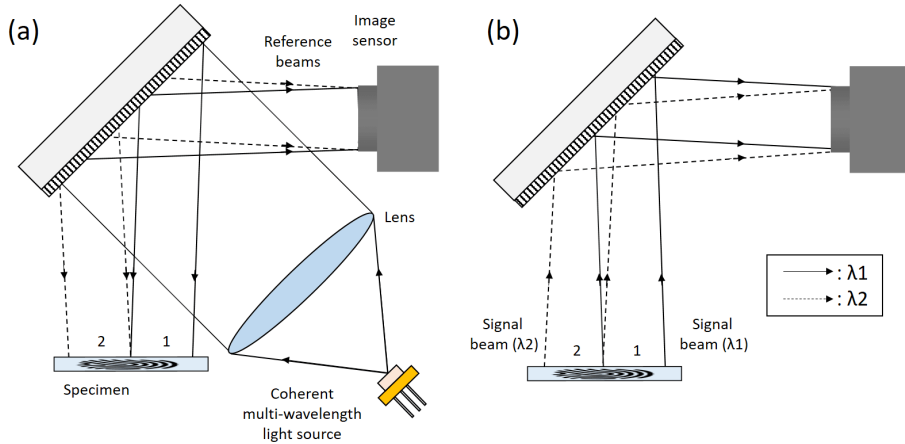


Figure 3.6 SGD with multiplexed illumination system. (a) Two wavelengths of beams are diffracted in different directions. (b) The two signal beams of adjacent regions of 1 and 2 are reflected on the diffraction grating.

In Section 3.2.1, the author presents a method to implement an efficient interferometer using a diffraction grating. Although SGD provides an alternative interferometer with fewer optical components, it is necessary to address the limited SBP of off-axis DH. In this section, a method to obtain a hologram of double SBP (double size of the image with identical resolution) with a single-shot configuration is introduced. The key idea is to use the remaining regions in the Fourier spectrum that are supposed to be filtered in conventional off-axis DH. Inspired by multi-wavelength DH [23–26], the author devises multiplexed illumination SGD aiming for obtaining the hologram with double size of the images. Although methods for multiplexing size of the images have been proposed [29–31, 35], they are not suitable for compact applications because the optical system becomes complicated and bulky to multiplex size of the images

at different carrier frequencies. In the author's approach, however, diffraction grating makes it possible to apply the multiplexing method with its compact system. Figure 3.6 shows the schematic diagram of the proposed double size of the images system. Combining multi-wavelength light source with the lens, two plane waves which have a different wavelength of λ_1 and λ_2 are illuminated on the grating as shown in Fig. 3.6(a). The grating diffracts these waves in the angle of $\theta_{\pm 1, \lambda_1}$ and $\theta_{\pm 1, \lambda_2}$ according to Eq. (3.6), depending on wavelength. Since the diffraction angle from the grating is a function of wavelength, even if the light source system is constructed in line, the beams with two different wavelengths can reach different regions at different angles without additional optics for tilting and shifting. The two -1st order beams are sequentially reflected on the specimen and grating, as shown in Fig. 3.6(b). The reference and signal beams of two wavelengths (total of four beams) make an interference pattern on the image sensor. When λ_1 and λ_2 are mutually incoherent, the measured intensity on the image sensor is given by

$$\begin{aligned}
I(x, y) = & |R_{\lambda_1}(x, y)|^2 + |R_{\lambda_2}(x, y)|^2 + |S_{\lambda_1}(x, y)|^2 \\
& + |S_{\lambda_2}(x, y)|^2 + R_{\lambda_1}(x, y)S_{\lambda_1}(x, y)^* + R_{\lambda_1}(x, y)^*S_{\lambda_1}(x, y) \\
& + R_{\lambda_2}(x, y)S_{\lambda_2}(x, y)^* + R_{\lambda_2}(x, y)^*S_{\lambda_2}(x, y),
\end{aligned} \tag{3.9}$$

where R_λ and S_λ are complex amplitudes of reference and signal beams of λ , and $*$ denotes conjugation operator. The 6th and 8th terms on the right-hand side of Eq. (3.9) can be decomposed separately by spatial frequency filtering. By designing the multiplexing system to satisfy the carrier frequency condition, the author obtains holograms of two adjacent regions while keeping a single-shot acquisition. In order that both images correspond to adjacent regions without overlapping or discontinuance, the distance from specimen to the sensor should

be satisfied:

$$d = \frac{L_y}{|\tan(\delta_{\lambda_1,y}) - \tan(\delta_{\lambda_2,y})|}, \quad (3.10)$$

where L_y is y -directional length of sensor, and $\delta_{\lambda,y}$ is y component of the difference angle with wavelength of λ .

3.3 Implementation

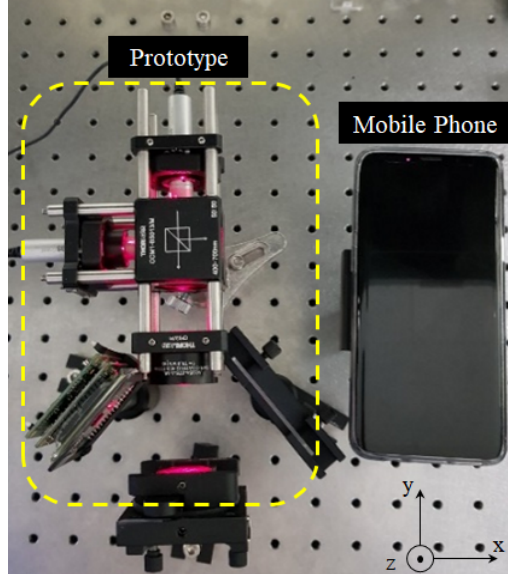


Figure 3.7 Experimental setup of proposed method with multiplexed illumination. The size of the system is measured in the area indicated by the yellow dashed line. The mobile phone is placed next to the system for size comparison.

Figure 3.7 is the experimental setup of the proposed dual-wavelength SGD system. The system consists of two LD modules (Thorlabs, CPS650F and CPS670F, the wavelength of 650 nm and 670 nm), a plano-convex lens (Thorlabs, AC254-075-A-ML, focal length of 75 mm), a diffraction grating (Edmund, 43-210), and a CMOS sensor (Artray, 100MI-USB3-T2, a pixel pitch of $3.34 \mu\text{m}$). The author merges the beams from LDs of two different wavelengths by implementing a beam splitter and a collimating lens to create two plane waves. Note that it is possible to substitute the merged light source with a single LD (without beam combining process) using the commercialized dual or multi-wavelength

LD. The period of the grating is 1200 grooves/mm, which diffracts two normal incidence beams in 51.3° and 53.5° , respectively. The diffraction efficiency varies with the angle between the linear polarization of the incident beam and the direction of the grating vector. The author measures the efficiency for all the linear polarization states and chooses around 60° with a grating vector where the reference beam and the signal beam are of similar intensity. Since these two LDs are mutually incoherent, the multiplexed hologram does not generate interference noise with each other. With multiplexed illumination, a single multiplexed hologram is captured on 1376×1920 pixels of the sensor, which corresponds to $4.59 \text{ mm (H)} \times 6.41 \text{ mm (V)}$. The author sets the angle difference as $\delta_{\lambda_1} = (1.5^\circ, -1.1^\circ)$ and $\delta_{\lambda_2} = (1.5^\circ, 1.1^\circ)$. It makes the signal spectrum of two wavelengths appear at the opposite sides from x -axis. In the author's prototype, amplitudes of the δ are 1.86° for both wavelengths. From Eq. (3.8), the lower bounds are given by 1.39° and 1.44° , and the upper bounds are 2.79° and 2.88° for 650 nm and 670 nm, respectively. Therefore, the system satisfies both conditions. OPD of the prototype is about 10 cm, short enough to achieve interference pattern using LDs. Following Eq. (3.10), The author sets the distance from the sensor to the specimen as 10.5 cm to obtain the adjacent regions of holograms with a minute overlapping. Although the ideal distance is 11.7 cm, the overlapped region helps to stitch holograms and remove edge artifacts. When the distance from sensor to specimen (l) is smaller than d , the lateral overlapped ratio is given by $(100 - 8.4 \times l)\%$. The overall size of the prototype is $12 \text{ cm} \times 17 \text{ cm} \times 5 \text{ cm}$, corresponding to the area indicated by the yellow dashed line in Fig. 3.7. A mobile phone (Samsung, Galaxy 9) is shown to compare the form factor. The author believes this comparison shows the potential that the proposed system can be applied to industrial fields in the form of a hand-carriable form.

3.4 Experimental Results

3.4.1 Resolution Assessment

Figure 3.8 shows experimental results using a 1951 USAF resolution target (Edmund, 51-152). Figures 3.8(a) and 3.8(b) show the captured image and the Fourier spectrum of this image. As the author sets $\delta_{\lambda_1, y} = -\delta_{\lambda_2, y}$, two shifted signals appear at nearly opposite sides in x -axis and are sufficiently separated from each other. The signals are filtered around each carrier frequency, considering the bandwidths. Figures 3.8(c) and 3.8(d) are the frequency filtered images acquired by applying inverse Fourier transform to the noted regions of Fig. 3.8(b). In the reconstruction process, these holograms are digitally propagated to 10.5 cm through the angular spectrum method with the corresponding wavelength. Then hologram with double size of the image is acquired by stitching the two holograms, as shown in Fig. 3.8(e). The area of the image sensor is indicated by the arrows. In this experiment, The author allows ten % overlapped region in the lateral direction between two images to connect the images smoothly. The size of the image of the synthesized image is 6.85 mm \times 8.72 mm, which is 1.9 times larger than the image area of the sensor (6.85 mm \times 4.59 mm). Figure 3.8(f) is a magnified image of high-resolution parts of Fig. 3.8(e). To check the resolution of the proposed system, The author plots the cross-section following the white vertical line. Element 5 of group 5 is resolved, which corresponds to the resolution of 19.69 μm as shown in Fig. 3.8(g). Abbe diffraction limit for coherent illumination is λ/NA , where NA denotes numerical aperture. As the author measures the high-resolution part using a wavelength of 650 nm, the resolution limit of the author's system is 19.94 μm (NA of 0.0326). Therefore, the author confirms that SGDH can provide a high-resolution hologram that accords with the theoretical diffraction limit.

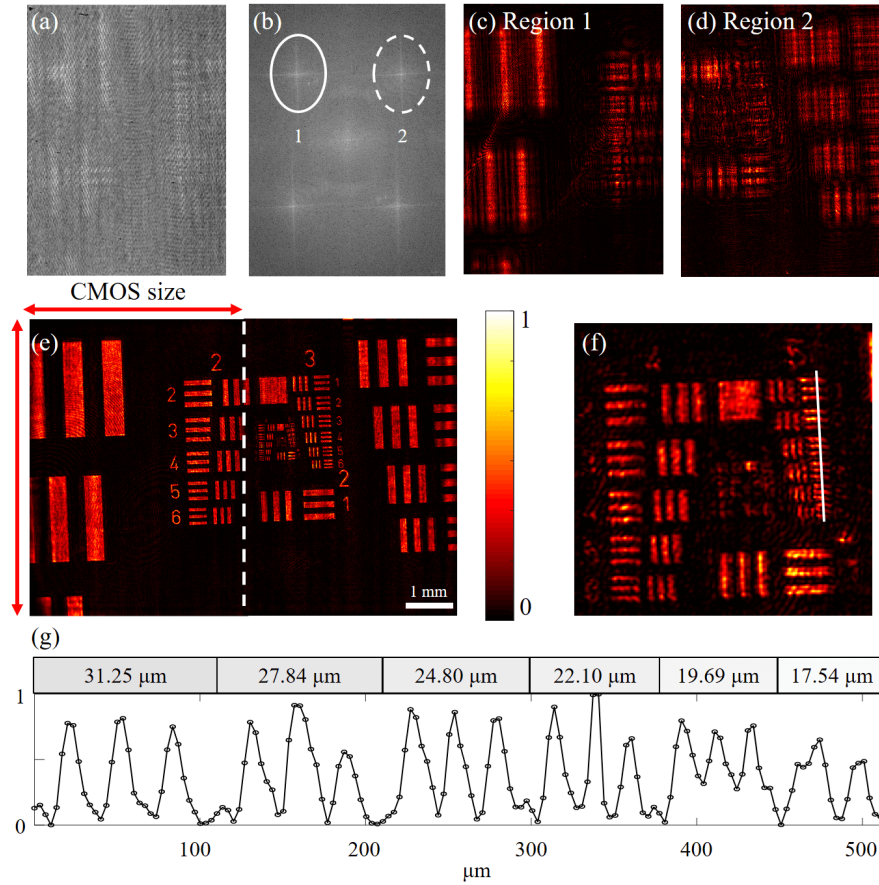


Figure 3.8 Experimental results of 1951 USAF resolution target imaging. (a) The captured hologram and (b) its Fourier spectrum. (c, d) The intensity images of the filtered regions in the spatial domain (e) The stitched double size of the image of the hologram. The size of image sensor is presented using the red arrows. (f) Zoom-in image that presents high-resolution part. (g) The cross-section of the intensity through the vertical line of group 5.

3.4.2 Imaging Result

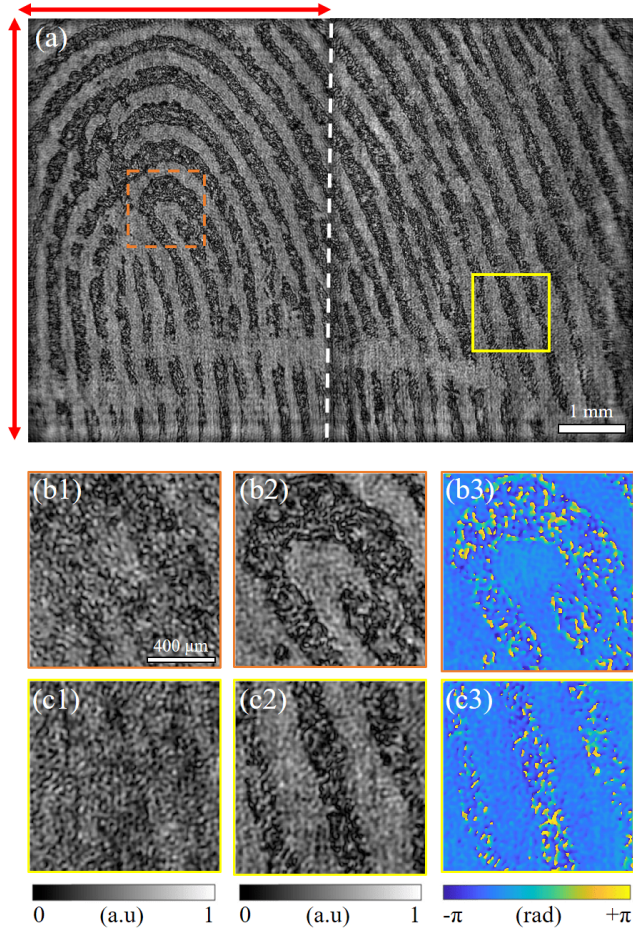


Figure 3.9 Holographic imaging experimental results using the latent fingerprint. (a) Synthesized focus image. (b1, c1) The zoom-in intensity images corresponding to the noted boxes in part (a) before the numerical propagation. Focused zoom-in (b2, c2) amplitude and (b3, c3) phase images reconstructed by numerical propagation.

Next, the author carries out another holographic imaging experiment using a

latent fingerprint on slide glass as a specimen to show the potential use of SGDH in the biomedical and forensic fields. The specimen is made by pressing the thumb on the slide glass, mimicking the process of leaving the actual latent fingerprint. Applied to SGDH with multiplexed illumination, a synthesized image is acquired, as shown in Fig. 3.9(a). The author's method reconstructs double size of the images without degradation of resolution compared to conventional off-axis DH. Figures 3.9(b1) and 3.9(c1) are the enlarged images without the numerical propagation of the orange dashed region and yellow dotted region in Fig. 3.9(a). Figures 3.9(b2) and 3.9(c2) are digitally focused amplitude images that show the core and ridges of fingerprint. Figures 3.9(b3) and 3.9(c3) are phase images.

3.4.3 Quantitative 3-D Measurement

Finally, the author obtains a phase profile of a concave mirror (Thorlabs, CM750-500-G01, focal length is 500 mm) to verify that SGDH provides a quantitative phase profile. Figure 3.10(a) is the synthesized wrapped phase profile acquired by the proposed method, where the left half is the result for 650 nm, and the right half is the result for 670 nm. In order for two phase profiles getting continuous values near the boundary of two images, one of two phase profiles (e.g. ϕ_{λ_2}) is updated to $\arg \{ \exp(j\phi_{\lambda_2}) + b \}$, where \arg is the phase angle operator, and b is the constant bias. The phase profiles are unwrapped by applying the Goldstein algorithm [43] for individual wavelength units. Then, two phase maps of λ_1 and λ_2 are presented with respect to the wavelength of λ_1 . The converted phase profiles can be presented by

$$\begin{aligned}\Phi_1 &= \Phi_{\lambda_1}, \\ \Phi_2 &= \Phi_{\lambda_2} \times \frac{\lambda_1}{\lambda_2},\end{aligned}\tag{3.11}$$

where Φ_λ is an unwrapped phase with a wavelength of λ . The unwrapped phase profile, which is converted to 650 nm is reconstructed, as shown in Fig. 3.10(b). Fig. 3.10(c) plots the cross-section of unwrapped phase profile, labeled by black horizontal line in Fig. 3.10(a). In Fig. 3.10(d), the unwrapped phase profiles of experimental results and theoretical value are shown. It seems that the experimental result is in good agreement with the theoretical value. Theoretical phase profile of concave mirror is given by $k(x^2 + y^2)/2f$ where k is wavenumber and f is focal length of the concave mirror. In addition, the author visualizes the three-dimensional distribution of the reconstructed phase profile, which is a quadratic surface, as shown in Fig. 3.10(e). To quantitatively analyze the phase reconstruction performance, the author presents the reconstructed result using the Zernike polynomials expansion [44]. The Zernike polynomials correspond

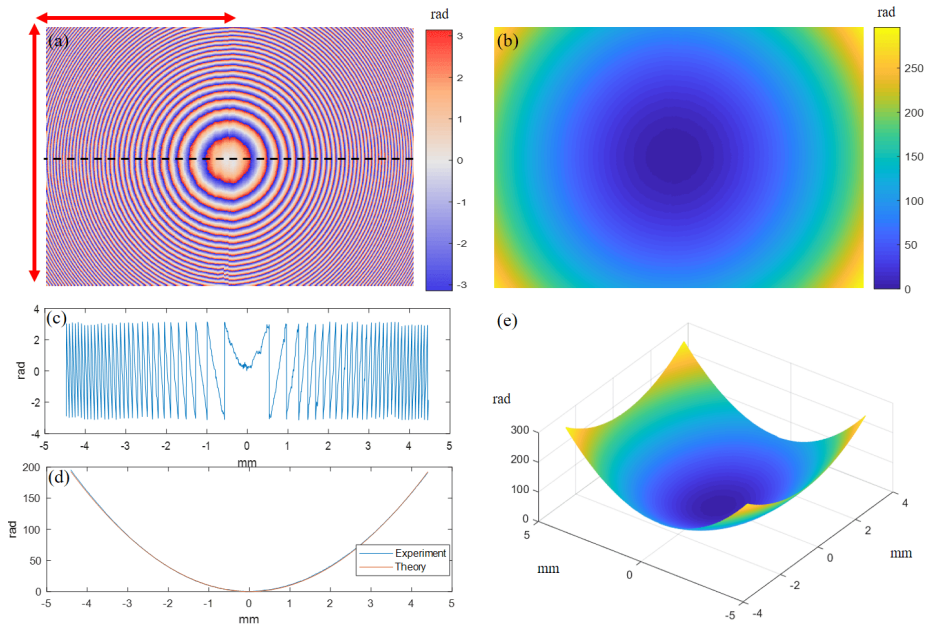


Figure 3.10 Quantitative phase imaging using a concave mirror. (a) The stitched wrapped phase image. (b) Unwrapped phase profile. (c) The cross-section of the wrapped phase along x -axis, which corresponds to the black dash line of (a). (d) Unwrapped phase profile of (c) with theoretical value. (e) Three-dimensional distribution of the reconstructed result.

to orthogonal optical aberrations such as tilt, astigmatism, defocus, coma, etc. By projecting the reconstructed phase map of the concave mirror to the polynomials, it is possible to confirm how the results are optically accurate. The first 12 orders of the Zernike polynomials coefficients without piston ($P=1$) are shown in Fig. 3.11 using the Fringe indexing scheme [45]. From the bar diagram, the defocus ($P=4$) coefficient is the main contribution of the Zernike function for both theory and experiment. It is a reasonable result because the author modeled and measured the spherical mirror. By comparing the relative amplitudes of the coef-

ficients, the optical aberrations of the other terms are negligible, and the results are in good agreement with the theory. Figure 3.12 shows the phase error between the reconstruction result and the theoretical value on a two-dimensional image. It seems that the holograms of the two regions have continuous phase distributions including the vertical boundary. Most regions show phase errors smaller than 2 rad and the edge regions where the largest errors appear about 4 rad. It is confirmed that the proposed method is able to provide quantitative phase profile.

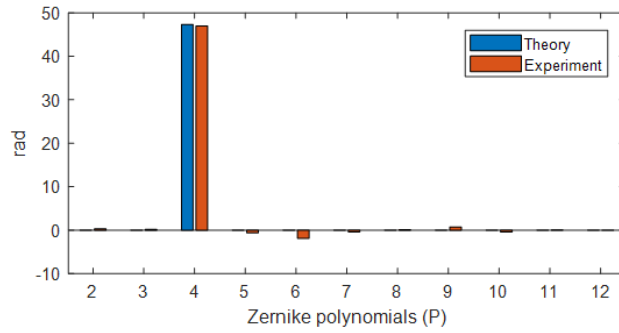


Figure 3.11 Zernike polynomials coefficients of the experimental result and the theoretical model.

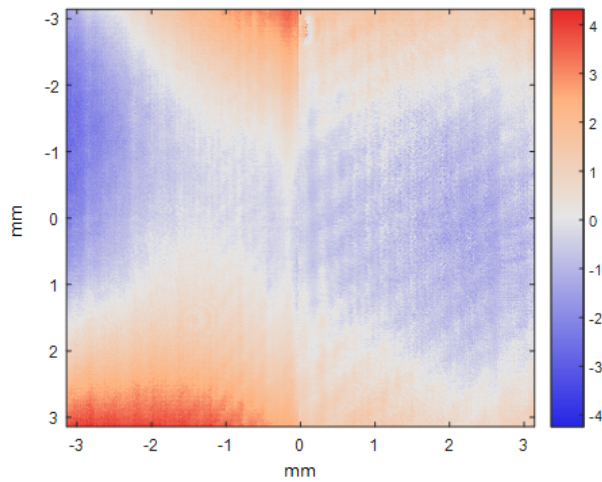


Figure 3.12 Two-dimensional phase error between the reconstructed result and the theoretical value.

3.5 Conclusion

In Chapter 3, the author introduced DH with off-axis configuration as a tool for complex amplitude imaging. To expand SBP, which is considered the system's limitation, the author adopts frequency multiplexing by illuminating the mutually incoherent laser diodes of two wavelengths. The author presented a method to implement a simple interferometer by adopting a diffraction grating. Considering the grating's multi-functional application, the author replaces the beam splitter and the mirror widely used in conventional off-axis reflective DH. Furthermore, the grating wavelength dependence allowed to enhance the SBP of the hologram without additional optical components to make multiplexed beams propagate in different directions. The prototype showed a compact design and provided a hologram of the diffraction-limited resolution and the double size of the image. The obtained hologram is digitally propagated to confirm three-dimensional imaging. Lastly, the author demonstrated that SGDH provided a quantitative phase profile using a concave mirror. The author believes SGDH has potential in various practical uses, including inspection, identification, cell imaging, and where the compact holographic sensing system with high imaging performance is required.

Chapter 4. High-Resolution Complex Amplitude Imaging via Fourier Ptychographic Microscopy

4.1 Introduction

The SGDH showed double expanded SBP of complex amplitude as enhancing size of the image without sacrificing resolution by efficiently utilizing frequency domain. However, the off-axis type DH has a limitation that the SBP of complex amplitude could not reach that of the image sensor because the object beam's bandwidth is limited to avoid aliasing with the central correlation term. In Chapter 4, the author proposes SBP more expanded imaging system based on computational imaging rather than interference. The method provides the spatial resolution and size of the image as the level of conventional coherent microscope maintaining the single-shot condition. This method, termed single shot Fourier ptychographic microscopy (SSFPM), is devised by combination of microscopic imaging methods: Fourier ptychographic microscopy (FPM) [46–55], lens array imaging [56–60] and multiplexed illumination [49–52]. The main novelty of the author's research is that the author only takes a single shot intensity image and unveil phase profile using a computational algorithm. Since the proposed method does not adopt the interference technique, SBP can be more enhanced with a quasi-monochromatic light source. Also, the significance of SSFPM is to overcome not only the trade-off relationship between SBP and the number of measurements but also the requirement of the scanning process in FPM. Using the lens array imaging method, the system collects various angular intensity profiles with a single acquisition. LEDs generate quasi-monochromatic plane

waves rather than diffusive incoherent light so that sub-images formed by the lens array correspond to spatial frequency components for the case of thin samples. In addition, LEDs have advantages of competitive price, compact optical system, and capability of multiplexed illumination. Since FPM requires data redundancy (overlapping in the spectral domain), the author simultaneously turns LEDs on to make a single shot image retain sufficient data for satisfying the convergence condition of FPM. As the sub-images correspond to low-resolution images of conventional FPM, the system can adopt a multiplexed-FPM algorithm and reconstruct wide bandwidth of complex spectrum whose cut-off frequency is equal to the sum of NA of objective lens and illumination angle of the marginal LED. Thus, even if the lens array imaging method degrades each sub-images resolution, the high-resolution of the complex profile is retrieved through FPM reconstruction.

This paper analyzes the constraints for applying FPM with a single shot system and demonstrates the performance of SSFPM using numerical simulation and experiments. By imaging the 1951 USAF resolution target, the author confirms that the prototype represents a resolution of $3.10 \mu\text{m}$ with a wide size of the image of 0.34 mm^2 , which is comparable performance to coherent imaging using a conventional microscope. Besides, a biological specimen experiment is carried out to show that SSFPM can be utilized for quantitative phase imaging.

4.1.1 Phase Retrieval

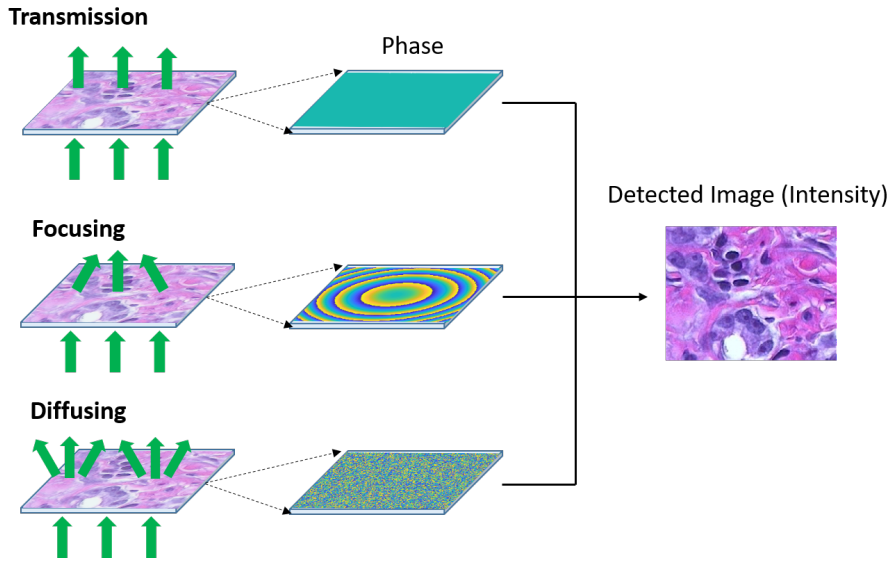


Figure 4.1 Schematic diagram of the phase lost by measuring intensity image.

The complex amplitude of wave $U(r) = a(r) \exp(j\phi(r))$ consists of the amplitude $a(r)$ and phase $\phi(r)$. As briefly discussed in Chapter 1.2, the detected information of the image sensor is the intensity, and thus the phase is lost. Figure 4.1 shows the image acquired when the amplitude is fixed, and only the phase of complex amplitude is changed. It shows that even if the light is transmitted, focused, or scattered due to the phase profile, the acquired information is the same. Therefore, reconstruction of the phase, called *phase retrieval*, is very crucial to understand and modulate the wave fully.

In the imaging field, phase retrieval is a prominent method to discover the 3-D distribution of non-absorbing samples such as biological cells, tissues, and micro-elements [13, 61, 62]. There is research to retrieve phase of transmitted or reflected light, which can be categorized as multiple shots imaging [10–

12, 14, 15, 19, 63–69] and single-shot imaging methods [3–9, 70–74]. Multiple shots imaging techniques, including on-axis DH, transport of intensity equation imaging, and ptychography of coherent diffraction imaging (CDI), are representative methods that recover the complex wavefront by measuring multiple intensity patterns. Although all of these techniques quantitatively retrieve phase while keeping the resolution and size of the image without degradation, they require controllable electrical elements (e.g., piezoelectric actuator) or mechanical scanning parts in their system. Moreover, the requirement of multiple measurements makes them sensitive to small noise during the acquisition process, and the system is restricted to capture the static objects only. On the other hand, single-shot phase imaging is advantageous on dynamic imaging with a high frame rate and tolerance for signal fluctuation during the scanning process. However, in order to retrieve phase profile with a single measurement, conventional methods have limitations that reconstructed results undergo loss of spatial resolution [3–5], size [6, 7], or constraint of high frequency components of the sample [8, 9]. Although there has been research to overcome the trade-off relationship between the number of measurements and SBP, the systems require specific specimen’s kind of sparsity [71, 72], additional object support [73], and massive training complex amplitude data [74].

4.1.2 Fourier Ptychographic Microscopy

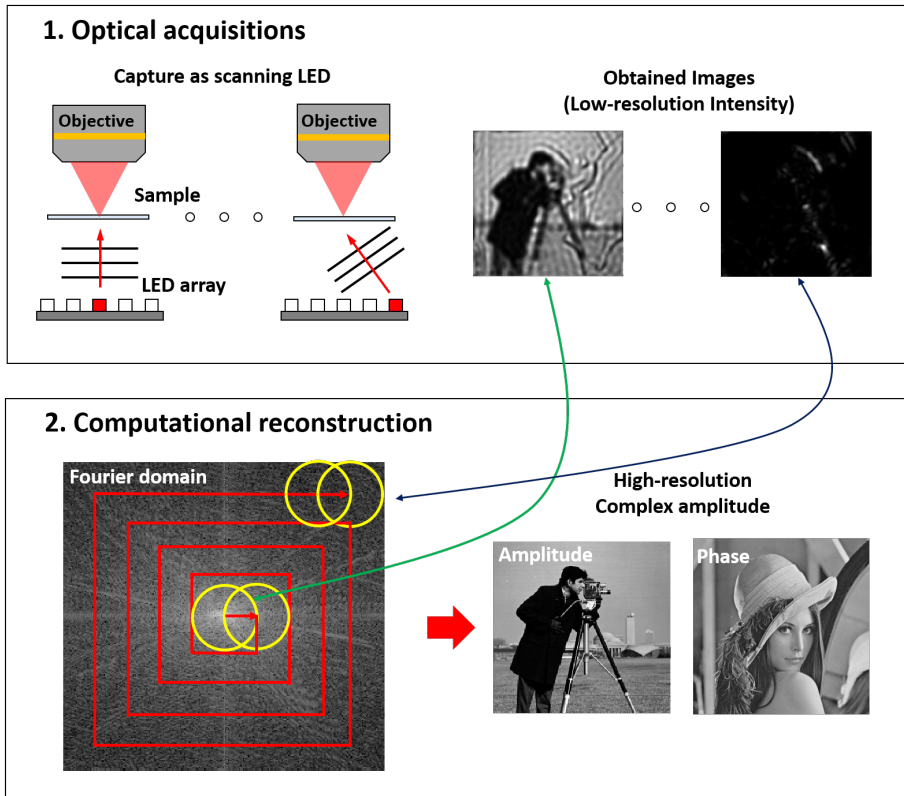


Figure 4.2 Optical acquisitions and computational reconstruction of FPM. High-resolution complex amplitude is reconstructed by multiple low-resolution intensities.

FPM is a computational imaging technique developed in 2013 that reconstructs complex Fourier spectrum with extending bandwidth beyond the numerical aperture (NA) of objective lens [46]. FPM is devised to obtain a gigapixel (high SBP) image whose resolution is $0.8 \mu\text{m}$ with 1.1 mm diameter size of the image. Figure 4.2 denotes the principle of FPM, which can be sequentially

understandable by optical acquisitions and computational reconstruction. The optical set-up of FPM can be easily implemented by replacing a light source of a conventional microscope with an LED array. Since FPM expands bandwidth, the objective lens is generally chosen with a low magnification with a small-NA but a wide size of the image. In the acquisition step, low-resolution images (but wide size of the image) are sequentially captured as scanning the LED array. By assuming that the distance between sample and LED array is long enough considering the size of the image of the sample, the illuminated light from n th LED is considered as plane-wave $\exp(j\mathbf{k}_n \cdot \mathbf{r})$ with a unique spatial frequency \mathbf{k}_n . The spatial frequency is determined by the geometric relationship between the sample and each LED. The imaging method in a microscope can be interpreted as 4f imaging of an objective lens and a tube lens. At the back-focal plane of the first objective lens, the complex amplitude undergoes low-pass filtering determined by the NA of the objective lens after it is Fourier transformed :

$$\begin{aligned}\tilde{O}_n(\mathbf{k}) &= \mathcal{F} \{O(\mathbf{r}) \exp(j\mathbf{k}_n \cdot \mathbf{r})\} \cdot \tilde{P}(\mathbf{k}) \\ &= \tilde{O}(\mathbf{k} - \mathbf{k}_n) \exp(j\mathbf{k}_n \cdot \mathbf{r}) \cdot \tilde{P}(\mathbf{k}),\end{aligned}\tag{4.1}$$

where \mathbf{r} and \mathbf{k} denote spatial and frequency vectors, respectively, \mathcal{F} refers to two-dimensional Fourier transform operator, and $\tilde{O}(\mathbf{k})$ denotes Fourier spectrum of object function. $\tilde{P}(\mathbf{k})$ is pupil function of the objective lens which is a form of circle function :

$$\begin{aligned}\tilde{P}(\mathbf{k}) &= 1 \left(\|\mathbf{k}\| < \frac{2\pi}{\lambda} NA \right), \\ \tilde{P}(\mathbf{k}) &= 0 \text{ (else)}.\end{aligned}\tag{4.2}$$

Note that switching the LED appears as a shift in the frequency domain. Then, the image sensor detects the intensity image after the tube lens performs inverse Fourier transform. The detected image is given by

$$I_n(\mathbf{r}) = \left| \tilde{F}^{-1} \left\{ \tilde{O}(\mathbf{k} - \mathbf{k}_n) \right\} \cdot \tilde{P}(\mathbf{k}) \right|^2.\tag{4.3}$$

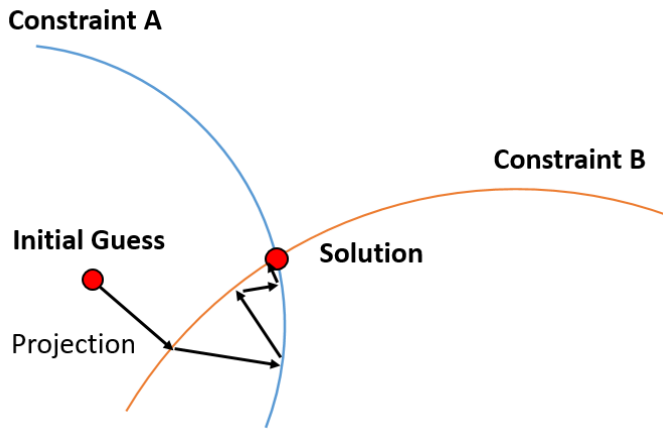


Figure 4.3 Iterative projections on the constraints to find solution.

Next, the measured intensity patterns are used to reconstruct the wide bandwidth of the Fourier spectrum, which has complex value. The main idea of the computational reconstruction is iterative projections of the unknown complex amplitude to the multiple constraints. Figure 4.3 shows the basic concept of the iterative projection, where two constraints have existed. For the FPM reconstruction, the projections are updating the intensity in the spatial domain using the measured image and imposing the pupil functions corresponding to the \mathbf{k} of each LED. The projection can be implemented based on Gerchberg-Saxton approach [75] or Fienup method [76]. To converge the unique solution rather than local minimum, the convergence condition that the intensity profiles should be overlapped with each other in the Fourier domain at least 40% should be satisfied [48]. The detailed reconstruction algorithm of the Gerchberg-Saxton approach is summarized as Algorithm 1.

FPM reconstructs high resolution of intensity and phase profile by stitching

the intensity patterns in the Fourier domain. Nevertheless, the requirement of scanning is the most challenging problem for FPM. There are prior studies that effectively reduce the number of measurements required in FPM using multiplexed illumination [49–51]. Although these previous studies have shown great quality results, taking multiple shots limits their application, including the high-frame rate of dynamic imaging.

Algorithm 4.1 FPM algorithm

Step 1 : Initializing a high-resolution estimation for object function.

$$O^{(0)}(\mathbf{r}) = \sqrt{I_1(\mathbf{r})} \cdot e^{j\phi^{(0)}},$$

where $\phi^{(0)}$ indicates the initial phase. Then up-sample it to generate high-resolution function.

Step 2 : Performing Fourier transform to the object function

$$\tilde{O}^{(l)}(\mathbf{k}) = \mathcal{F} \left\{ O^{(l)}(\mathbf{r}) \right\}$$

and selecting n -th LED's sub-region of this spectrum

$$\tilde{O}_n^{(l)}(\mathbf{k}) = \tilde{O}^{(l)}(\mathbf{k} - \mathbf{k}_n) \cdot \tilde{P}(\mathbf{k}).$$

Step 3 : Updating amplitude using a measured sub-image. In this update process, the amplitudes are changed while the phases are kept unchanged:

$$O_n^{(l)}(\mathbf{r}) = \mathcal{F}^{-1} \left\{ \tilde{O}_n^{(l)}(\mathbf{k}) \right\},$$

$$\Omega_n^{(l)}(\mathbf{r}) = \sqrt{I_n(\mathbf{r})} \cdot \frac{O_n^{(l)}(\mathbf{r})}{\|O_n^{(l)}(\mathbf{r})\|}.$$

Then, updating the object spectrum corresponding to the n -th LED's region :

$$\tilde{O}^{(l+1)}(\mathbf{k}) = \mathcal{F} \left\{ \Omega_n^{(l)}(\mathbf{r}) \cdot e^{-j\mathbf{k}_n \cdot \mathbf{r}} \right\} \cdot P(\mathbf{k} + \mathbf{k}_n).$$

Step 4 : Repeat the step 2 – 3 for all the n .

Step 5 : Repeat the step 2 – 4 l -times until the variation of solution between each iteration is lower than preset threshold value.

4.2 Principle

4.2.1 Imaging System for Single-Shot Fourier Ptychographic Microscopy

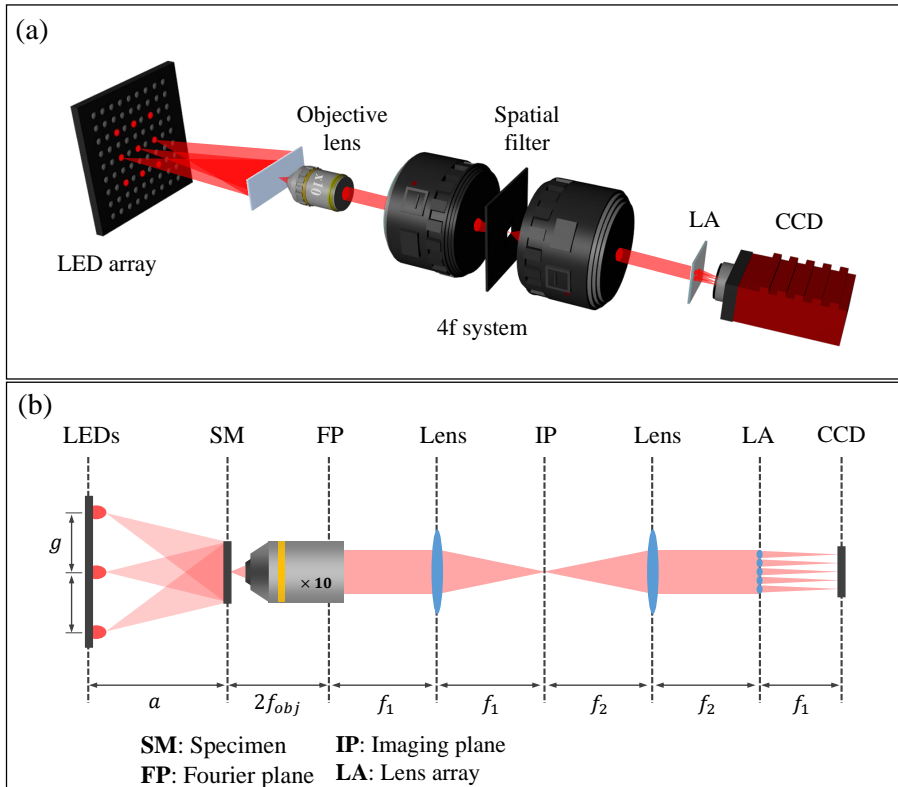


Figure 4.4 SSFPM set-up. The specimen is illuminated by multiple LEDs. (a) Three dimensional schematic diagram of SSFPM. (b) Its corresponding two dimensional diagram.

In Chapter 4, the phase retrieval technique is adopted to obtain the object beam's complex amplitude rather than utilizing the interference of Chapter 3. Conventionally, FPM aims to acquire an image of an enormous SBP with hun-

dreds of acquisitions. The author devises a novel system that applies the FPM to a single-shot complex amplitude imaging system, called SSFPM. The proposed approach provides phase retrieval with high SBP, which is the advantage of FPM, and at the same time overcomes the disadvantage of the FPM, hundreds of shots.

Figures 4.4(a) and 4.4(b) show the experimental set-up and schematic diagram of SSFPM, respectively. Following the basic assumption of the FPM, an LED illuminates a thin specimen in the form of a coherent plane wave within its coherence length range. As the scattered light passes through the objective lens, the objective lens performs Fourier transform by multiplying its pupil function. Thus, the object field passing through the Fourier plane is

$$\tilde{O}_n(\mathbf{k}) = \mathcal{F} \{ O(\mathbf{r}) e^{j\mathbf{k}_n \cdot \mathbf{r}} \} \cdot \tilde{P}(\mathbf{k}). \quad (4.4)$$

The purpose is to place a lens array at the position of the Fourier plane to obtain multiple intensity images corresponding to a different region of spatial frequencies. However, it is not easy to directly place the lens array at the back focal plane because the Fourier plane is generally formed inside the objective lens. Thus, the author implements a 4f imaging system that consists of two lenses with focal lengths of f_1 and f_2 . In addition, there are several advantages to using the 4f system. First, the beam-width of the spectral region, $W = 2f_{obj} \tan \{ \sin^{-1}(\text{NA}_{obj}) \} \times (f_2/f_1)$, can be adjusted by determining the ratio of the focal lengths. Here, f_{obj} and NA_{obj} are focal length and NA of the objective lens, respectively. The beam-width can be appropriately adapted to match the lens array's size and the imaging area of the sensor. Second, a spatial filter can be placed at the first imaging plane (IP in Fig. 4.4(b)). Without the filter, each sub-image appears circular form due to the shape of the exit pupil, and sub-images are arranged periodically following the structure of the

lens array. The author used a long f-number of lens array to make sub-images overlapped and remove the overlapped parts using the square filter. This process allows most of the pixels in the sensor to be efficiently used. Also, a combination of a long f-number lens array and a square filter can alleviate the f-number matching problem occurring in lens array imaging [56–60, 77]. The vignetting effect is also mitigated by magnifying the object to the level of a conventional microscope.

The lens array is located at the relayed Fourier plane, and the CCD sensor measures the intensity pattern at the back focal plane of the lens array. Each lens performs Fourier transform so that the detected m -th sub-intensity pattern in sensor using n -th LED is given by

$$I_{n,m}(\mathbf{r}) = \left| \mathcal{F}_{l,m}^{-1} \left\{ \tilde{O}_n(\mathbf{k} - \mathbf{k}_m) \cdot \tilde{P}_l(\mathbf{k}) \right\} \right|^2, \quad (4.5)$$

where $m = 1, 2, 3, \dots, M$ is the index of the lens array, M is the total number of the lens array, \mathbf{k}_m indicates central spatial frequency of m -th lens, $\mathcal{F}_{l,m}^{-1}$ denotes inverse Fourier transform operator by m -th lens array, and $\tilde{P}_l(\mathbf{k})$ is the pupil function corresponding to shape of lens. This pupil function works as the aperture stop of the objective lens that acts as an object support in conventional FPM. In other words, each lens serves as object support as well as tube lens in conventional microscope. According to Eqs.(4.3) and (4.5), the intensities measured in SSFPM correspond to those measured in FPM. Thus, the detected sub-images can be applied to conventional FPM algorithm.

4.2.2 Multiplexed Illumination

Using a lens array, the author obtains multiple intensity images corresponding to different regions of the spectrum in a single exposure (see Fig. 4.5(a)). Although the images represent different spatial frequency components like conventional FPM, the author cannot directly apply them to the FPM algorithm since they do not satisfy the overlapping condition for convergence of FPM. The structure of the lens array consists of physically separated lenses (the gap between adjacent lenses is represented as Δk_m in the Fourier domain). As each lens performs Fourier transform in its structure, the detected intensities do not have overlapping information in the spectral region. This problem cannot be solved by shifting the lens array position because it only makes additional phase term to the wavefront, which disappears when measuring intensity pattern at the back focal plane of the lens array. To achieve enough information in a single shot, several LEDs are turned on simultaneously, as shown in Fig. 4.5(b1). Even though the light from an LED is considered a coherent wave in their coherence length, the lights illuminated from different LEDs are mutually incoherent. Note that all LEDs are unpolarized light sources. Thus, the m -th sub-image using multiple illuminations appears as the sum of each intensity pattern:

$$I_{N,m}(\mathbf{r}) = \sum_{n=1}^N \left| \mathcal{F}_{l,m}^{-1} \left\{ \tilde{O}_n(\mathbf{k} - \mathbf{k}_m) \cdot \tilde{P}_l(\mathbf{k}) \right\} \right|^2, \quad (4.6)$$

where $n = 1, 2, 3, \dots, N$ is the index of the multiplexed LEDs, and N is the total number of multiplexing states. Each sub-image represents sum of N different intensities spaced at regular interval $\Delta k_1 = 2\pi/\lambda \sin \{ \tan^{-1}(g/a) \}$ in the Fourier domain (see red marks in Fig. 4.5(b)). It has been presented that the superposed information could be decomposed during FPM reconstruction process [49, 50]. Thus, the author decomposes multiplexed sub-images to $N \times M$ sub-images satisfying overlapping conditions. The details are explained in Sec-

tion 4.2.3. In the SSFPM, the LED matrix (index of n) and lens array (index of m) have periodic regular rectangular arrangement, requiring optimal selection of Δk_i to efficiently collect data in a single shot. For example, if $\Delta k_i = \Delta k_m$, the decomposed spectrum sets of red and blue circles in Fig. 4.5(b4) correspond to the same area in the six parts. In this case, they neither constrain each other nor provide sufficient object support to recover phase information. Therefore, the author takes the Δk_i , which is out of the lens array's period in order that the decomposed intensities are overlapped while providing object support as shown in Fig. 4.5(b4). In a similar fashion to previous studies, it is difficult to analytically find and indicate the optimal Δk_i with satisfying the convergence condition while providing enough object support due to the non-linear property of the FPM algorithm. Instead, the author finds a suitable range for choosing the value, which minimizes errors between the reconstructed phase and ground truth using numerical simulation. The detailed process is explained in Section 4.3.

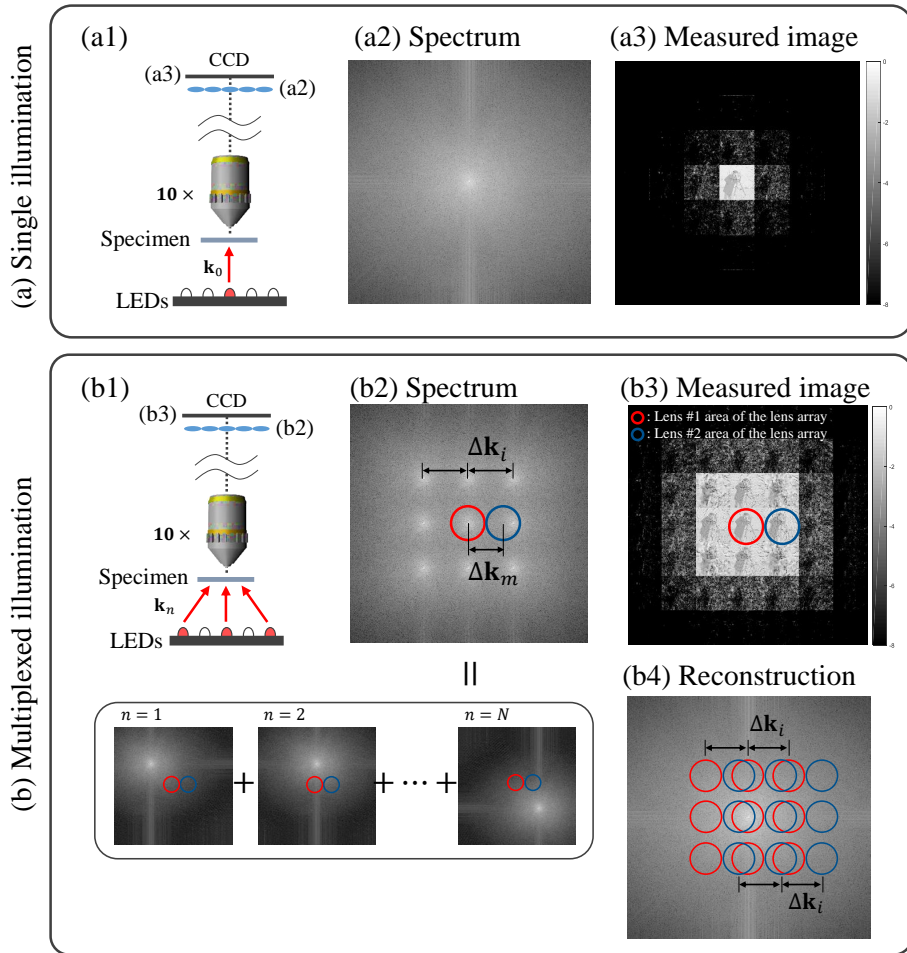


Figure 4.5 The schematic diagram of (a1) single illumination and (b1) multiplexed illumination. (a2, b2) The Fourier spectrum of specimen. Measured intensity pattern in CCD with (a3) single illumination and (b3) multiplexed illumination. (b2) The Fourier spectrum with LED multiplexing. (b4) Fourier spectrum reconstructed by SSFPM.

4.2.3 Reconstruction Algorithm

Algorithm 4.2 SSFPM algorithm (part 1)

Step 1 : Initializing a high-resolution estimation for object function.

$$O^{(0)}(\mathbf{r}) = \sqrt{I_{N,m_0}(\mathbf{r})} \cdot e^{j\phi^{(0)}},$$

where $\phi^{(0)}$ indicates the initial guess of phase. Then up-sample it to generate high-resolution function.

Step 2 : Performing Fourier transform to the object function

$$\tilde{O}^{(l)}(\mathbf{k}) = \mathcal{F} \left\{ O^{(l)}(\mathbf{r}) \right\}$$

and selecting n -th sub-regions of this spectrum corresponding to m -th sub-image,

$$\tilde{O}_{n,m}^{(l)}(\mathbf{k}) = \tilde{O}^{(l)}(\mathbf{k} - \mathbf{k}_n - \mathbf{k}_m) \cdot \tilde{P}(\mathbf{k} - \mathbf{k}_m) \cdot \tilde{P}_l(\mathbf{k}).$$

Then, generating a set of low-resolution object functions by inverse Fourier transform of the images,

$$O_{n,m}^{(l)}(\mathbf{r}) = \mathcal{F}^{-1} \left\{ \tilde{O}_{n,m}^{(l)}(\mathbf{k}) \right\}.$$

Step 3 : Updating the functions' amplitudes using a measured sub-image.

$$\Omega_{n,m}^{(l)}(\mathbf{r}) = \sqrt{\frac{I_{N,m}(\mathbf{r})}{\sum_{n=1}^N |O_{n,m}^{(l)}(\mathbf{r})|^2}} \cdot O_{n,m}^{(l)}(\mathbf{r}).$$

Then, updating the object spectrum through gradient descent method.

$$\tilde{O}_{n,m}^{(l+1)}(\mathbf{k}) = \tilde{O}_{n,m}^{(l)}(\mathbf{k}) + \frac{\tilde{P}_l(\mathbf{k} + \mathbf{k}_n + \mathbf{k}_m) \cdot \left(\mathcal{F} \left\{ \Omega_{n,m}^{(l)}(\mathbf{r}) \cdot e^{-j(\mathbf{k}_n + \mathbf{k}_m) \cdot \mathbf{r}} \right\} - \tilde{O}_{n,m}^{(l)}(\mathbf{k}) \right)}{\left| \tilde{P}_l(\mathbf{k} + \mathbf{k}_n + \mathbf{k}_m) \right|_{\max}^2}.$$

Algorithm 4.3 SSFPM algorithm (part 2)

Step 4 : Repeat the step 2 – 3 for all the m .

Step 5 : Repeat the step 2 – 4 until the variation of solution between each iteration is lower than preset threshold value.

FPM uses the iterative algorithm in which the intensity corresponding to each illumination is updated with the measured intensity data. For multiplexing FPM imaging, a step of decomposing the summated intensity is added in the conventional FPM reconstruction process. The key idea is that a set of intensities $I_{n,m}$ ($n = 1, 2, \dots, N$) are updated to multiplying the measured intensity $I_{N,m}$ by the ratio between the sum of N set of intensity $\sum_{n=1}^N I_{n,m}$ and each intensity $I_{n,m}$. The author extends the multiplexing FPM algorithm and develops the SSFPM reconstruction algorithm to apply the lens array imaging system. The SSFPM reconstruction algorithm is summarized, as shown in algorithm 4.2 and 4.3. The computational cost per each iteration represents $\mathcal{O}(M \cdot N \cdot n_p \cdot \log n_p)$ using big \mathcal{O} notation. n_p denotes the total number of a sub-image's pixels. The computational cost is linearly proportional to the N (multiplexed number of LEDs).

4.3 Implementation

4.3.1 Numerical Simulation

Simulation of SSFPM

The performance of SSFPM is verified using numerical simulation. The system is numerically designed, as shown in Fig. 4.4 with the parameters considering experimental reproduction. The system consists of an objective lens (x10 magnification, $NA = 0.25$), two lenses for 4f system ($f_1 = f_2 = 50$ mm), and a lens array (pitch of 1 mm, $f_l = 30$ mm). The author simulated the case in which 3×3 LEDs ($N = 9$) illuminate an object simultaneously with a wavelength of 630 nm, and the object has complex transmittance, as shown in Figs. 4.6(a) and 4.6(b). The LEDs are placed 145 mm apart from the sample, and the interval between adjacent LEDs is 12 mm. Since the back focal plane diameter of the objective lens is 9.3 mm, central 7×7 lens array ($M = 49$) is used to satisfy $\tilde{P}(\mathbf{k})$ be nearly one. Then, the scattered light is sequentially propagated from the object through the objective lens, 4f system, lens array, and to the imaging sensor. The calculated intensity pattern is displayed in Fig. 4.6(c). Multiplexed illumination makes sub-images have multi-regional frequency information, which can be confirmed through the appearance of the DC bright-field component in the central peripheral images. Next, the intensity pattern is divided into M sub-images. Figure 4.6(d) represents a central sub-image marked in white of the captured image. After generating sub-images, the high-resolution of object function is reconstructed using the SSFPM algorithm, as shown in Figs. 4.6(e) and 4.6(f). SSFPM shows validity to retrieve the phase profile using only a single intensity pattern from the simulation results. Also, the sacrificed spatial resolution due to using lens array is recovered up to the resolution of input complex profiles.

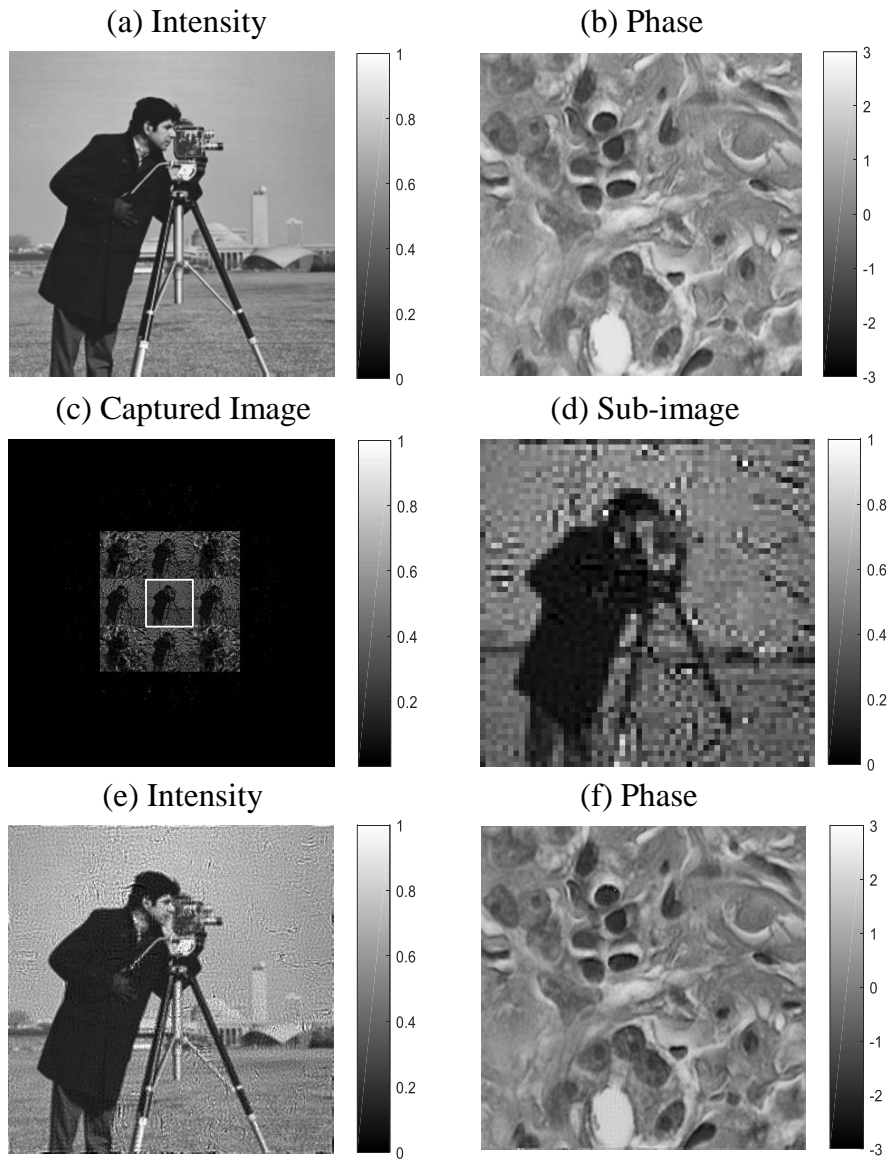


Figure 4.6 Numerical simulation results of SSFPM. The input (a) intensity and (b) phase of complex specimen. (c) A measured intensity pattern. (d) A magnified central sub-image which has low resolution. Applying the measured pattern to the SSFPM, (e) intensity and (f) phase profiles are reconstructed.

Simulation to set Δk_i

In this section, the author simulates how Δk_i affects the reconstruction result of the SSFPM algorithm and select optimal value. Figure 4.7(a) plots the mean squared error (MSE) of the phase between ground truth and reconstructed results by changing the ratio of $\Delta k_i/\Delta k_m$. Figure 4.7(b) exhibits the ground truth images and the reconstructed images for several Δk_i . The reconstructed results near $\Delta k_i/\Delta k_m = 1$ and $\Delta k_i/\Delta k_m = 2$ show high MSE because it does not give enough object support and constrain as described in section 2.B in primary text. In this simulation, there are three minimum points showing smaller phase error near the $4/3$, $3/2$, and $5/3$. Although near the $3/2$ point represents the minimum MSE, in this case, the DC components in Fourier domain are located at the edge of the lens array and severe optical aberration in experiment (the aberration factor is not considered in this simulation). Since the bright field involves most energy for transparent specimen, the marginal position of DC component can degrade quality of reconstruction results. Thus, the author chooses $\Delta k_i/\Delta k_m = 4/3$ considering both reconstruction results and experimental tolerance.

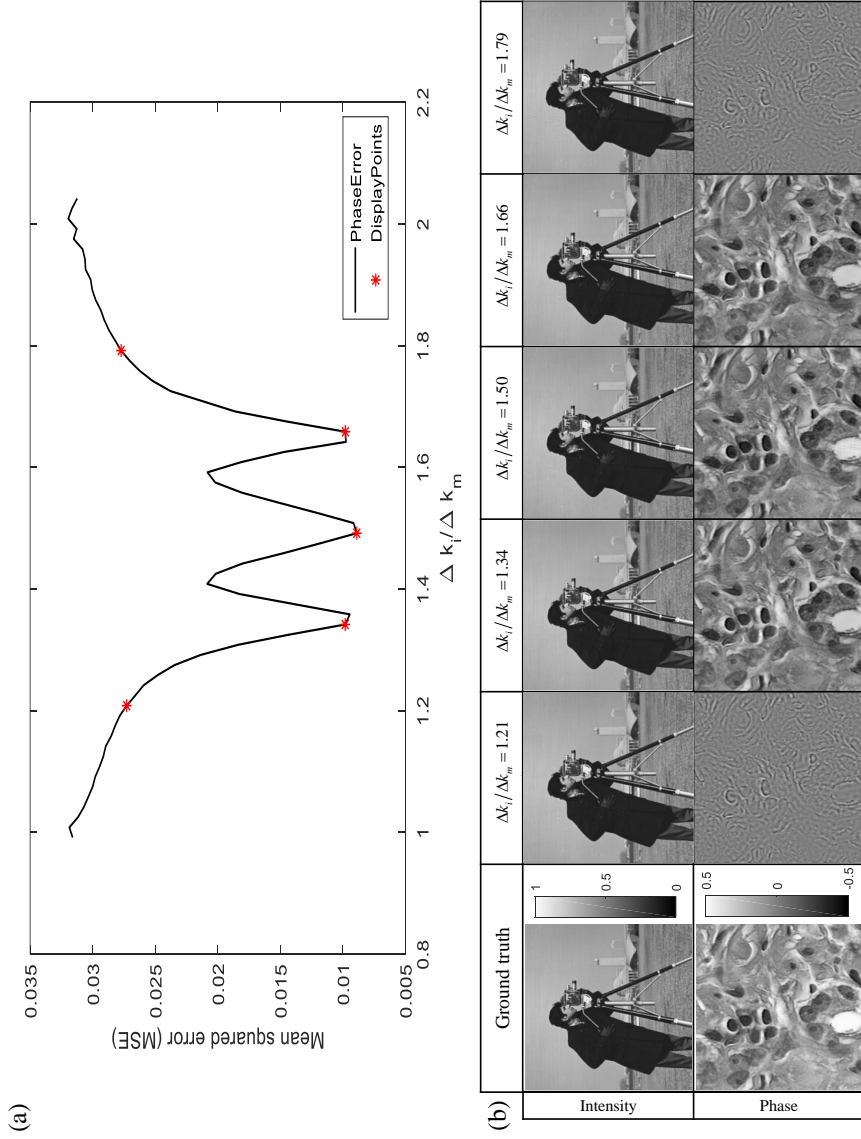


Figure 4.7 Numerical simulation results to select Δk_i ; (a) Plot of the phase error while changing $\Delta k_i / \Delta k_m$ from 1 to 2. Several reconstructed results are displayed in (b).

4.3.2 System Design

Next, SSFPM is experimentally demonstrated using an optical system shown in Fig. 4.4. The system adopts an objective lens (x10 magnification, $NA_{obj} = 0.25$, $f_{obj} = 18$ mm) and a CCD sensor (Pointgrey Grasshopper3) with a pixel pitch of $3.69 \mu\text{m}$ and spatial resolution of 1897×1897 . 4f system is implemented using two aberration compensated lenses (Canon, F1.8, a focal length of 50 mm). An LED array (Adafruit, 6 mm spacing) is placed at 145 mm apart from the sample, and 3 X 3 LEDs (wavelength of 630 nm, the bandwidth of 20 nm) are turned on simultaneously. The lateral gap of LED is 12 mm and the marginal LEDs have lateral illumination NA_m of 0.0825, so that the maximum received NA into the objective lens is $NA_{obj} + NA_m = 0.3325$. Before SSFPM experiments, the calibration process is implemented by placing a diffuser below the specimen. The diffuser leads the measured sub-images to represent not the spatial frequency components but the perspective views, which is a similar concept of integral floating microscopy [58, 60]. The system is optically and computationally calibrated to make all the sub-images appear in the same position using test samples (1951 USAF resolution target and pinhole).

4.4 Results and Assessment

4.4.1 Resolution

After the calibration process, 1951 USAF resolution target imaging is carried out to demonstrate the performance of SSFPM, such as resolution enhancement and convergence of the algorithm. The measured intensity pattern consists of 49 sub-images whose resolution is low because each lens constrains maximum spatial frequency and the number of the pixel, as shown in Fig. 4.8(a). The white dashed figure shows that element 2 of group 6 (71.8 lp/mm, resolution of 13.92 μm) is barely distinguished in the centered bright sub-image. The overall magnification ratio is calculated by $f_l/f_{obj} \times f_1/f_2 = 1.71$. The measured intensity patterns share the region of the sensor so that the effective size of an image is divided by the lateral number of sub-image. Thus, the system has a size of 0.34 mm^2 , which corresponds to the x12 microscope (multiplying the overall magnification ratio with the lateral number). The measured intensity pattern is cropped to generate a set of sub-images and apply the SSFPM algorithm to them. The reconstruction results show that the high-resolution intensity, as well as the phase map, is recovered, as shown in Figs. 4.8(c) and 4.8(d). It is possible to distinguish element 3 of group 8 (287.4 lp/mm, resolution of 3.10 μm), as shown in Fig. 4.8(f). To compare the imaging performance with a conventional microscope, an additional experiment is implemented image, as shown in Fig. 4.8(b). The resolution target is illuminated by a single LED (wavelength of 630 nm) for coherent imaging. In this experiment, the author uses the x10 objective lens (NA of 0.25) combined with a commercialized microscope (Olympus BX53F), and even number of pixels with the single-shot image (1897 x 1897) are used. The Abbe limit for coherent illumination is given by $\lambda/(NA_{obj})$. From Figs. 4.8(g), element 4 of group 8 (362.0 lp/mm, resolution of 2.76 μm) can be

resolved, which accords with the theoretical value of $2.52 \mu\text{m}$. Since SSFPM can restore sacrificed resolution owing to the lens array from $13.92 \mu\text{m}$ to $3.1 \mu\text{m}$ (1.23 times for the diffraction limit and 1.12 times for the experiment result), it is confirmed that SSFPM can provide comparable performance with a conventional microscope.

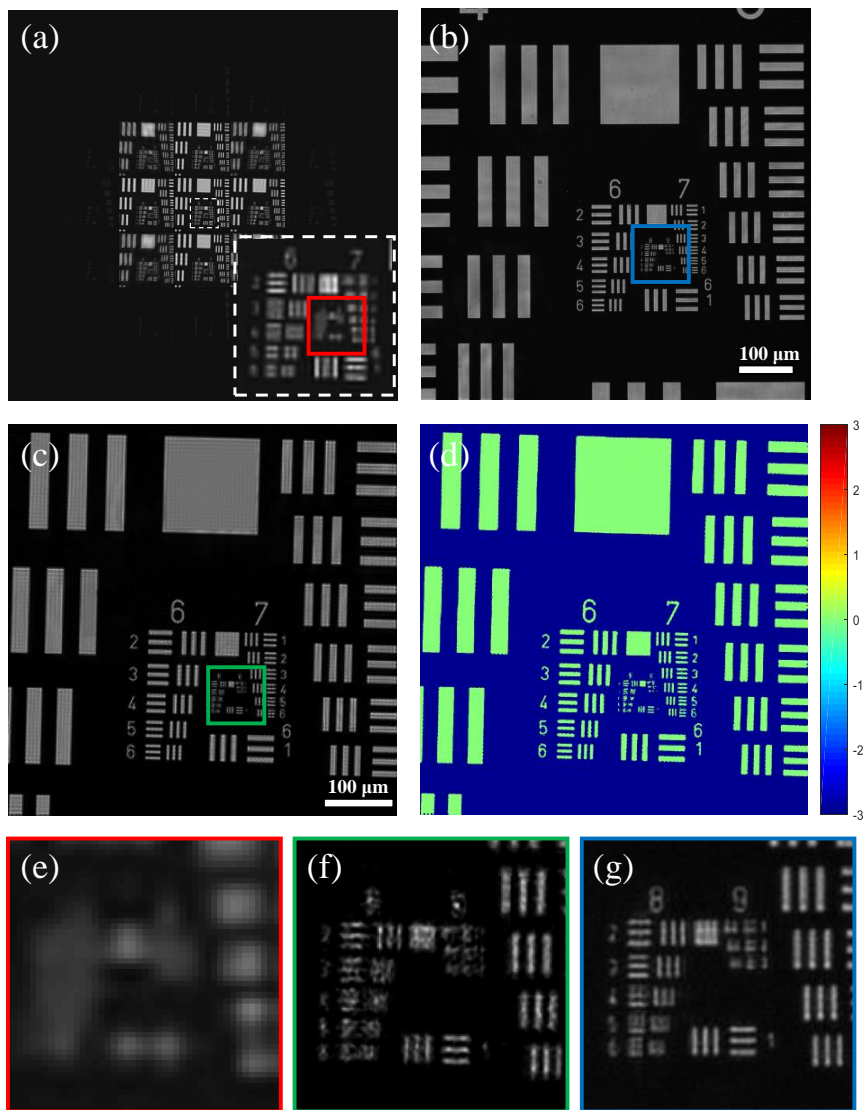


Figure 4.8 (a) The original experimental data from 7 x 7 lens array with turning 3 x 3 LEDs simultaneously on. (b) The image from conventional x10 microscope with coherent illumination. (c, d) The high resolution of reconstruction intensity and phase profiles, respectively. (e-g) The zoom in images of raw data, reconstruction image, and conventional microscope image.

4.4.2 Phase Retrieval of Biological Specimen

Next, biological specimen experiment is carried out using *allium cepa* (onion) epidermal cells to show that SSFPM can be implemented for complex amplitude imaging with 3-D information. The specimen is illuminated by green LEDs (wavelength of 532 nm) and other experimental conditions are identical to the above experiments. Using the SSFPM method, intensity and phase map of the *allium cepa* epidermal cells are reconstructed with size of 0.34 mm^2 as shown in Figs. 4.9(a) and 4.9(b), respectively. The conventional coherent microscope images taken with x10 objective are shown for comparison in Fig. 4.9(c3-e3). In the author's experiment, sacrificed resolution due to using a lens array is recovered up to a conventional microscope, as shown in Fig. 4.9(c1-e1), and the phase profile is retrieved as shown in Fig. 4.9(c2-e2).

To verify SSFPM provides the quantitative phase profile, the author carries out two additional phase retrieval experiments using well-known methods such as phase-shifting DH and transport of intensity equation (TIE) for comparison. Figure 4.10 indicates the three-dimensional distributions of chosen region and schematic diagrams of these methods. It is found that all distributions obviously show the *allium cepa* epidermal cell's 3-D structure, including cell walls and nuclear with periodical structure. Although SSFPM only captures a single image to obtain the phase distribution, four acquisitions are implemented for phase-shifting DH ($\Delta\phi = \pi/2$), and three images are captured for TIE as moving specimen in the axial directions. Considering the number of measurements and SBP of the complex amplitude, it is asserted that SSFPM has competitiveness over conventional phase retrieve methods.

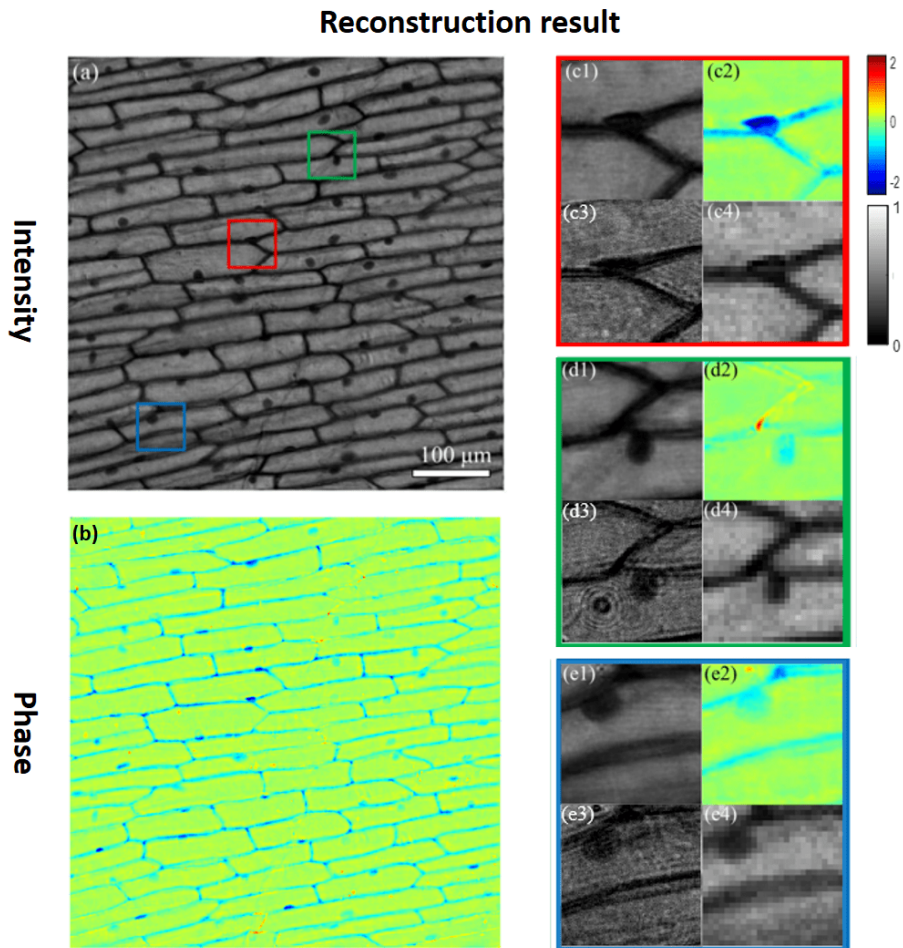
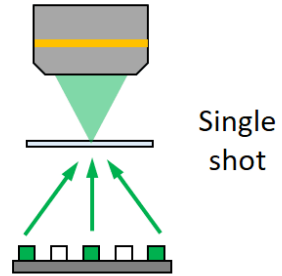
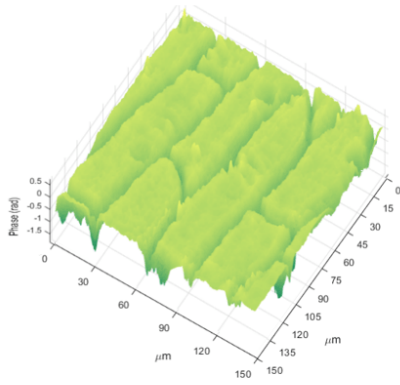
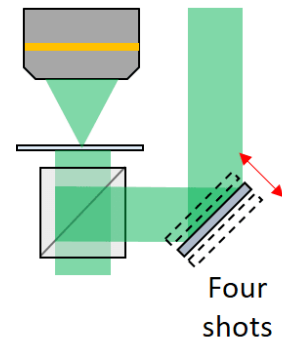
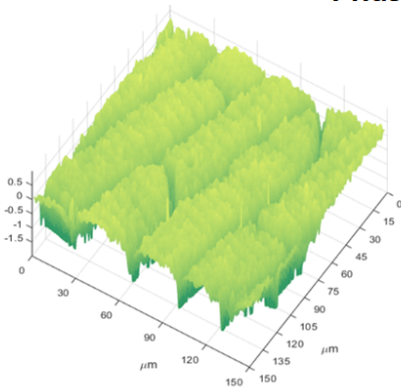


Figure 4.9 Biological specimen imaging using SSFPM. High resolution (a) intensity and (b) phase results. The magnified (c1-e1) intensity images and (c2-e2) phase images corresponding to the regions of red, green, and blue boxes in (a) and (b). (c3-e3) The coherent microscopic images, for comparison. (c4-e4) The raw-data images taken by proposed SSFPM extracted from central bright sub-image.

SSFPM



Phase-shifting DH



TIE

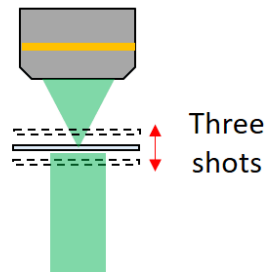
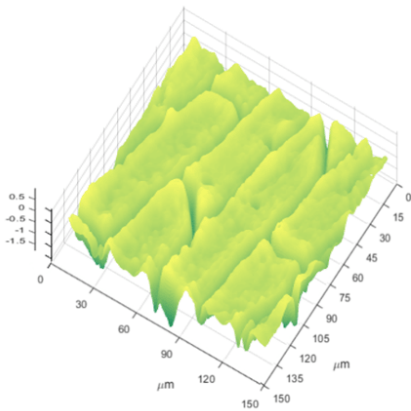


Figure 4.10 3-D Phase distribution recovered by SSFPM, phase-shifting DH, and TIE

4.5 Discussion

The main advantage of SSFPM is that it provides a complex amplitude with high SBP, which is comparable to SBP of the conventional intensity-only imaging technique. Besides, collecting intensity data in the space domain leads to high signal to noise ratio data both bright and dark field image. It allows using partial coherence light by cropping an image to small patches considering coherence length. SSFPM consists of a similar optical system in integral floating microscopy or LFM in the sense that a lens array is used to acquire multiple images in a single shot [58, 60]. In LFM, however, the perspective views of the 3-D thick sample rather than spatial frequency components appear based on ray optics using an incoherent light source (e.g., halogen lamp). Although there is an analysis of LFM based on wave optics, it does not recover sacrificed resolution, which is the fundamental limit of LFM [59]. SSFPM is a method based on wave optics that collect the spatial frequency components of a thin sample as data, and the monochromatic relation between spatial and frequency domain (Fourier transform) can be applied. In other words, the data is not just used to generate perspective views, but synthesizes complex Fourier spectrum based on FPM algorithm, so that SSFPM recovers the resolution of the image up to NA of the conventional microscope with the 3-D profile of the specimen. From another perspective, SSFPM can be considered extended Fourier analysis of coherent LFM with thin samples. FPM can also be applied to restore the refractive index of the thick sample by considering the volumetric coherent transfer function [53]. Since it requires more information and redundancy of data than 2-D FPM reconstruction, SSFPM may have the advantage of applying 3-D FPM with a multiplexing strategy. For instance, the author's prototype obtains 21 x 21 intensity profiles in a single exposure using a 7 x 7 lens array. Also, the author

believes SSFPM generates a more accurate complex profile with less computational costs by optimizing the multiplexing pattern and the lens array structure. Finally, since this method is based on FPM algorithm, SSFPM can be applied in various applications of FPM imaging such as pupil function recovery [47], reflection FPM [54], fluorescence FPM [55], and full color imaging [46].

4.6 Conclusion

In Chapter 3, the complex amplitude is directly acquired by frequency filtering so that the accurate distribution can be obtained with the low-computation cost. Still, there is an upper limit of SBP to avoid aliasing. In Chapter 4, the author obtained a complex amplitude of object wave by restoring phase distribution with a computational algorithm. The proposed method is devised by combining FPM, lens array imaging, and multiplexed illumination. Using lens array and multiplexing strategy, multiple intensity images satisfying FPM's convergence condition are acquired in a single measurement. The sacrificed resolution due to lens array imaging is recovered via FPM so that high resolution of phase and intensity profiles are acquired. The author demonstrates that the performance of SSFPM, resolution, and size of the image is comparable with a conventional microscope by numerical simulations and imaging the 1951 USAF resolution target. Furthermore, SSFPM provides the biological specimen's quantitative phase profile, showing the feasibility of three-dimensional imaging. SSFPM has the potential to improve image quality with aberration correction and be applied in several subsequent researches of FPM and lens array imaging. The author believes SSFPM can provide new possibilities in phase retrieval microscopy in that high resolution of quantitative phase imaging is acquired with a single measurement.

Chapter 5. Viewing Angle Enhancement for Holographic Display

5.1 Introduction

The previous two Chapters are focused on improving SBP in the imaging system, such as DH and computational phase retrieval. As introduced in Chapter 1.1, the complex amplitude fully represents the light in wave optics, so its applications are not limited to the imaging systems only and can be extended to various optical fields. As one method of application to another area, Chapter 5 introduces an extension to a complex amplitude display system. The complex amplitude display can be referred to as a holographic display. Although the former (complex amplitude display) gives unity in this dissertation, the author adopts the latter (holographic display) in order to avoid confusion of understanding by various readers who are accustomed to calling the latter.

In Chapter 5, the author proposes the SBP enhanced holographic display, which provides an expanded viewing zone without losing hologram size. In Chapter 4, the frequency bandwidth is expanded by directional plane-wave illumination with multiplexing. Inspired by the previous work, the author proposes temporal multiplexing (TM) with structured illumination (SI) whose shape of directional plane-wave expands the bandwidth of the holographic display. To implement the concept, the author utilizes a digital micromirror device (DMD) and a laser diode (LD) array for SLM and light sources, respectively. To eliminate diffraction noise from SI, the author utilizes an active filter array for the Fourier filter and synchronize it with the LD array. Also, the speckle noise is

reduced via temporal multiplexing, where the proposed system supports a dynamic video of 60 Hz using the DMD's fast operation property.

5.1.1 Complex Amplitude Representation

Holographic displays are considered the ultimate 3-D displays because they can reconstruct scattered waves from virtual objects rather than 2-D images [78–81]. The multiplication of the viewing angle and the size of the hologram is upper limited due to the SBP of the SLM. In fact, the SBP of the reconstructed hologram should be smaller than that of SLM. The reason is that the SLM can modulate amplitude or phase of wave only, not both. Figure 5.1 shows three representative encoding simulation results, where target complex amplitude $U(x, y) = A(x, y) \exp(j\phi(x, y))$ with its Fresnel hologram and spectrum are shown in the first column. The simplest way to use a phase-only SLM for the complex modulation is to discard the amplitude value. In this case, the amplitude-discarded hologram is $H_1(x, y) = \exp(j\phi(x, y))$. Since the method does not apply any information filtering to obtain the complex value, the SBP of the reconstructed result is identical to the SBP of the SLM without loss. However, the reconstructed results show poor quality due to the absence of amplitude modulation. Double-phase technique proposed to mitigate the problem to modulate both amplitude and phase using a phase-only SLM [2]. Each complex amplitude pixel is expressed by dividing it by the sum of two adjacent phase pixels, which are given by

$$\begin{aligned} H_{DP1}(x, y) &= \exp(j(\phi(x, y) - \cos^{-1}(A(x, y)/|A(x, y)|_{\max}))) \\ H_{DP2}(x, y) &= \exp(j(\phi(x, y) + \cos^{-1}(A(x, y)/|A(x, y)|_{\max}))). \end{aligned} \quad (5.1)$$

The author arranges the two pixels in a mosaic shape to push the noise generated by this method to the edge high-frequency, as shown in Fig. 5.1. Note that even if two pixels are designed as a set, since these two pixels are not physically one, higher-order noise is formed due to interference between adjacent pixels that are not intended for the group. Since two pixels represent one pixel of information,

the SBP is reduced by at least half. The signal must be band-limited and filtered to avoid such high-frequency noise. The red line depicts the bandwidth of the complex amplitude to obtain the reconstruction results. It shows better results compared with the amplitude discard case, but there is still noise, and SBP is reduced by less than half.

The complex amplitude can be encoded using an amplitude only SLM by the SSB method [1]. The idea of this technique is that the sum of a complex number and its conjugate has only the real part. The SSB hologram is given by

$$H_{SSB}(x, y) = A(x, y) \exp(j\phi(x, y) + j\mathbf{k} \cdot \mathbf{r}) + [A(x, y) \exp(j\phi(x, y) + j\mathbf{k} \cdot \mathbf{r})]^* + dc, \quad (5.2)$$

where dc is the minimum value of the sum of the first and second terms, which makes SSB hologram has a positive value. Similar to the off-axis DH in Chapter 3, the complex amplitude should be band-limited and shifted in the frequency domain by carrier frequency of \mathbf{k} to avoid aliasing and obtain pure signal only. The simulation results show when the SSB hologram has maximum bandwidth. The red box depicts the bandwidth to acquire the reconstruction results, which could be implemented by optical 4-f filtering. This method suffers a reduction in SBP by half to represent the complex value, but since it completely restores the original complex value mathematically, the best result consistent with the target can be obtained.

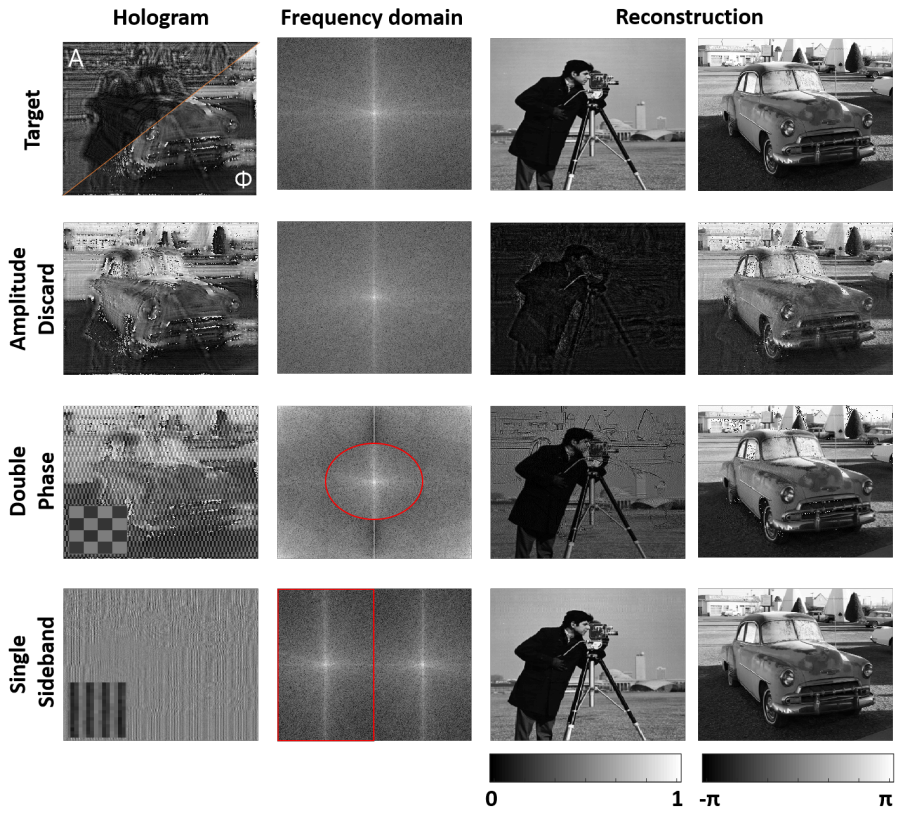


Figure 5.1 Simulations of complex amplitude representations by amplitude discard, double-phase, and single-sideband amplitude encoding methods.

5.1.2 DMD Holographic Displays

Current liquid crystal (LC) based SLMs cannot support enough viewing conditions to the users, such as a wide viewing angle with a large size hologram due to limited SBP. Prior researches proposed spatial [82] or temporal multiplexing (TM) [83] of SLM to increase SBP of the holographic system. However, spatial multiplexing using multiple SLMs makes optical systems bulky and complicated. In addition, the commercialized LC based SLMs suffer from difficulties in applying TM because it can support a frame rate of 60 Hz to 180 Hz. If ten states TM is applied, the LC-based SLMs only provide a display frame rate of 6 Hz to 18 Hz, which allows humans to recognize flickering.

The digital micromirror device (DMD) has recently been adopted for SLM of the holographic display with the advantage of its high-speed operation [84–87]. A DMD is composed of micromirrors that can represent the binary states (1 or 0). It allows the DMD to be used as a binary amplitude modulator with a high-frame rate above 10 kHz [88]. Compared with LC-based SLM, DMD is a suitable device to apply the TM technique because it has a driving speed of several tens to a hundred times faster. Accordingly, the DMD holographic display can improve its performance by designing and engineering the time domain in various ways. For instance, horizontally scanning holographic display, which provides an extensive horizontal viewing angle, is proposed combined with galvanometer scanners [84, 85]. Although the system outperforms conventional holographic display using LC-based SLMs in terms of SBP, there exist several issues such as one-dimension only scanning and stability of the physical movement. Moreover, speckle noise, a fundamental problem of holographic displays, and binarization noise occurring in binary displays cannot be mitigated.

In this dissertation, the author proposes a high-quality holographic display

that mitigates this noise while improving SBP through engineering the time domain. Although the proposed system is focused on a monochromatic panel type device, the author introduces other applications that provide full-colors in a near-eye configuration in the discussion session.

5.2 Principle

5.2.1 Structured Illumination

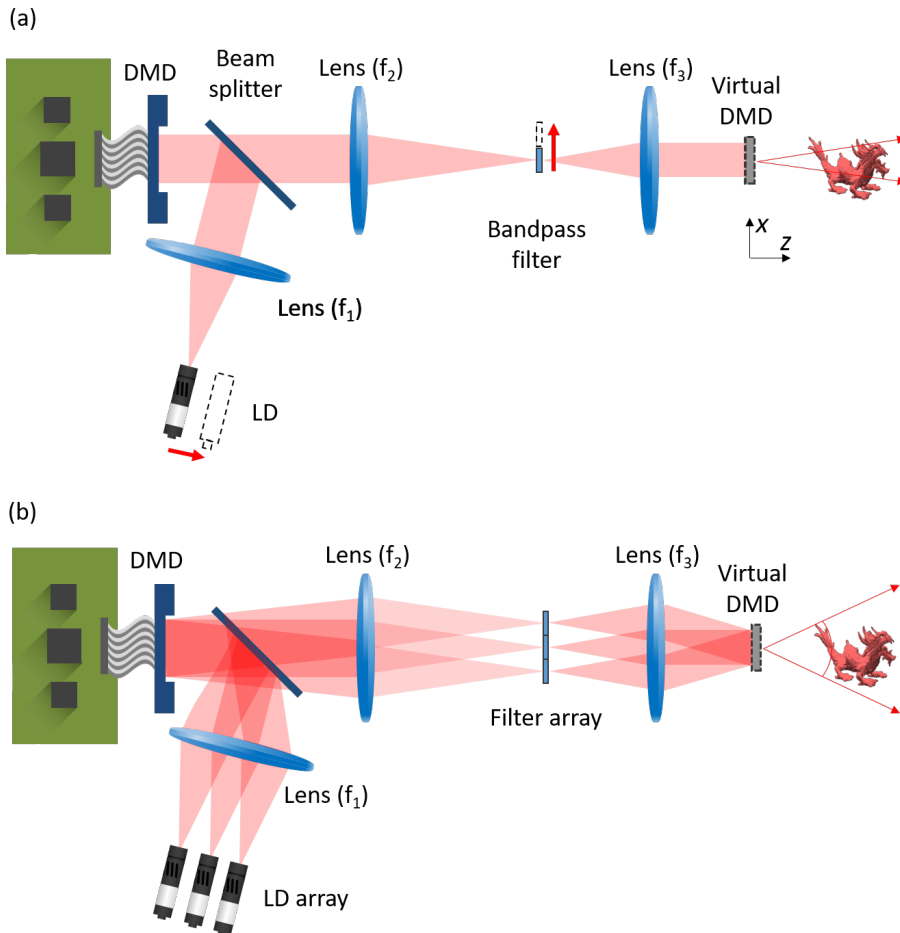


Figure 5.2 Schematic diagram of (a) the conventional and (b) the proposed TM DMD holographic display.

First, the author applies the directional illumination to expand the viewing angle, inspired by the structured illumination microscopy (SIM), which is already explained in previous Chapter 4 [21, 89, 90]. The concept of SIM is that

directional plane wave illumination leads to a shift of the specimen's Fourier spectrum. If the DMD is illuminated by the (i, j) th directional plane wave, the Fourier spectrum of the hologram on the DMD is given by

$$\tilde{H}_{ij}(\mathbf{k}) = F \left[h_{ij}(\mathbf{r}) \times e^{i\mathbf{k}_{ij}\mathbf{r}} \right] = H_{ij}(\mathbf{k} - \mathbf{k}_{ij}), \quad (5.3)$$

where \mathbf{r} and \mathbf{k} are spatial and frequency vectors. \mathbf{k}_{ij} denotes k -vector of the illumination and F is Fourier transform operator. The h is the binary signal which is sampled by pixelated structures of the DMD. From Eq. (5.3), it is found that the Fourier spectrum could be shifted by changing the illumination \mathbf{k}_{ij} without spatial movement. Figure 5.2(a) shows schematic diagram of conventional DMD holographic display. \mathbf{k}_{ij} is determined by the relation between focal length of the collimating lens (f_1) and spatial location of the LD. The lateral shift of the LD while maintaining the position of the lens alters \mathbf{k}_{ij} , depicted as dot lines with red arrows. However, the position of the bandpass filter also needs to be adjusted because Fourier spectrum including signal with diffraction noise is shifted together. It is difficult to implement because the LD and the bandpass filter should move at high speeds corresponding to the level of display frame rate with synchronization.

5.2.2 TM with Array System

As a more practical approach, the author uses the light source and filter as an array rather than a single component. The schematic diagram of the proposed array system is shown in Fig. 5.2(b). Note that Fig. 5.2(b) shows TM image, and the LD array and filter array are synchronized with the DMD. Each component of the LD array and filter array can be actively operated by electrical signals. By adopting the array structures, the directional illumination with proper noise filtering is realized by temporal switching of the arrays without spatial movement. Back to the Eq. (5.3), the Fourier spectrum is multiplied by the filter array, and the inverse Fourier transform is operated through a lens (f_3). The TM profile (h_{TM}) on the virtual DMD becomes

$$h_{TM} = \sum_{i,j} F^{-1} [H_{ij}(\mathbf{k} - \mathbf{k}_{ij}) \cdot M_{ij}(\mathbf{k})], \quad (5.4)$$

where M is the mask profile of the filter array. By matching \mathbf{k}_{ij} with bandwidth of the DMD, entire bandwidth can be expanded in proportion to the number of illumination ($i \times j$). The expanded bandwidth makes the viewing angle of the hologram wider.

5.2.3 Time Domain Design

According to Eq. (5.4), the viewing angle (bandwidth of the spectrum) may seem to be continuously expandable by considering only the number of arrays. However, conventional lenses have a limited acceptable NA and suffer from serious optical aberrations at the edges. In order to efficiently utilize the fast driving speed of DMD without waste, the author designs some frames to improve SBP and uses the rest to improve hologram quality. The author adopts the temporal speckle reduction method while expanding the proposed viewing angle expansion method. The temporal speckle reduction preserves spatial resolution and depth of field of the hologram. The author uses the factor of speckle contrast (C) to analyze the amount of speckle noise. The speckle contrast is calculated by dividing the standard deviation of the intensity by the mean value. It is reduced as proportional to the inverse square root of the number of synthesized independent holograms if the holograms are added during a single frame. The author generates the holograms with different random phases to avoid correlation of the speckle patterns. Then, the holograms are temporally multiplexed in a frame as long as each LD and corresponding filter are activated. The maximum number of speckle reducing frames is calculated by dividing the DMD frame rate by $i \times j \times f_o$, where f_o is output frame rate of implemented system. For instance, 36 sub-holograms can be multiplexed in 60 Hz display conditions and six times viewing angle expansion and 12,987 Hz frame rate supporting DMD. Then, the speckle contrast can be reduced 1/6 times. Note that since each filter and LD are still activated during the speckle reducing frames, they require only the frame rate of 360 Hz ($3 \times 2 \times 60$).

5.3 Implementation

5.3.1 Hardware Design

The prototype is designed and implemented for the demonstration of the presented method. The DLP9000X model from Texas Instruments is used for DMD, whose resolution is WQXGA (1600×2560 pixels), and pixel pitch is $7.56 \mu\text{m}$. The author customized the LD array by mounting six ($i = 1, 2, 3$ and $j = 1, 2$) commercialized LD modules (Thorlabs, CTF635F, wavelength of 635 nm). The linear polarization state of each LD is controlled by rotating LD module to achieve maximum diffraction efficiency from DMD. Focal lengths of the lenses (f_1 , f_2 , and f_3) are 125 mm, 200 mm, and 100 mm, respectively. The filter array is also customized by attaching commercially available polarization shutters (LC-TEC, PolarSpeed-S-AR), where periodic pitch between each shutter (p) is 13 mm. Each shutter provides the high-frame rate of 540 Hz, making it suitable for use with the proposed TM method. This feature allows the viewing angle to be expanded up to nine times with a 60 Hz display.

5.3.2 Frequency Domain Design

Figure 5.3 shows the sideband encoding strategy with the diffraction noise filtering method. In this prototype, the filter array passes bottom sidebands for bottom views ($j = 1$) and top sidebands for top views ($j = 2$). Since the opposite side of the Fourier spectrum is conjugated, the author pre-conjugates the hologram of top views to compensate for it. When commercialized SLM is used, the shape of the sideband is a rectangle with a 2:1. To match the shape with the shutter used in this paper, i.e., square shape, the author applies an anamorphic transform to change the Fourier spectrum ratio [91]. The anamorphic transform system is composed of a lens ($f = 100$ mm), two x -cylindrical lenses ($f = 150$

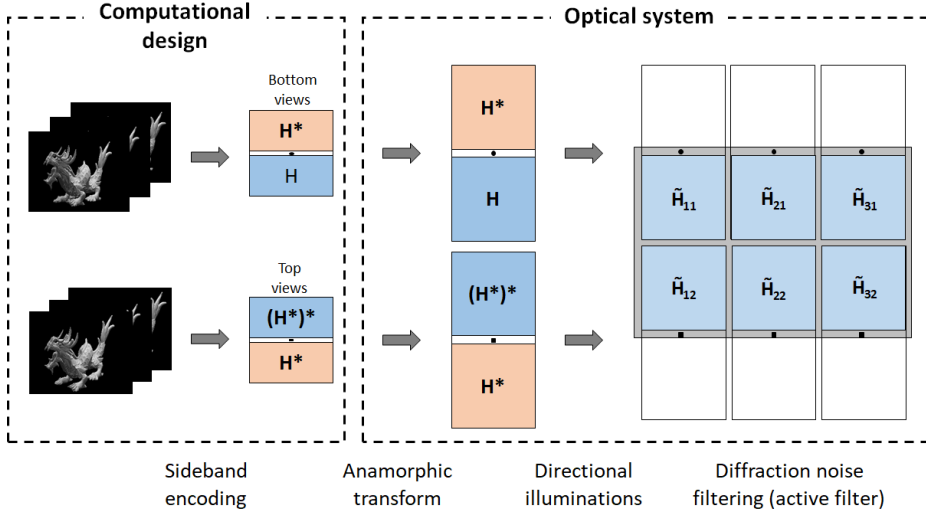


Figure 5.3 Frequency domain design to utilize the filter array. The sideband encoding and the anamorphic transformation are implemented to match the structure of the filter array. The DC components are blocked using the bezel of the array.

mm), and a y -cylindrical lens ($f = 75$ mm), located between the DMD and the lens (f_2) in Fig. 5.2 (omitted for simplicity). The magnifications of the anamorphic system are $m_x = 1.50$ and $m_y = 0.75$. Then, the author designs the pitch between each LD (d) to match the spatial shifts of the Fourier spectrum with the period of the filter array (p). The d is set as 12.2 mm when p is 13 mm by the relation of $d = f_1 m_x p / f_2 = 2 f_1 m_y p / f_2$. The spatial size of the single-sideband for each illumination is calculated by $w_x = 2 f_2 \tan [\sin^{-1}(\lambda / 2 q m_x)]$ and $w_y = f_2 \tan [\sin^{-1}(\lambda / 2 q m_y)]$, where λ is wavelength and q is the pixel pitch of DMD.

5.3.3 Aberration Correction

Although the proposed method expands viewing angles corresponding to the directional illumination, the expanded wavefront suffers optical aberrations due to the deviation from the optical axis. The author pre-compensates the aberrations arising from the optical system by modulating the phase-profile of the hologram. The author experimentally obtains the correction phase profiles through the Zernike feedback algorithm [78, 81]. The coefficients of several major aberrations (tilt, defocus, and astigmatism) are acquired in the implemented system to make the sharpest point spread function at the intended 3-D space. Since the optical aberration functions are spatially variant, it is required to obtain the correction phase functions for every 3-D object point. However, to find and apply the correction functions for all points is impractical because over two million pixels of DMD requires too high computational costs. Assuming that the aberration function is smoothly variant and the differences in depth are negligible, the author only obtains a total of six global correction functions, each corresponding to the central 3-D point of each illumination. Then correction is applied using each global correction phase map for each illumination. The $4f$ relay system is implemented using aberration-corrected camera lenses (Canon, F1.8, f_1 of 200 mm and Zeiss, F2.0, f_2 of 100 mm) to support the assumption of slow-varying variation.

5.4 Results

The author displayed the holograms blended from intensities and depth maps of six orthographic views. The holograms are generated by layers-based method [92], where they are sliced by 32 depths and have depth range from 0.5 cm to 1.4 cm after the relayed virtual DMD. The size of the hologram is $9.1 \times 7.3 \times 0.9$ mm³. The experimental results are captured using a CCD sensor (FLIR, GS3-U3-91S6C-C) adapted with a C-mount lens (Nikon, AF Micro Nikkor 60mm F2.8). The shutter speed of the image sensor is set as 1/60 seconds for all the results in this Chapter. Figure 5.4 is an example of the experimental result showing the process and effect of the aberration correction. Figure 5.4(b) shows that

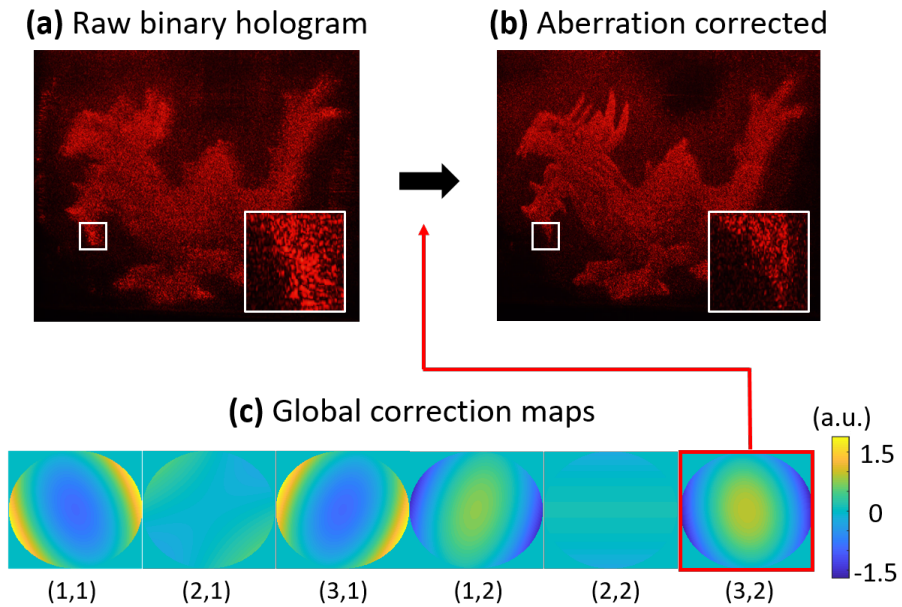


Figure 5.4 (a) An example of captured image from raw binary hologram. (b) The aberration corrected result using a correction map. (c) The pre-measured global correction maps.

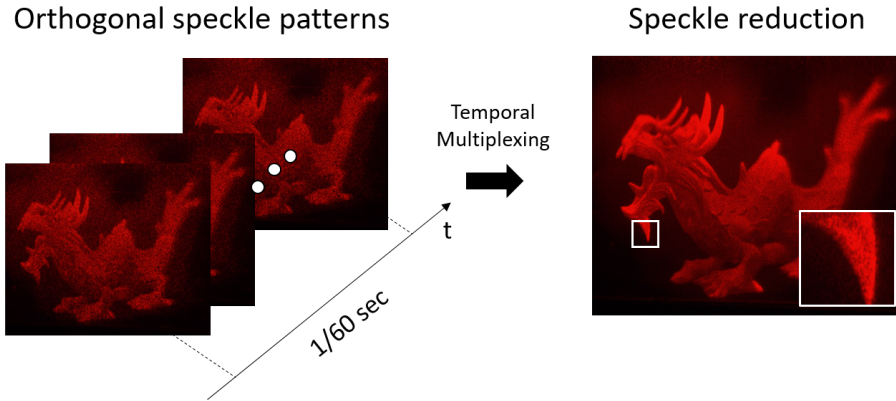


Figure 5.5 Temporal multiplexing to reduce speckle noise.

the aberrations are well corrected using the proposed global method compared with the raw hologram [Fig. 5.4(a)]. The pre-measured global correction map is used corresponding to each LD, as shown in Fig. 5.4(c). Then, the author applies temporal multiplexing to reduce speckle noise and to achieve the high-quality holographic display results as shown in Fig. 5.5. The 30 sub-frames which are generated from orthogonal random phase form one-frame within 1/60 second. A detailed explanation of speckle noise reduction is provided in Section 5.5.1.

Figure 5.6 is a set of experimentally captured images according to the viewing angle. The image sensor focuses on the head of the dragon hologram. In the sub-images, the left bottom insets mean the number of illuminations (i, j), and the right bottom insets are the observing angles corresponding to the center of each viewing zone. Considering the bezel of the used filter and efficiency of the hologram's information, the author designs each viewing angle as $\pm 3.2^\circ \times \pm 3.2^\circ$ rather than the period of the sub-viewing zone of 7.4° , where it is given by $\tan^{-1}(p/f_3)$. It has an advantage that the size of the hologram increases but brings some non-observable regions at the boundary of the sub-viewing zones. The discrete viewing angle issue would be mitigated as the filter

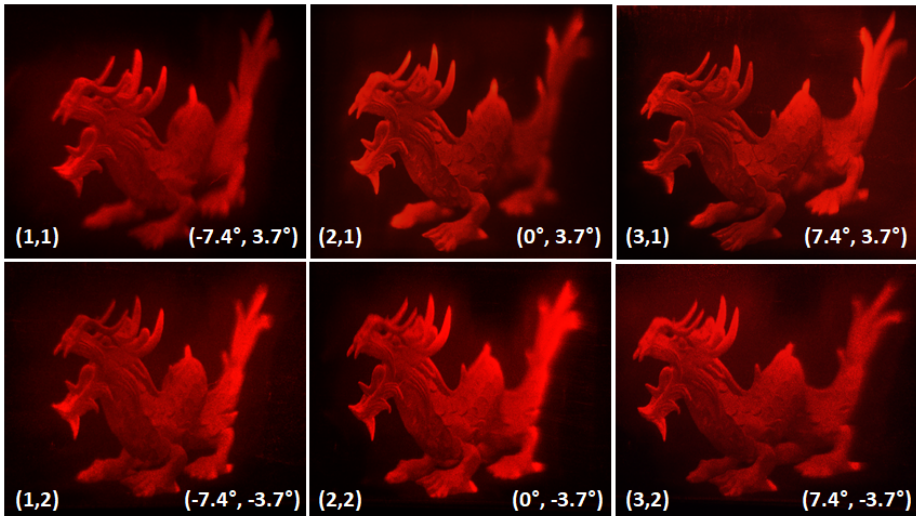


Figure 5.6 Captured results in changing the image sensor's observation angles. Each viewing zone covers $\pm 3.2^\circ \times \pm 3.2^\circ$ from the center axis, indicated by the inset in the right bottom.

array fill factor is enhanced in the future. Using the proposed TM illumination technique, the viewing zone is 2-D expanded to $\pm 9.6^\circ \times \pm 6.4^\circ$ effectively. The author carries out another experiment to show a 3-D focus cue with the high-frame rate application's feasibility using a 3-D object of the butterfly. Figure 5.7 is a captured image by shifting the focal plane of the image sensor. The 1st image is obtained when the object is rendered and displayed on the 2-D plane (1.4 cm after DMD) for comparison. The object is 3-D rendered identical conditions with the dragon object to capture the 2nd - 4th images. The focus cue is confirmed by the results of changing the focal plane. Finally, holographic videos are recorded sequentially, changing the focal planes from the front to the rear. The videos are recorded as 60 Hz using a high-frame rate of CMOS sensor (FLIR, FL3-U3-20E4C-C). Four sample frames of the video with input images are illustrated in Fig. 5.8.

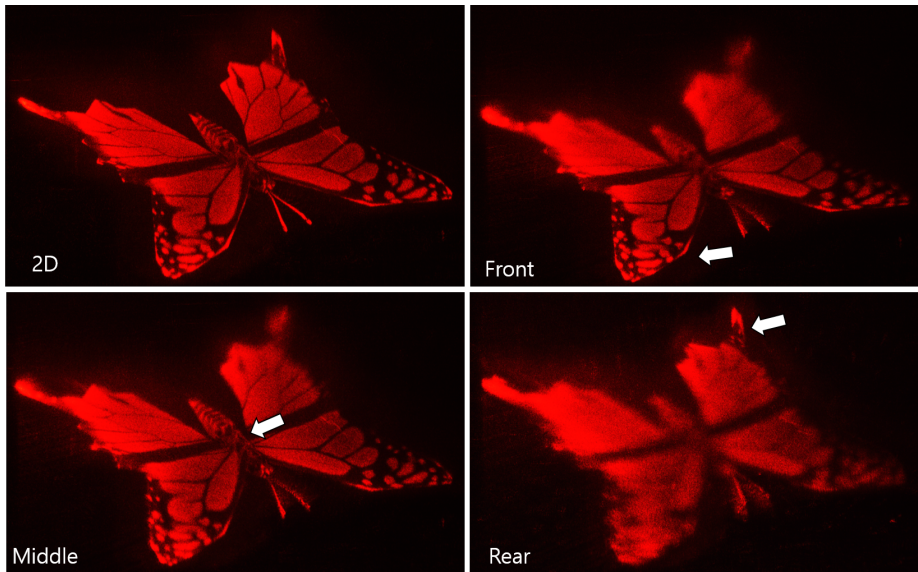


Figure 5.7 Experimental result when the 2-D (1st) and 3-D hologram (2nd - 4th) are displayed.



Figure 5.8 Four sample frames of the holographic video as focusing on the middle depth. Top columns are experimental photographs and bottoms are input images.

5.5 Discussion

5.5.1 Speckle

Another major issue of the holographic displays is the speckle noise from coherent light source [93–95]. Speckle is a random interference pattern from scattered coherent light, which severely degrades reconstructed hologram quality. Also, high-intensity from the constructive interference of the speckle can damage the human visual system. Speckle reduction methods have been proposed

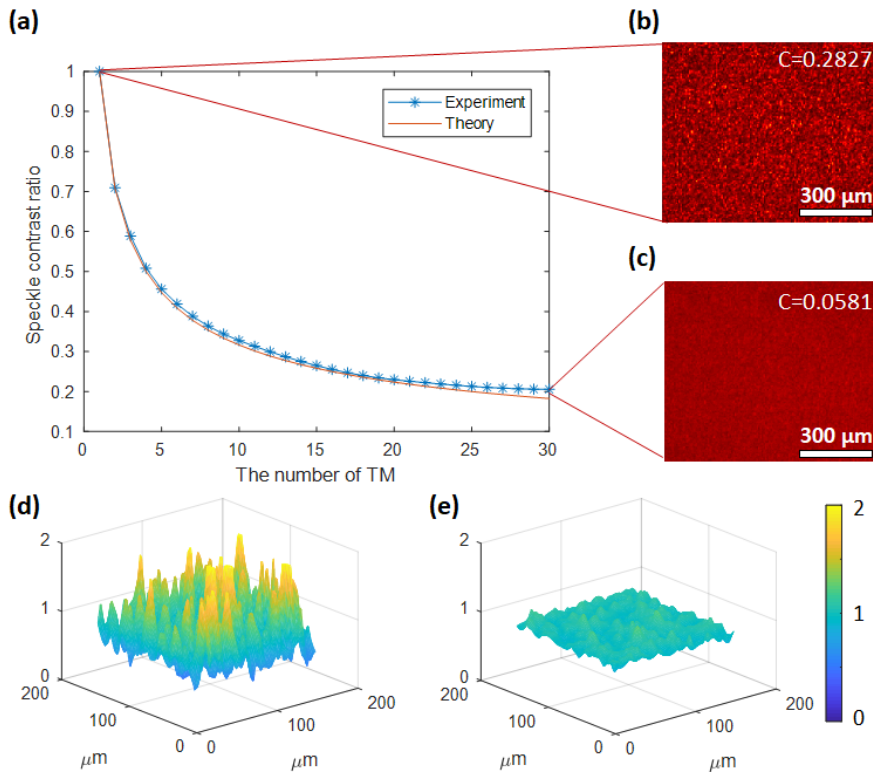


Figure 5.9 (a) The speckle contrast ratio versus the number of TM. (b),(c) Experimental results of the 2-D uniform hologram without TM and with TM of 30 frames, respectively. (d),(e) Enlarged distributions of the **b** and **c**.

via a partially coherent light source [95] and temporal superposition [96]. When the partially coherent light is used, the speckle is produced less due to the short coherence length. However, the low-coherence sacrifices spatial resolution and depth of field of the reconstructed hologram. On the other hand, the temporal superposition mitigates the speckle noise by summing multiple holograms having uncorrelated speckle patterns. It could be realized by applying the TM of holograms generated from different random phase patterns [97]. However, since the TM decreases the frame rate of the display, high-frame rate SLM is required to apply the method.

The author multiplexes 30 holograms for each frame by changing the random phase profile to reduce speckle noise. From Fig. 5.5(c), it is confirmed that the quality of the hologram is remarkably enhanced with TM. To quantitatively analyze the effect of TM for speckle reduction, a 2-D hologram of the uniform intensity image is captured. Figure 5.9(a) shows the experimentally obtained speckle contrast ratio as increasing the number of TM states. Figures 5.9(b) and 5.9(c) are the captured images when the number of TM is 1 and 30, and Figs. 5.9(d) and 5.9(e) are zoom-in intensity profiles, respectively. The speckle contrast values are calculated as 0.2827 and 0.0581. It shows that the implemented system reduces the speckle contrast as the ratio of 0.2055 when 30 frames are multiplexed. The reduction ratio is well-matched with the theoretically expected value of 0.1826, and the overall tendency is also consistent with the theory (inverse square root of the number of TM).

5.5.2 Applications for Near-eye Displays

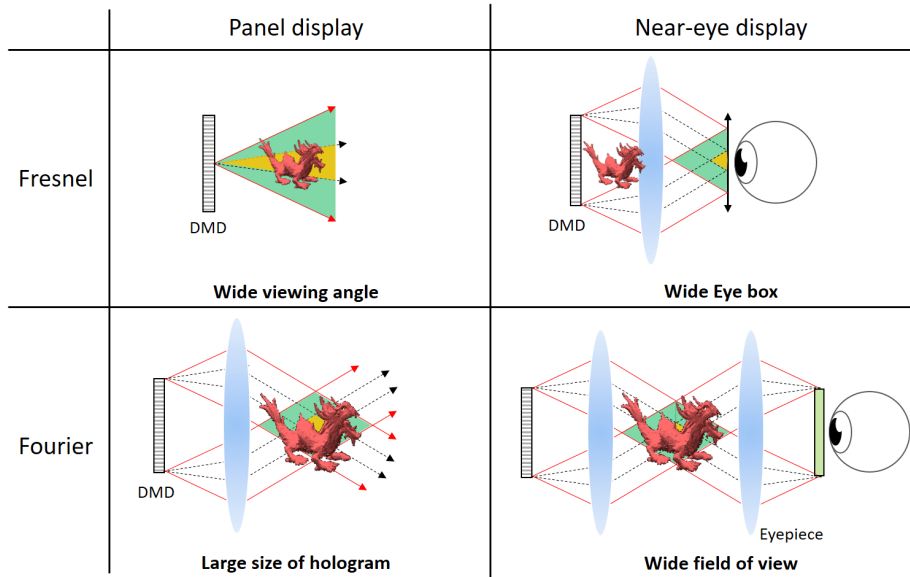


Figure 5.10 Applications of SBP expanding in four types of holographic displays.

The holographic displays can be implemented not only in the Fresnel panel-type (mainly covered in this Chapter) but also in the near-eye type. Since the SBP indicates the fundamental trade-off relationship of holographic displays, the method can also be applied to the near-eye displays.

Eye-box expansion

First, the author demonstrates the near-eye configuration with Fresnel holography. The near-eye type display is implemented by placing an eyepiece lens between the observer's eye and virtual hologram, as shown in Fig. 5.10. The eyepiece magnifies and floats the hologram when the axial distance is less than the focal length of the lens. The eye-box is determined as a two-dimensional

size at which light diffracted from one pixel of the SLM reaches the pupil plane of the user. Thus, the diffraction angle extended through the proposed method widens the eye-box.

To briefly verify the concept via experiment, the author additionally places an eyepiece lens ($f = 100mm$) at the exit pupil of the previously implemented system (Fig. 5.2). The floated hologram is also captured by a CCD camera after passing through an additional beam-splitter to observe the AR scene. Figure 5.11 is experimental results captured as moving the camera in the horizontal axis. Since the proposed system shows three times wider eye-box on the horizontal axis, it can be confirmed that the eye-box is improved in proportion to the number of lateral LD array. Note that the field of view (FOV) is about 6° , and the FOV and eye-box can be optimized by adjusting the magnification of the optical system.

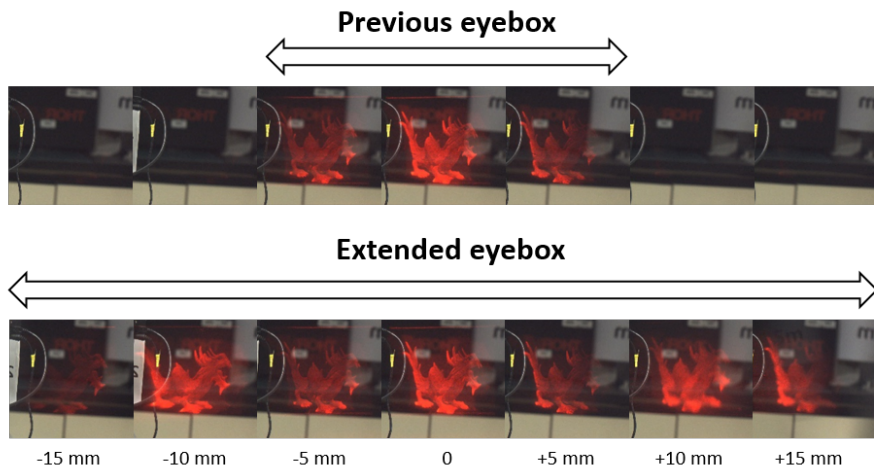


Figure 5.11 Eye-box expanded system of AR near-eye holographic display.

Full-color VR/AR displays

For display systems, full-color representation is important to provide a more immersive experience to the users. SLM used for holographic displays, neither LC nor DMD, does not have a color filter that separates RGB wavelengths. Therefore, in general, TM is adopted as synchronizing the SLM and laser for each color. It reduces the entire display's frame rate by a factor of 3. Thus, the binary SLM would be a good candidate for a full-color holographic system by taking advantage of its fast frame rate. To demonstrate the concept of full-color VR/AR holographic display, the author implements additional sets up, as shown in Fig. 5.12. Fourier holography is adopted to minimize optical set-up by removing one lens that composes the $4f$ system and to improve the quality of reconstructed hologram. Here, binary amplitude SLM is implemented by combining ferroelectric liquid crystal on silicon (FLCOS) and linear polarizer (LP). A conventional single lens is used for an eyepiece for the VR system, and an RGB multiplexed holographic optical element (HOE) lens is used for the AR system. The HOE lens is manufactured to Fourier transform off-axis (about 60°) incident light and transfer it to the user. The author divides a total of 3600 Hz of SLM into RGB implementation (3 Hz) and 24 frames for speckle reduction, so the display provides the 50 Hz full-color holographic video. FOV and eyebox for the full-color VR setup are (10.2° , 5.1°) and (4.8 mm, 3.6 mm). FOV and eyebox for the full-color AR setup are (66.3° , 16.6°) and (1.1 mm, 0.7 mm).

Figure 5.13 shows experimental results of full-color binary near-eye holographic display. The speckle reduced high-quality of holograms are reconstructed in both systems. The top column holograms are generated from a 2-D image of the berry. The results in the 2nd and 3rd rows show some frames extracted from the captured video while changing the focus in the VR result. Note that the re-

sults are extracted from a different frame of content. To obtain the AR results, the author pre-compensate RGB optical aberrations occurring in an off-axis full-color HOE. The AR results will be further improved if the color uniformity and efficiency of the full-color HOE are precisely manufactured. Although SBP expansion through SI is not applied in this system, it can be implemented by synchronizing the laser diode array and filter array for each wavelength.

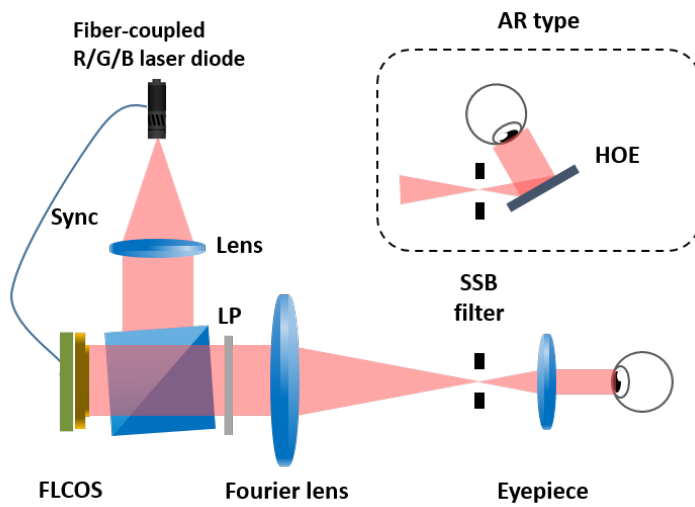


Figure 5.12 Full-color binary holographic near-eye display.

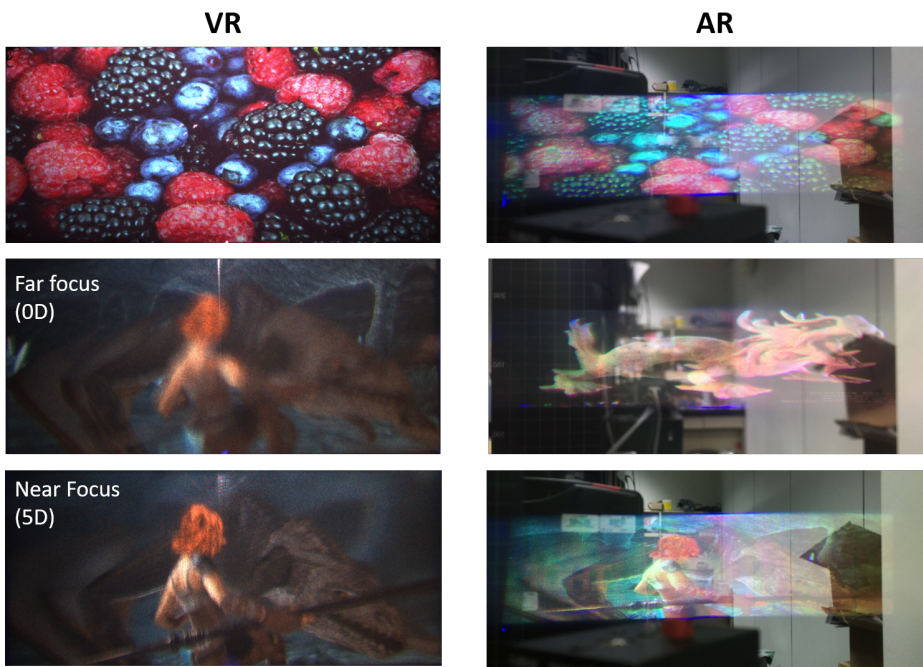


Figure 5.13 Experimental results of full-color binary near-eye holographic display.

5.6 Conclusion

In this chapter, the author proposes and experimentally demonstrate TM with directional illumination to enhance the SBP of holographic display. This technique successfully expands the viewing angle while maintaining the size of the hologram and reducing the speckle noise. Considering the high driving speed of the DMD, the author designs a high-speed holographic video display of 60 Hz with a six times wide viewing angle and 0.21 times reduced speckle noise. Furthermore, near-eye as well as panel type holographic display is introduced and verified, which provides a large eye-box due to the enhanced SBP. The possibility of a full-color structure is confirmed in both VR and AR structures through the synchronization of RGB light sources and binary SLM. Full-color SBP expanded system can be implemented by designing the filter array with RGB structured illumination considering DMD's diffraction characteristic. Since the present method enlarges SBP and reduces speckle noise, which is a fundamental limitation of the holographic display, the author expects that the proposed technique can be utilized for various applications such as table-top and near-eye holographic displays.

Chapter 6. Conclusion

This dissertation presents the studies on high SBP for complex amplitude imaging and display systems. SBP represents the amount of information and allows the complex amplitude system to follow a trade-off relationship within this indicator. To improve the SBP of the complex amplitude in a limited amount of information, various multiplexing techniques suitable for the implemented system are applied. Computational separation algorithm combined with novel optical design allows the acquired multiplexed information to be decomposed in the imaging system, leading to improve size of the image or resolution. In the display system, the author decomposes the multiplex information by combining human perceptual temporal bandwidth and spatial filtering, so extended viewing angle is achieved.

At the beginning of the dissertation, theoretical definitions of the complex amplitude and SBP are introduced to help readers understand the proposed methods that will be presented in later Chapters. These concepts are then applied to two optical engineering applications, imaging and display fields, to study their relationship in system performance with existing challenges. Since the SBP is limited to express complex values using the image sensor's pixelated structure or SLM, it hinders various realization for the complex amplitude controlling system. Thus, followed Chapters tries to minimize the limitation and obtain a large SBP complex field by devising novel multiplexed encoding techniques with decomposition methods.

First, DH with off-axis configuration as a tool of complex amplitude imaging system is studied. Here, frequency multiplexing is adopted to use the remained bandwidth of the captured hologram efficiently. Two different wave-

lengths of laser diodes are used to avoid mutual interference noise. The author implemented the dual-wavelength DH system using a single diffraction grating, termed SGD. Considering the multi-functional application of the grating, such as diffraction, reflection, wavelength, and polarization dependency, lots of optical elements for conventional dual-wavelength DH interferometer are replaced by only a diffraction grating. The prototype showed a compact design and provided a hologram of the diffraction-limited resolution with the double size of the image. Also, the proposed 2-times expanded SBP system supported by 3-D imaging, whose quantitative depth resolution is under the sub-wavelength. The author believes the proposed SGD has potential in various practical use, including inspection, identification, cell imaging, and where the compact holographic sensing system with wide size of the image is required.

Although SGD showed double expanded SBP, the off-axis DH couldn't reach SBP of the image sensor to avoid aliasing with interference noise terms. In Chapter 4, the SBP more expanded imaging system is proposed using computational imaging. The proposed method (SSFPM) is devised by combining FPM, lens array imaging, and multiplexed illumination. To ensure that a single shot had multiplexed information, the specimen is simultaneously illuminated with 3×3 LEDs. A computational algorithm is developed to decompose the multiplexed information and obtain a high-resolution complex amplitude. At the same time, an optical system, including a lens array is designed and implemented for this algorithm to converge. The authors experimentally showed that the SBP of SSFPM could reach the level of the imaging sensor and is comparable to other conventional multi-shot complex amplitude imaging technologies that require 3 to 4 images. The author believes SSFPM can provide new possibilities in phase retrieval microscopy in that high resolution of quantitative phase imaging is acquired with a single measurement.

Finally, the author extended the aim of this dissertation to the display area by adopting the previous multiplexing methods. Using an LD array, SI of directional plane-wave illuminations is implemented to expand the viewing angle of the holographic displays. In addition, the filter array was placed in the Fourier plane in synchronization with the LD array and the DMD to effectively remove high-order noise. Considering the DMD's high driving speed, the author designs a high-speed holographic video display of 60 Hz with a six times wide viewing angle and 0.21 times reduced speckle noise. Also, near-eye displays that provide expanded eye-box or full-color hologram are introduced and verified.

For the future work, the author suggests several topics for further improvement of proposed systems. First, in the SGDH of Chapter 3, frequency multiplexing can be performed more than the currently implemented double by implementing the optimized system design between the diffraction angles and the period of the diffraction grating. Second, in the SSFPM of Chapter 4, research to boost complex amplitude reconstruction time through optimization of algorithm with parallel computing can be studied. From the work, it is expected that the commercialization of a 3-D microscope beyond the existing 2-D microscopes can be achieved. Third, in Chapter 5, holographic displays with improved performance according to the user's taste can be studied through time domain engineering. Also, the full-color systems and near-eye displays can be studied.

The author hopes that this thesis will contribute to developing the imaging and display fields, which share a common problem of small SBP. The author hopes that the proposed methods will inspire various researchers to approach the implementation of complex amplitude systems, and various future industries, including 3-D inspection, holography, VR, and AR, will be realized with high-performance.

Bibliography

- [1] O. Bryngdahl and A. Lohmann, “Single-sideband holography,” *JOSA*, vol. 58, no. 5, pp. 620–624, 1968.
- [2] C. Hsueh and A. Sawchuk, “Computer-generated double-phase holograms,” *Applied optics*, vol. 17, no. 24, pp. 3874–3883, 1978.
- [3] E. Cuche, P. Marquet, and C. Depeursinge, “Simultaneous amplitude-contrast and quantitative phase-contrast microscopy by numerical reconstruction of fresnel off-axis holograms,” *Applied optics*, vol. 38, no. 34, pp. 6994–7001, 1999.
- [4] E. Cuche, P. Marquet, and C. Depeursinge, “Spatial filtering for zero-order and twin-image elimination in digital off-axis holography,” *Applied optics*, vol. 39, no. 23, pp. 4070–4075, 2000.
- [5] E. N. Leith and J. Upatnieks, “Reconstructed wavefronts and communication theory,” *JOSA*, vol. 52, no. 10, pp. 1123–1130, 1962.
- [6] L. Waller, Y. Luo, S. Y. Yang, and G. Barbastathis, “Transport of intensity phase imaging in a volume holographic microscope,” *Optics letters*, vol. 35, no. 17, pp. 2961–2963, 2010.
- [7] Z. Yang and Q. Zhan, “Single-shot smartphone-based quantitative phase imaging using a distorted grating,” *Plos one*, vol. 11, no. 7, p. e0159596, 2016.
- [8] P. Sidorenko and O. Cohen, “Single-shot ptychography,” *Optica*, vol. 3, no. 1, pp. 9–14, 2016.

- [9] P. Sidorenko, O. Lahav, and O. Cohen, “Ptychographic ultrahigh-speed imaging,” *Optics express*, vol. 25, no. 10, pp. 10997–11008, 2017.
- [10] M. R. Teague, “Deterministic phase retrieval: a green’s function solution,” *JOSA*, vol. 73, no. 11, pp. 1434–1441, 1983.
- [11] C. Zuo, Q. Chen, W. Qu, and A. Asundi, “High-speed transport-of-intensity phase microscopy with an electrically tunable lens,” *Optics express*, vol. 21, no. 20, pp. 24060–24075, 2013.
- [12] J. C. Petrucci, L. Tian, and G. Barbastathis, “The transport of intensity equation for optical path length recovery using partially coherent illumination,” *Optics express*, vol. 21, no. 12, pp. 14430–14441, 2013.
- [13] P. Marquet, B. Rappaz, P. J. Magistretti, E. Cuche, Y. Emery, T. Colomb, and C. Depeursinge, “Digital holographic microscopy: a noninvasive contrast imaging technique allowing quantitative visualization of living cells with subwavelength axial accuracy,” *Optics letters*, vol. 30, no. 5, pp. 468–470, 2005.
- [14] Gabor, “A new microscopic principle,” *Nature*, vol. 161, no. 4098, pp. 777–778, 1948.
- [15] M. K. Kim, “Principles and techniques of digital holographic microscopy,” *Journal of photonics for energy*, pp. 018005–018005, 2010.
- [16] T.-C. Poon, *Digital holography and three-dimensional display: Principles and Applications*. Springer Science & Business Media, 2006.
- [17] P. W.-M. Tsang and T.-C. Poon, “Review on the state-of-the-art technologies for acquisition and display of digital holograms,” *IEEE transactions on industrial informatics*, vol. 12, no. 3, pp. 886–901, 2016.

- [18] J. Min, B. Yao, P. Gao, R. Guo, B. Ma, J. Zheng, M. Lei, S. Yan, D. Dan, T. Duan, Y. Yang, and T. Ye, “Dual-wavelength slightly off-axis digital holographic microscopy,” *Applied optics*, vol. 51, no. 2, pp. 191–196, 2012.
- [19] C. Jang, J. Kim, D. C. Clark, S. Lee, B. Lee, and M. K. Kim, “Holographic fluorescence microscopy with incoherent digital holographic adaptive optics,” *Journal of biomedical optics*, vol. 20, no. 11, p. 111204, 2015.
- [20] J. Hong and M. K. Kim, “Single-shot self-interference incoherent digital holography using off-axis configuration,” *Optics letters*, vol. 38, no. 23, pp. 5196–5199, 2013.
- [21] B. Lee, J.-Y. Hong, D. Yoo, J. Cho, Y. Jeong, S. Moon, and B. Lee, “Single-shot phase retrieval via fourier ptychographic microscopy,” *Optica*, vol. 5, no. 8, pp. 976–983, 2018.
- [22] A. Barty, S. Boutet, M. J. Bogan, S. Hau-Riege, S. Marchesini, K. Sokolowski-Tinten, N. Stojanovic, H. Ehrke, A. Cavalleri, S. Düsterer, M. Frank, S. Bajt, B. W. Woods, M. M. Seibert, J. Hajdu, R. Treusch, and H. N. Chapman, “Ultrafast single-shot diffraction imaging of nanoscale dynamics,” *Nature photonics*, vol. 2, no. 7, p. 415, 2008.
- [23] D. Abdelsalam, R. Magnusson, and D. Kim, “Single-shot, dual-wavelength digital holography based on polarizing separation,” *Applied optics*, vol. 50, no. 19, pp. 3360–3368, 2011.
- [24] J. Kühn, T. Colomb, F. Montfort, F. Charrière, Y. Emery, E. Cuche, P. Marquet, and C. Depeursinge, “Real-time dual-wavelength digital holographic microscopy with a single hologram acquisition,” *Optics express*, vol. 15, no. 12, pp. 7231–7242, 2007.

- [25] A. Khmaladze, M. Kim, and C.-M. Lo, “Phase imaging of cells by simultaneous dual-wavelength reflection digital holography,” *Optics express*, vol. 16, no. 15, pp. 10900–10911, 2008.
- [26] M. Shan, L. Liu, Z. Zhong, B. Liu, G. Luan, and Y. Zhang, “Single-shot dual-wavelength off-axis quasi-common-path digital holography using polarization-multiplexing,” *Optics express*, vol. 25, no. 21, pp. 26253–26261, 2017.
- [27] M. Paturzo, F. Merola, S. Grilli, S. De Nicola, A. Finizio, and P. Ferraro, “Super-resolution in digital holography by a two-dimensional dynamic phase grating,” *Optics express*, vol. 16, no. 21, pp. 17107–17118, 2008.
- [28] C. Yuan, H. Zhai, and H. Liu, “Angular multiplexing in pulsed digital holography for aperture synthesis,” *Optics letters*, vol. 33, no. 20, pp. 2356–2358, 2008.
- [29] P. Girshovitz and N. T. Shaked, “Doubling the field of view in off-axis low-coherence interferometric imaging,” *Light: science applications*, vol. 3, no. 3, p. e151, 2014.
- [30] B. Tayebi, F. Sharif, M. R. Jafarfard, and D. Y. Kim, “Double-field-of-view, quasi-common-path interferometer using fourier domain multiplexing,” *Optics express*, vol. 23, no. 20, pp. 26825–26833, 2015.
- [31] I. Frenklach, P. Girshovitz, and N. T. Shaked, “Off-axis interferometric phase microscopy with tripled imaging area,” *Optics letters*, vol. 39, no. 6, pp. 1525–1528, 2014.

- [32] M. Lee, O. Yaglidere, and A. Ozcan, “Field-portable reflection and transmission microscopy based on lensless holography,” *Biomedical Optics express*, vol. 2, no. 9, pp. 2721–2730, 2011.
- [33] Y. Hu, C. Zuo, J. Sun, Q. Chen, and Y. Zhang, “A compact and lensless digital holographic microscope setup,” in *International Conference on Optical and Photonic Engineering (icOPEN 2015)*, vol. 9524, p. 952426, International Society for Optics and Photonics, 2015.
- [34] A. Adinda-Ougba, B. Kabir, N. Koukourakis, F. Mitschker, N. Gerhardt, and M. Hofmann, “Compact low-cost lensless digital holographic microscope for topographic measurements of microstructures in reflection geometry,” in *Optical Systems Design 2015: Optical Fabrication, Testing, and Metrology V*, vol. 9628, p. 962818, International Society for Optics and Photonics, 2015.
- [35] M. Rubin, G. Dardikman, S. K. Mirsky, N. A. Turko, and N. T. Shaked, “Six-pack off-axis holography,” *Optics letters*, vol. 42, no. 22, pp. 4611–4614, 2017.
- [36] Y. Lu, Y. Liu, P. Li, Y. Fu, and J. Zhao, “Multiplexed off-axis holography using a transmission diffraction grating,” *Optics letters*, vol. 41, no. 3, pp. 512–515, 2016.
- [37] W. Zhang, L. Cao, G. Jin, and D. Brady, “Full field-of-view digital lens-free holography for weak-scattering objects based on grating modulation,” *Applied optics*, vol. 57, no. 1, pp. A164–A171, 2018.
- [38] W.-C. Hsu, J.-W. Su, T.-Y. Tseng, and K.-B. Sung, “Tomographic diffractive microscopy of living cells based on a common-path configuration,” *Optics letters*, vol. 39, no. 7, pp. 2210–2213, 2014.

- [39] V. Mico, C. Ferreira, Z. Zalevsky, and J. García, “Spatially-multiplexed interferometric microscopy (smim): converting a standard microscope into a holographic one,” *Optics express*, vol. 22, no. 12, pp. 14929–14943, 2014.
- [40] G. Popescu, T. Ikeda, R. R. Dasari, and M. S. Feld, “Diffraction phase microscopy for quantifying cell structure and dynamics,” *Optics letters*, vol. 31, no. 6, pp. 775–777, 2006.
- [41] B. Bhaduri, C. Edwards, H. Pham, R. Zhou, T. H. Nguyen, L. L. Goddard, and G. Popescu, “Diffraction phase microscopy: principles and applications in materials and life sciences,” *Advances in optics and photonics*, vol. 6, no. 1, pp. 57–119, 2014.
- [42] V. Bianco, B. Mandracchia, V. Marchesano, V. Pagliarulo, F. Olivieri, S. Coppola, M. Paturzo, and P. Ferraro, “Endowing a plain fluidic chip with micro-optics: a holographic microscope slide,” *Light: science applications*, vol. 6, no. 9, p. e17055, 2017.
- [43] R. M. Goldstein, H. A. Zebker, and C. L. Werner, “Satellite radar interferometry: Two-dimensional phase unwrapping,” *Radio science*, vol. 23, no. 4, pp. 713–720, 1988.
- [44] Z. von F, “Beugungstheorie des schneidenverfahrens und seiner verbesserten form, der phasenkontrastmethode,” *Physica*, vol. 1, no. 7-12, pp. 689–704, 1934.
- [45] V. L. Genberg, G. J. Michels, and K. B. Doyle, “Orthogonality of zernike polynomials,” in *Optomechanical Design and Engineering 2002*, vol. 4771, pp. 276–287, International Society for Optics and Photonics, 2002.

- [46] G. Zheng, R. Horstmeyer, and C. Yang, “Wide-field, high-resolution fourier ptychographic microscopy,” *Nature photonics*, vol. 7, no. 9, p. 739, 2013.
- [47] X. Ou, R. Horstmeyer, C. Yang, and G. Zheng, “Quantitative phase imaging via fourier ptychographic microscopy,” *Optics letters*, vol. 38, no. 22, pp. 4845–4848, 2013.
- [48] S. Dong, Z. Bian, R. Shiradkar, and G. Zheng, “Sparsely sampled fourier ptychography,” *Optics express*, vol. 22, no. 5, pp. 5455–5464, 2014.
- [49] S. Dong, R. Shiradkar, P. Nanda, and G. Zheng, “Spectral multiplexing and coherent-state decomposition in fourier ptychographic imaging,” *Biomedical Optics express*, vol. 5, no. 6, pp. 1757–1767, 2014.
- [50] L. Tian, X. Li, K. Ramchandran, and L. Waller, “Multiplexed coded illumination for fourier ptychography with an led array microscope,” *Biomedical Optics express*, vol. 5, no. 7, pp. 2376–2389, 2014.
- [51] L. Tian, Z. Liu, L.-H. Yeh, M. Chen, J. Zhong, and L. Waller, “Computational illumination for high-speed in vitro fourier ptychographic microscopy,” *Optica*, vol. 2, no. 10, pp. 904–911, 2015.
- [52] J. Sun, Q. Chen, Y. Zhang, and C. Zuo, “Sampling criteria for fourier ptychographic microscopy in object space and frequency space,” *Optics express*, vol. 24, no. 14, pp. 15765–15781, 2016.
- [53] R. Horstmeyer, J. Chung, X. Ou, G. Zheng, and C. Yang, “Diffraction tomography with fourier ptychography,” *Optica*, vol. 3, no. 8, pp. 827–835, 2016.

- [54] S. Pacheco, G. Zheng, and R. Liang, “Reflective fourier ptychography,” *Journal of biomedical optics*, vol. 21, no. 2, pp. 026010–026010, 2016.
- [55] S. Dong, P. Nanda, R. Shiradkar, K. Guo, and G. Zheng, “High-resolution fluorescence imaging via pattern-illuminated fourier ptychography,” *Optics express*, vol. 22, no. 17, pp. 20856–20870, 2014.
- [56] M. Levoy, R. Ng, A. Adams, M. Footer, and M. Horowitz, “Light field microscopy,” *ACM transactions on graphics (TOG)*, vol. 25, no. 3, pp. 924–934, 2006.
- [57] J. Kim, J.-H. Jung, Y. Jeong, K. Hong, and B. Lee, “Real-time integral imaging system for light field microscopy,” *Optics express*, vol. 22, no. 9, pp. 10210–10220, 2014.
- [58] A. Llavador, J. Sola-Pikabea, G. Saavedra, B. Javidi, and M. Martínez-Corral, “Resolution improvements in integral microscopy with fourier plane recording,” *Optics express*, vol. 24, no. 18, pp. 20792–20798, 2016.
- [59] M. Broxton, L. Grosenick, S. Yang, N. Cohen, A. Andalman, K. Deisseroth, and M. Levoy, “Wave optics theory and 3-d deconvolution for the light field microscope,” *Optics express*, vol. 21, no. 21, pp. 25418–25439, 2013.
- [60] J.-Y. Hong, J. Yeom, J. Kim, S.-g. Park, Y. Jeong, and B. Lee, “Analysis of the pickup and display property of integral floating microscopy,” *Journal of information display*, vol. 16, no. 3, pp. 143–153, 2015.
- [61] J. R. Fienup, “Reconstruction of a complex-valued object from the modulus of its fourier transform using a support constraint,” *JOSA A*, vol. 4, no. 1, pp. 118–123, 1987.

- [62] J. R. Fienup, "Lensless coherent imaging by phase retrieval with an illumination pattern constraint," *Optics express*, vol. 14, no. 2, pp. 498–508, 2006.
- [63] I. Yamaguchi and T. Zhang, "Phase-shifting digital holography," *Optics letters*, vol. 22, pp. 1268–1270, Aug 1997.
- [64] W. Bishara, T.-W. Su, A. F. Coskun, and A. Ozcan, "Lensfree on-chip microscopy over a wide field-of-view using pixel super-resolution," *Optics express*, vol. 18, no. 11, pp. 11181–11191, 2010.
- [65] T. J. Fuchs and J. M. Buhmann, "Computational pathology: Challenges and promises for tissue analysis," *Computerized Medical Imaging and Graphics*, vol. 35, no. 7, pp. 515–530, 2011.
- [66] J. Miao, T. Ishikawa, I. K. Robinson, and M. M. Murnane, "Beyond crystallography: Diffractive imaging using coherent x-ray light sources," *Science*, vol. 348, no. 6234, pp. 530–535, 2015.
- [67] M. A. Pfeifer, G. J. Williams, I. A. Vartanyants, R. Harder, and I. K. Robinson, "Three-dimensional mapping of a deformation field inside a nanocrystal," *Nature*, vol. 442, no. 7098, pp. 63–66, 2006.
- [68] A. M. Maiden, J. M. Rodenburg, and M. J. Humphry, "Optical ptychography: a practical implementation with useful resolution," *Optics letters*, vol. 35, no. 15, pp. 2585–2587, 2010.
- [69] H. Faulkner and J. Rodenburg, "Movable aperture lensless transmission microscopy: a novel phase retrieval algorithm," *Physical review letters*, vol. 93, no. 2, p. 023903, 2004.

- [70] R. Horisaki, Y. Ogura, M. Aino, and J. Tanida, "Single-shot phase imaging with a coded aperture," *Optics letters*, vol. 39, no. 22, pp. 6466–6469, 2014.
- [71] L. Denis, D. Lorenz, E. Thiébaud, C. Fournier, and D. Trede, "Inline hologram reconstruction with sparsity constraints," *Optics letters*, vol. 34, no. 22, pp. 3475–3477, 2009.
- [72] J. Song, C. L. Swisher, H. Im, S. Jeong, D. Pathania, Y. Iwamoto, M. Pivovarov, R. Weissleder, and H. Lee, "Sparsity-based pixel super resolution for lens-free digital in-line holography," *Scientific reports*, vol. 6, 2016.
- [73] F. Zhang, B. Chen, G. R. Morrison, J. Vila-Comamala, M. Guizar-Sicairos, and I. K. Robinson, "Phase retrieval by coherent modulation imaging," *Nature communications*, vol. 7, 2016.
- [74] Y. Rivenson, Z. Göröcs, H. Günaydin, Y. Zhang, H. Wang, and A. Ozcan, "Deep learning microscopy," *Optica*, vol. 4, pp. 1437–1443, Nov 2017.
- [75] R. W. Gerchberg, "A practical algorithm for the determination of the phase from image and diffraction plane pictures," *Optik*, vol. 35, pp. 237–246, 1972.
- [76] J. R. Fienup, "Phase retrieval algorithms: a comparison," *Applied optics*, vol. 21, no. 15, pp. 2758–2769, 1982.
- [77] J. Kim, Y. Jeong, H. Kim, C.-K. Lee, B. Lee, J. Hong, Y. Kim, Y. Hong, S.-D. Lee, and B. Lee, "F-number matching method in light field microscopy using an elastic micro lens array," *Optics letters*, vol. 41, no. 12, pp. 2751–2754, 2016.

- [78] A. Maimone, A. Georgiou, and J. S. Kollin, “Holographic near-eye displays for virtual and augmented reality,” *ACM transactions on graphics (TOG)*, vol. 36, no. 4, p. 85, 2017.
- [79] G. Li, D. Lee, Y. Jeong, J. Cho, and B. Lee, “Holographic display for see-through augmented reality using mirror-lens holographic optical element,” *Optics letters*, vol. 41, no. 11, pp. 2486–2489, 2016.
- [80] H. Yu, K. Lee, J. Park, and Y. Park, “Ultrahigh-definition dynamic 3d holographic display by active control of volume speckle fields,” *Nature photonics*, vol. 11, no. 3, p. 186, 2017.
- [81] C. Jang, K. Bang, G. Li, and B. Lee, “Holographic near-eye display with expanded eye-box,” *ACM transactions on graphics (TOG)*, vol. 37, no. 6, pp. 1–14, 2018.
- [82] J. Hahn, H. Kim, Y. Lim, G. Park, and B. Lee, “Wide viewing angle dynamic holographic stereogram with a curved array of spatial light modulators,” *Optics express*, vol. 16, no. 16, pp. 12372–12386, 2008.
- [83] G. Li, J. Jeong, D. Lee, J. Yeom, C. Jang, S. Lee, and B. Lee, “Space bandwidth product enhancement of holographic display using high-order diffraction guided by holographic optical element,” *Optics express*, vol. 23, no. 26, pp. 33170–33183, 2015.
- [84] Y. Takaki and K. Fujii, “Viewing-zone scanning holographic display using a mems spatial light modulator,” *Optics express*, vol. 22, no. 20, pp. 24713–24721, 2014.

- [85] Y. Takaki, Y. Matsumoto, and T. Nakajima, "Color image generation for screen-scanning holographic display," *Optics express*, vol. 23, no. 21, pp. 26986–26998, 2015.
- [86] M. Chlipala and T. Kozacki, "Color led dmd holographic display with high resolution across large depth," *Optics letters*, vol. 44, no. 17, pp. 4255–4258, 2019.
- [87] J.-Y. Son, B.-R. Lee, O. O. Chernyshov, K.-A. Moon, and H. Lee, "Holographic display based on a spatial dmd array," *Optics letters*, vol. 38, no. 16, pp. 3173–3176, 2013.
- [88] S. Lee, Y. Jo, D. Yoo, J. Cho, D. Lee, and B. Lee, "Tomographic near-eye displays," *Nature communications*, vol. 10, no. 1, pp. 1–10, 2019.
- [89] M. G. Gustafsson, "Surpassing the lateral resolution limit by a factor of two using structured illumination microscopy," *Journal of microscopy*, vol. 198, no. 2, pp. 82–87, 2000.
- [90] B. Lee, C. Jang, D. Kim, and B. Lee, "Single grating reflective digital holography with double field of view," *IEEE transactions on industrial informatics*, vol. 15, no. 11, pp. 6155–6161, 2019.
- [91] H. Kim, C.-Y. Hwang, K.-S. Kim, J. Roh, W. Moon, S. Kim, B.-R. Lee, S. Oh, and J. Hahn, "Anamorphic optical transformation of an amplitude spatial light modulator to a complex spatial light modulator with square pixels," *Applied optics*, vol. 53, no. 27, pp. G139–G146, 2014.
- [92] H. Zhang, L. Cao, and G. Jin, "Computer-generated hologram with occlusion effect using layer-based processing," *Applied optics*, vol. 56, no. 13, pp. F138–F143, 2017.

- [93] Y. Deng and D. Chu, “Coherence properties of different light sources and their effect on the image sharpness and speckle of holographic displays,” *Scientific reports*, vol. 7, no. 1, p. 5893, 2017.
- [94] Z. Cui, A.-t. Wang, Z. Wang, S.-l. Wang, C. Gu, H. Ming, and C.-q. Xu, “Speckle suppression by controlling the coherence in laser based projection systems,” *Journal of display technology*, vol. 11, no. 4, pp. 330–335, 2015.
- [95] D. Lee, C. Jang, K. Bang, S. Moon, G. Li, and B. Lee, “Speckle reduction for holographic display using optical path difference and random phase generator,” *IEEE transactions on industrial informatics*, vol. 15, no. 11, pp. 6170–6178, 2019.
- [96] Y. Mori, T. Fukuoka, and T. Nomura, “Speckle reduction in holographic projection by random pixel separation with time multiplexing,” *Applied optics*, vol. 53, no. 35, pp. 8182–8188, 2014.
- [97] J. W. Goodman, *Speckle Phenomena in Optics: Theory and Applications*. Roberts and Company Publishers, 2007.

Appendix

Portions of the work discussed in this dissertation were also presented in the following publications:

[Chapter 3] B. Lee, C. Jang, D. Kim, and B. Lee, "Single grating reflective digital holography with double field of view," *IEEE transactions on industrial informatics*, vol. 15, no. 11, pp. 6155-6161, 2019.

[Chapter 4] B. Lee, J.-Y. Hong, D. Yoo, J. Cho, Y. Jeong, S. Moon, and B. Lee, "Single-shot phase retrieval via Fourier ptychographic microscopy," *Optica*, vol. 5, no. 8, pp. 976-982, 2018.

[Chapter 5] B. Lee, D. Yoo, J. Jeong, S. Lee, D. Lee, B. Lee, "Wide-angle speckleless DMD holographic display using structured illumination with temporal multiplexing," *Optics letters*, vol. 45, no. 8, pp. 2148-2151, 2020.

초 록

빛을 파동으로 이해하면 간섭과 회절을 포함한 다양한 광학 현상을 해석할 수 있다. 미래 기술이라 불리는 홀로그래프, 3차원 이미징 및 3차원 디스플레이 시스템들은 파동의 복소진폭을 이해하고 변조함으로써 구현될 수 있다. 현존하는 광공학 장치를 넘어서는 파동 광학에 기반한 광공학 장치들을 상용화 및 발전시키기 위해 많은 연구가 진행되어왔지만, 지금까지 구현된 장치들은 공간 대역폭 (space-bandwidth product)의 제한으로 인해 그 성능이 대중의 기대에 부합하기 어려움을 겪고있다.

본 논문은 복소 진폭 이미징 및 디스플레이 시스템에서 공간 대역폭을 향상시키는 방법을 제안한다. 복소 진폭 변조 시스템의 성능은 광학 시스템의 정보량을 나타내는 공간 대역폭에 의해 제한된다. 이 공간 대역폭을 향상시키기 위하여 저자는 다양한 다중화 기술을 적용하며, 동시에 다중화된 정보를 분리하는 알고리즘과 장치를 고안한다. 첫번째로 디지털 홀로그래피 기술에 공간 주파수를 다중화해 대역폭을 효율적으로 활용하는 방법을 고안하여 획득된 홀로그래프의 촬영 영역을 증가시킨다. 두번째로, 단일 촬영 푸리에 타이코그래피 (single-shot Fourier ptychography) 기술에서는 광 조사 다중화를 사용하여 이미지 센서에 기록되는 정보의 양을 확장시킨다. 다중화 된 정보를 분해하고 복소 진폭을 획득하기 위하여 새로운 광학 시스템과 전산 알고리즘을 고안하여 해상도가 향상된 복소 진폭을 획득한다. 세번째로, 저자는 홀로그래프 디스플레이에 조명 다중화 및 시분할 기술을 적용한다. 다중화 된 정보는 인간의 인지적 시간 대역폭과 제안된 시스템의 공간 필터링의 결합으로 분해된다. 구현된 홀로그래픽 디스플레이는 공간 대역폭이 확장되어 더 넓은 시야각에 삼차원 홀로그래프를 제공한다.

본 논문은 작은 공간대역폭이라는 공통된 문제를 공유하는 이미징 및 디

스플레이 분야의 발전에 기여할 것으로 기대된다. 저자는 본 연구에서 제안된 방법이 다양한 복소 진폭 변조 시스템의 성능 향상에 영감을 주며, 나아가 삼차원 계측, 홀로그래피, 가상 및 증강현실을 포함한 다양한 미래 산업에 발전에 기여할 수 있기를 기대한다.

주요어: 공간 대역폭, 복소 진폭, 디지털 홀로그래피, 푸리에 타이코그래피, 홀로그래픽 디스플레이

학번: 2015-22798